DEPARTMENT OF PHYSICS, UNIVERSITY OF JYVÄSKYLÄ
RESEARCH REPORT No. 8/2000

# NANOFABRICATION BY ATOMIC FORCE MICROSCOPY, ELECTRON BEAM LITHOGRAPHY AND REACTIVE ION ETCHING

BY
ANSSI LINDELL

Academic Dissertation
for the Degree of
Doctor of Philosophy

Jyväskylä, Finland
August 2000

URN:ISBN:978-951-39-9461-7
ISBN 978-951-39-9461-7 (PDF)
ISSN 0075-465X

Jyväskylän yliopisto, 2022

ISBN 951-39-0770-8
ISSN 0075-465X

DEPARTMENT OF PHYSICS, UNIVERSITY OF JYVÄSKYLÄ
RESEARCH REPORT No. 8/2000

# NANOFABRICATION BY ATOMIC FORCE MICROSCOPY, ELECTRON BEAM LITHOGRAPHY AND REACTIVE ION ETCHING

BY
ANSSI LINDELL

Academic Dissertation
for the Degree of
Doctor of Philosophy

To be presented, by permission of the
Faculty of Mathematics and Science
of the University of Jyväskylä,
for public Examination in Auditorium FYS 1 of the
University of Jyväskylä on October 13, 2000,
at 12 o'clock noon

Jyväskylä, Finland
August 2000

# Preface

I wish to thank my supervisor, Prof. Jukka Pekola for his guidance during this work. I have learned a huge amount from him about physics, experimental techniques and scientific outlook. I also want to thank my earlier supervisor Prof. Mikko Paalanen for his bright and inspiring attitude.

Prof. Kalevi Valli also deserves special thanks for his introduction during my odyssey in nuclear physics. The skills he taught me in vacuum technology have been a tremendous help in instrumentations made in this work.

Dr. Per Davidsson and Dr. Abdel Aassime were excellent collaborators for parts of this work. Per initiated our AFM based reseach and Abdel developed vertical junction fabrication technique during their periods in Jyväskylä. They both are warmly acknowledged for pleasant and instructive collaboration. Further, I want to thank Mr. Jukka Mattila for fabrication of microcalorimeters, Dr. Prosenjit Singha Deo for theoretical calculations and Mr. Ari Jäsberg for the simulations. I am also grateful for discussions that we had by email with Dr. Joe Nabity about electron beam lithography.

The Technology Development Center, Department of Physics and Jyväskylä Science Park are gratefully acknowledged for the financial support and investments in facilities used in this work.

Finally, I wish to extend my gratitude to my fellow students, to my friends and to Anja for everything.

Jyväskylä, August 2000
Anssi Lindell

# Abstract

This thesis describes a selection of methods tested and developed for fabrication of nanodevices in the Department of Physics at the University of Jyväskylä during the period 1996-1999. Atomic force microscopy, electron beam lithography and reactive ion etching were the primary methods under investigation, but also bulk micro machined silicon nitride membranes were used as substrates for vertical tunnel junctions and as a basis of a micro calorimeter for investigating thin superconducting disks. These are the main devices fabricated, but the work has also included some aspects of nanofabrication using an atomic force microscope. Suppressing conductance of a thin metallic wire by anodic oxidation and efforts to fabricate planar tunnel junctions by atomic force microscopy will be described.

# Author's contribution

This thesis is partly based on the published papers [75, 122, 140, 125, 8] and [60]. The author of this thesis has written papers [8, 75] and [140] and participated in the writing of the papers [60] and [122]. The development and testing of a pattern generator for an atomic force microscope described in section 4.3.5 has been performed by the author. The author has taken active part in designing the micro-calorimeters and he has been responsible for the experimental work on them as described in Section 8. He has also developed the sample fabrication techniques using an atomic force microscope reported in this thesis.

The sample fabrication technique through a thin silicon nitride membrane [125], originally designed in our laboratory by Dr. A. Aassime, was further developed by the author. All the unpublished data based on these techniques and presented in this thesis have been measured by the author.

# Contents

# 1 Introduction

## 1.1 History of ever smaller electronic circuits

Shortly after the invention of the bipolar transistor in 1947 planar junction technology was developed in order to get rid of the bulky three dimensional contacts. This technology adopted soon photolithography technique to fabricate planar semiconductor devices on a silicon chip. Silicon was chosen as a substrate material since it can be grown into large, low defect crystals and it can be easily oxidized to form an insulating barrier or a mask for doping. In the early 60's four transistors were interconnected together on a single silicon chip at Fairchild Semiconductor Corporation, USA. This very first circuit was followed soon by circuits with more and more transistors interconnected by aluminium or highly doped polycrystalline silicon. In 1964, the rapid exponential growth in the number of transistors on a single chip, encouraged an American Gordon Moore to plot this number versus time and to make a bold extrapolation known nowadays as Moore's law. According to this law, the number of integrated transistors on a single chip will double each year! Today, almost 40 years later when the number of transistors on a chip is several billions, and the Moore's law is still quite valid - the current definition of the law is that the number of transistors doubles every 18 months (Fig. 1). This incredible growth has been due to the vigorous research and development in processing and fabrication technologies.

Modern commercial circuits such as Intel Pentium micro processors have been fabricated by VLSI (Very-Large-Scale-Integration) or ULSI (Ultra-Large-Scale-Integration) technologies. The line between the two is vague. These commercial technologies are able to produce lines narrower than 0.3 $\mu$m [1]. The limitation is mainly due to the wavelength of the ultraviolet (UV) light, which is used to expose the desired patterns on the chip during a photolithography process. To reduce the linewidth still, one needs to replace photolithography by other methods. Those methods are here called nanofabrication, because they are able to produce features smaller than 100 nm wide in two or even in three dimensions.

Traditionally, the integrated circuits have been two dimensional. This is due to the planar fabrication processes that allow only one layer of devices to be processed on a chip. If the line width of the processing can be decreased from 1 $\mu$m to 100 nm in two dimensions, an equal chip area can accommodate 25 times more transistors [2]. This would satisfy Moore's law for five years.

A straightforward possibility of increasing the density of devices is to take an advantage of the third dimension. The principle is to process two dimensional functional elements first, then extract these elements and bond

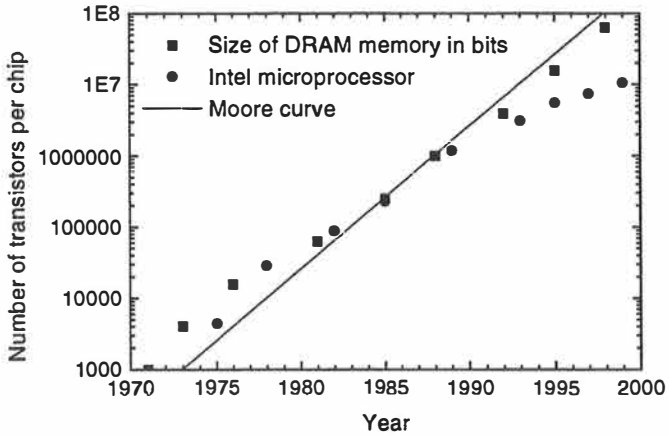


Figure 1: *Moore's curve and the evolutionary trend of exponentially increasing number of transistors on integrated circuits. The curve has been closely followed on the basis of active research and development of lithography systems. Higher densities in DRAM memory chips are due to their simpler design.*

them to a three dimensional aligned stack. The extraction of the elements can be done using an ion cut technique referred to as smart cut [3]. In micro mechanics, such bulk three dimensional micromachining fabrication processes [4] have been adopted parallel with the planar techniques. They allow fabrication of three dimensional devices through the chip.

There are several motives in squeezing the size of the devices on a silicon chip. The main one is money. In a large scale production, it does not cost more to produce one billion small transistors than to produce one big transistor on a chip! It is indeed much cheaper to integrate a device on a chip than to produce components separately and then wire them together. The integrated devices are also more reliable than devices put together of components. The more components one can integrate on a single chip the less chips needs to be fabricated and connected together. Smaller dimensions also lead to increasing speed and performance.

Another motivation to reduce the size of a device is the human curiosity. Quantum mechanical phenomena in structures where one, two or even all three dimensions have been reduced into a mesoscopic scale lead to completely new electronic devices. Mesoscopic physics studies the electron behavior in structures having dimensions from the microscopic to the macroscopic

scale. In small samples quantum mechanical interference starts to affect electron transport. Also, classical effects arising from electrostatic charging energy of single or just few electrons start to play a role in small conductors with small capacitance. To satisfy Moore's law, the size of minimum features will reduce to less than 100 nm during this decade. Then, quantum mechanical effects such as tunneling and particle wave interference have to be taken into account in device performance. If the gate length of a metal oxide field effect transistor is reduced to 90 nm, the oxide thickness will be only 4.5 nm and also the effective channel length may approach distances where tunneling is remarkable [5]. Quantized conduction in dimensionally confined structures [6] has been measured in 100 nm wide wires at 80 K [7]. Quantum well (QW) heterojunction [8] lasers [9] and quantum wire lasers [10] are typical applications of these effects. Also quantum mechanical tunneling combined with charging effects in small junctions has produced commercial applications [11]. Mesoscopic effects in superconductivity [12] are under rapidly increasing interest.

## 1.2 Basics of quantum mechanical tunneling

According to the classical theory, when a uniform beam of particles moves in a direction x with kinetic energy $E$ and approaches a potential barrier of energy $U$, the particles will get over the barrier if $E > U$ by converting a part $E - U$ of their kinetic energy into potential energy. If $E < U$ the probability of finding a particle behind the barrier is classically zero.

However, in quantum mechanics the state of a particle is described by a wave function and the beam of mono energetic particles moving into the x direction can be presented by a plane wave having a constant amplitude $A$:

$$\Psi(x) = A\exp(ikx) \tag{1}$$

where $|A|^2$ is the uniform density of particles and

$$k = \sqrt{\frac{2mE}{\hbar^2}} \tag{2}$$

where $E$ represents the kinetic energy of each particle of mass $m$. Due to this wave nature, some of the particles penetrate into the barrier even if $E < U$. Further, if the barrier is not infinitely high or wide some of the particles may penetrate through it. This is called quantum mechanical tunneling (see Fig. 2). The current density $j_I$ of the incident beam can be expressed by electron velocity and density [13]:

$$j_I = \frac{\hbar k}{m}|A|^2. \tag{3}$$

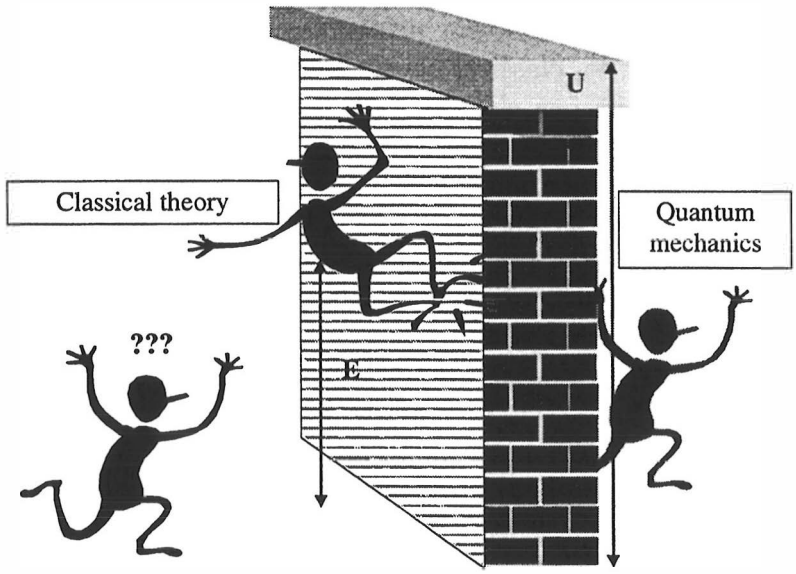


Figure 2: *A classical particle cannot cross a potential barrier U higher than its kinetic energy E. In quantum mechanics, however, it has a small probability to tunnel through a barrier of non-zero thickness and finite height.*

The beam splits due to the tunneling into the transmitted part with a current density $j_T$ and the reflected part with a current density $j_R$. Because of particle conservation, the sum of the two is $j_I$. The transmitted beam is presented by a plane wave with the same kinetic energy but with reduced amplitude $C$ (due to the reduced particle density). The transmission coefficient $T$, i.e., the probability that a particle penetrates the barrier can be defined as the ratio of transmitted and incoming beam intensities [13]:

$$T = \frac{j_T}{j_I} = \left|\frac{C}{A}\right|^2 = \frac{1}{1 + \left(\frac{k^2+\kappa^2}{2k\kappa}\right)^2 \sinh^2(\kappa a)} \tag{4}$$

where the decay constant

$$\kappa = \sqrt{\frac{2m}{\hbar^2}(U - E)} \tag{5}$$

is dependent on the height of the potential barrier and $a$ is the width of it. Typically, the barrier is very high or wide enough such that $\kappa a >> 1$. Then

$$T \approx \left(\frac{16E(U-E)}{U^2}\right) \exp(-2\kappa a). \tag{6}$$

Moreover, the exponential part dominates and often it is convenient to approximate $T$ by:

$$T \approx \exp\left(-a\sqrt{\frac{8m}{\hbar^2}(U-E)}\right). \tag{7}$$

Thus, the transmission probability decays exponentially when the barrier width or height increases. For a modern technology it is relatively simple to fabricate barrier structures thin enough to make the electron tunneling observable in transport measurements. This makes the tunneling one of the most important examples of quantum mechanical phenomena for applications.

## 1.3 Voltage biased tunnel junction

A tunnel junction may be considered as a capacitor with a very thin insulating layer through which electrons can leak due to quantum mechanical tunneling. Figure 3 presents schematically a voltage biased tunnel junction.

The total Hamiltonian for an ideally voltage biased tunnel junction can be written as [14]

$$H_{TOT} = H_{IN} + H_T. \tag{8}$$

The first term describes the energy states of the electrodes 1 and 2 and the second term is the tunneling coupling:

$$H_T = \sum_{kq\sigma} T_{kq} c^\dagger_{q\sigma} c_{k\sigma} + H.c. \tag{9}$$

where operator $c_{k\sigma}$ annihilates an electron with wave vector $k$ from the left electrode and operator $c^\dagger_{q\sigma}$ creates one with wave vector $q$ to the right electrode. Spin $\sigma$ conserves in tunneling. $T_{kq}$ is a matrix element corresponding to the tunneling coupling of this transition. Thus, $T_{kq}c^\dagger_{q\sigma}c_{k\sigma}$ transfers an electron from the left electrode to the right electrode with the probability $|T_{kq}|^2$ assuming that there is an electron at the state $E_k$ in the left electrode and that there is room for one, i.e., an empty state $E_q$ for an electron in the right electrode. The hermitian conjugate, $H.c$, describes the opposite process.

Due to the statistics of identical particles and Pauli exclusion principle, which states that no two identical fermions can be in the same quantum state, the probability $f(E_k, T)$ that there exists an electron at the state $E_k$ is determined by the Fermi-Dirac distribution [15]:

$$f(E) = \frac{1}{1+\exp[\beta(E-\mu)]}, \tag{10}$$

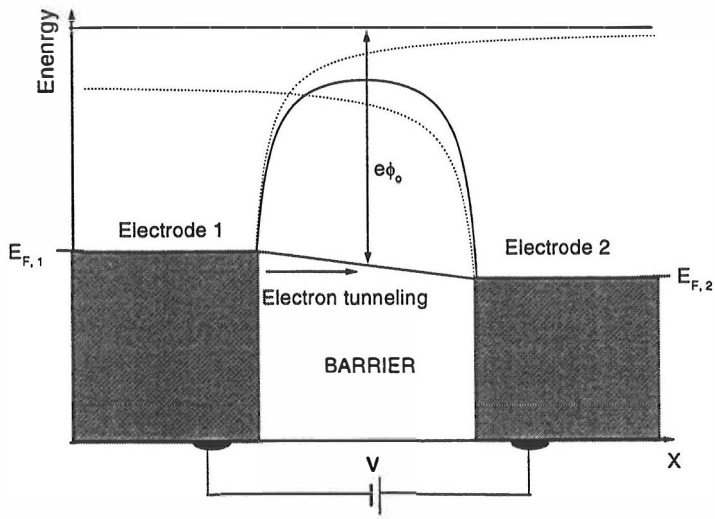


Figure 3: *The formation of a tunnel barrier in a voltage biased tunnel junction. The potential of an electron injected from a metal into a dielectric material is dependent on the distance from the surface (dotted curves). This is due to an image charge which induces barrier lowering, frequently referred to as Schottky barrier lowering [9]. The height of the barrier between two metal electrodes varies therefore strongly with the thickness of the barrier.*

where $\beta = \frac{1}{k_B T}$ is the inverse temperature and $\mu$ is the chemical potential. Naturally, the probability that a state $E_q$ is empty is $1 - f(E_q, T)$. At low temperatures the chemical potential approaches the Fermi energy $E_F$. At absolute zero temperature all energy states up to Fermi energy are filled. At finite temperatures there exist excitations from lower levels into upper levels and the occupation probability there increases according to Eq. (10). Many times it is practical to set the Fermi energy as a zero point of energy scale for calculations.

Due to the conservation of energy, tunneling can occur only if the energy difference $E_k - E_q$ equals the bias voltage $V$. At low temperatures and small bias voltages $|T_{kq}|^2$ may be considered independent of the energies $E_k$ and $E_q$, that is $|T_{kq}|^2 = T = \text{const}$. Then, the transition rate can be calculated by the Fermi golden rule [14]:

$$\Gamma(V) = \frac{2\pi}{\hbar} T \int_{-\infty}^{\infty} dE N_1(E) N_2(E + eV) f(E)[1 - f(E + eV)], \qquad (11)$$

where $E \equiv E_q$ and $N_1(E)$ and $N_2(E)$ are the densities of the states of the

left and the right electrode respectively. The densities of states are greatly dependent on the type of the carriers and the dimensionality of the system. This makes big differences between the current-voltage (IV) characteristics of different kinds of tunneling structures.

# 2 Metallic tunneling structures

## 2.1 Metal-insulator-metal tunnel junctions

The first metal-insulator-metal tunneling structures were fabricated already in 1960's [16]. The insulator material is usually natural oxide of the metal, but also so called artificial barriers have been fabricated [17, 18]. In the first case the bottom electrode is first deposited on a substrate and the surface is oxidized to achieve a tunnel barrier of desired thickness before depositing the other electrode on it. When an artificial barrier is used, the barrier material needs to be deposited in a separate process.

The conduction electrons in a metal electrode can be approximated by a free three dimensional electron gas (3DEG) for which $N(E) \propto \sqrt{E}$ [15]. However, the Fermi energies of metals are of the order of $10^5$ K $\sim$ 10 eV, i.e., much larger than the ambient temperature. In addition, if the applied voltages are some tens of millivolts, the densities of states of both the electrodes can be approximated by the densities of states at the Fermi level: $N_1(E) \simeq N_1(E_F)$ and $N_2(E + eV) \simeq N_2(E_F)$. In this case, according to Eq. (11) the IV curve of such a normal metal - insulator - normal metal (NIN) junction is linear and independent of temperature:

$$I(V) = e[\Gamma(V) - \Gamma(-V)] = \frac{V}{R_T}, \tag{12}$$

where

$$R_T = \frac{\hbar}{2\pi e^2 T N_1(E_F) N_2(E_F)} \tag{13}$$

is called tunnel resistance.

## 2.2 Metal-vacuum-metal, a scanning tunneling microscope

Perhaps the most celebrated application of solid state quantum mechanical tunneling is the scanning tunneling microscope (STM). It was invented by Binnig, Rohrer and Gerber in 1982 [19, 20]. Figure 4 shows its essential components.

Initially a small voltage is applied between the tip and the surface and the two approach each other. When the tip is at a distance of less than a nanometer from the surface, the tunneling current can be measured. According to equations (7), (12) and (13) the current is directly proportional to the applied voltage and it is exponentially dependent on the thickness of

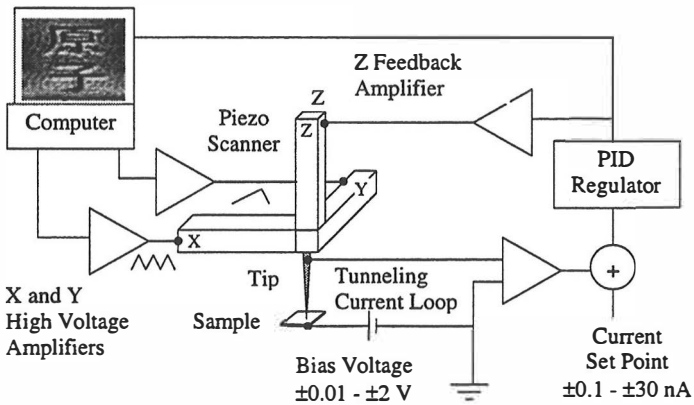


Figure 4: *Schematic diagram of the scanning tunneling microscope. Topographic information of the sample surface is extracted from the voltage that has to be applied to the piezo electric actuator in z direction, to keep the tip-sample tunneling current constant while the tip is scanned over the sample.*

the tunnel barrier, i.e., on the distance between the tip and the sample, and it may be expressed as:

$$I = c_1 V \exp(-c_2 \phi^{1/2} a). \tag{14}$$

Since the tunneling takes place through an air or a vacuum gap the barrier height is now the same as the work function $\phi$ of the material. The constant $c_1$ depends on the densities of the states of the tip and the sample at the Fermi level. The other constant $c_2 \approx 2\sqrt{2m/\hbar}$ =1.025 $(\sqrt{\text{eV}}\text{Å})^{-1}$ for an electron. Typical values of the work function for commonly used metals and, for example, silicon, are about 5 eV. The current decays then about exp(2)$\simeq$ 7.4 times for every Å at a constant applied voltage. The sample topography can be extracted as the vertical position of the tip needed to keep the tunneling current constant. The distance is regulated by a feedback loop formed by the tunneling current and the piezo ceramic transducer (z piezo). High resolution topography of a clean conductive surface can be indicated by the z-piezo voltage when scanning a very sharp conductive tip over the surface.

Typically, sample to tip distances of 3 to 10 Å are used in an STM. They are several times smaller than a barrier thickness of 20 - 30 Å of a

traditional tunnel junction, but the condition $\kappa a >> 1$ used to approximate the transmission probability $T$ is still quite well satisfied. At such short distances, however, the surface potentials of the tip and the sample start to overlap and this remarkably lowers the top of the potential barrier from the vacuum level, until finally at very small distances the barrier drops below the Fermi level. Also the local atom and electron structures and the forces between the tip and the sample become important [21]. At the distances less than about 3 Å the force between the apex atom of the tip and the topmost atom of the sample below the tip becomes repulsive. If the distance is further reduced the repulsive force deforms the structure accordingly and finally ruins the tip and the sample.

When the distance between the tip and the sample is higher than about 3 Å the force between them is attractive. The measured tunneling current follows approximately Eq. (14) and, thus, the tunneling resistance increases roughly by an order of magnitude per Å [21].

## 2.3 Field emission

When a distance between conductive electrodes, for example sample and tip in an STM becomes very large (> 10 nm) the interaction between them becomes negligible. However, by applying a large electric field the originally flat vacuum level bends down within a tunneling distance as can be seen in Fig. 5. The apparent width of the barrier is inversely proportional to the electric field and the electrons tunnel through the remaining barrier into free vacuum.

## 2.4 Superconductors

Tunneling in superconducting samples differs from that in normal metal structures because close to the Fermi level the density of states in the superconductor depends strongly on energy [22]. Besides quasiparticle tunneling, also Cooper pairs tunnel due to the Josephson effect.

The Cooper argument [23] states that even a very weak attractive interaction, resulting from virtual exchange of phonons, makes the Fermi energy of electrons unstable at low enough temperature. This leads to a formation of bound electron pairs called Cooper pairs. If the system has a large number of electrons, its ground state differs greatly from the Fermi level and the binding energy of one additional pair is negligible. The second quantization and a Hartree mean field approach then yield a ground state whose energy

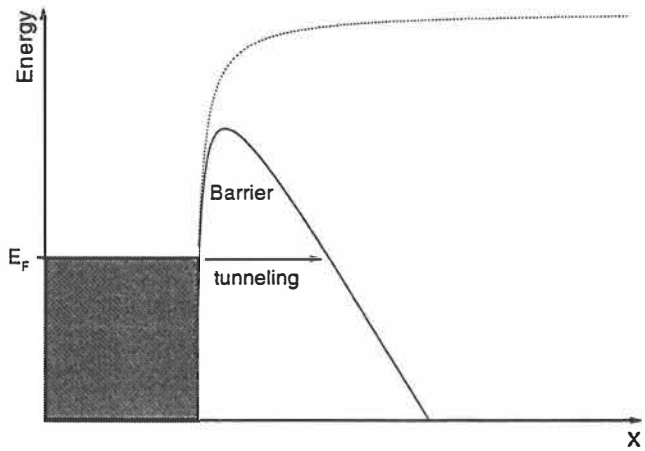


Figure 5: *Field emission. An electric field applied to a metal surface tilts the originally flat level to form a barrier of finite thickness. At strong fields electrons can tunnel through the remaining barrier into vacuum.*

relative to the energy of the Fermi level is [22, 24]:

$$< \Psi_0|H - \mu N_{op}|\Psi_0 >= 2\sum_k \xi_{\mathbf{k}} v_{\mathbf{k}}^2 + \sum_{kl} V_{\mathbf{kl}} u_{\mathbf{k}} v_{\mathbf{k}} u_{\mathbf{l}} v_{\mathbf{l}} \tag{15}$$

where the Hamiltonian operator includes the energies of single particles and the pairing interaction. The term $-\mu N_{op}$ sums the chemical potential $\mu$ (or Fermi energy when $T << T_F$, the Fermi temperature) over the occupied states and, thereby it shifts the zero of the kinetic energy to the Fermi energy: $\xi_{\mathbf{k}} = \epsilon_{\mathbf{k}} - \mu$. The probability of the state $(\mathbf{k}, -\mathbf{k})$ being occupied (empty) is $v_{\mathbf{k}}^2$ ($u_{\mathbf{k}}^2$). $V_{\mathbf{kl}}$ is the attractive potential between the electrons in a Cooper pair.

Minimizing the ground state energy of Eq. (15), taking into account that $v_{\mathbf{k}}^2 + u_{\mathbf{k}}^2 = 1$, gives:

$$v_{\mathbf{k}}^2 = \frac{1}{2}\left(1 - \frac{\xi_{\mathbf{k}}}{E_{\mathbf{k}}}\right), \tag{16}$$

where $E_{\mathbf{k}} = (\Delta^2 + \xi_{\mathbf{k}}^2)^{\frac{1}{2}}$ is the quasiparticle excitation energy. The minimum excitation energy $E_{\mathbf{k},min} = |\Delta|$ is found at the Fermi surface where $\xi_{\mathbf{k}} = 0$. Thus, $\Delta$ is an energy gap for excitations in a superconductor and it is equal to the binding energy per electron in a Cooper pair.

The reduced density of states of quasiparticle excitations, $N_s(E)$, can then be written assuming a constant $N_n(0)$, the normal metal density of states in

a narrow energy region $\xi$ around the Fermi energy:

$$N_s(E) \approx \frac{E}{\sqrt{E^2 - \Delta^2}} N_n(0), \tag{17}$$

when $|E| > \Delta$. If $|E| < \Delta$ the density of states of quasiparticle excitations is zero, but just at the gap it diverges to infinity as can be seen from Eq. (17).

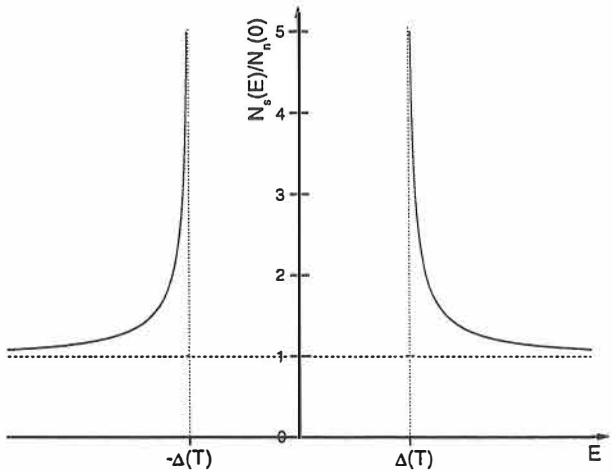


Figure 6: *The density of states in a superconductor diverges at $\pm\Delta$. Within the gap, $-\Delta < E < \Delta$, the density of states is zero.*

If one electrode of a tunnel junction is normal metal and the other one is superconductor (Normal metal-insulator-superconductor structure, NIS) the tunneling rate can be approximated by replacing the density of states $N_2(0)$ in Eq. (11) by that of Eq. (17). Equation (11) gives then the tunneling current [22]:

$$\begin{aligned} I_{ns} = & \frac{1}{eR_T} \int_{-\infty}^{-\Delta} \frac{E}{\sqrt{E^2 - \Delta^2}} [f(E) - f(E + eV)] dE \\ & + \frac{1}{eR_T} \int_{\Delta}^{\infty} \frac{E}{\sqrt{E^2 - \Delta^2}} [f(E) - f(E + eV)] dE. \end{aligned} \tag{18}$$

At very low temperatures $T << T_c$, where $T_c$ is the superconducting transition temperature, there are practically no thermal quasiparticle excitations and so there cannot be tunneling unless the biased difference in chemical

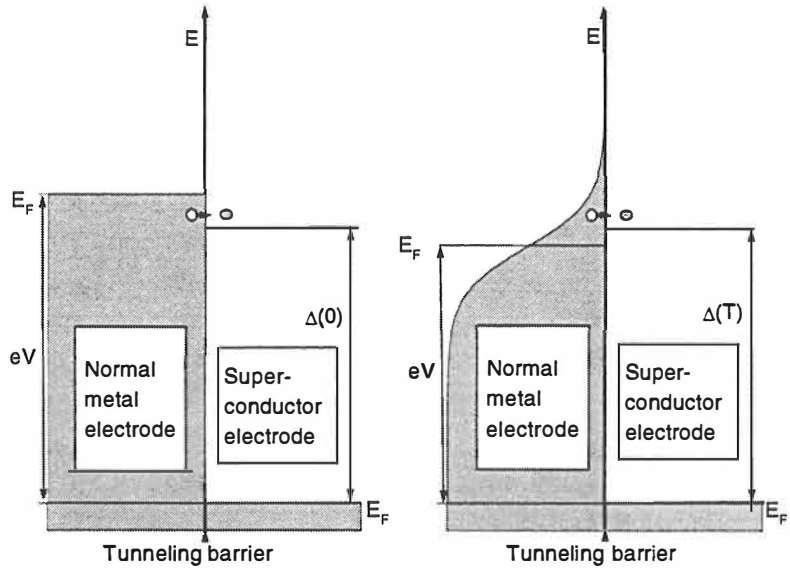


Figure 7: *At absolute zero temperature the bias voltage across an NIS junction has to exceed the energy gap of the superconductor for tunneling current to flow (left). At finite temperatures the current can flow also at lower bias voltages due to thermal excitations (right).*

potentials between the opposite electrodes exceeds the energy gap of the superconductor: $e|V| \geq \Delta$ (Fig. 7 left). At the absolute zero temperature the Fermi function is a step function which gives the tunneling current:

$$I_{ns,T=0} = \frac{1}{eR_T}\int_{\Delta}^{eV} \frac{E}{\sqrt{E^2-\Delta^2}}dE = \frac{\frac{\Delta}{e}}{R_T}\sqrt{\left(\frac{eV}{\Delta}\right)^2 - 1}\,, \quad e|V| > \Delta. \quad (19)$$

Current versus voltage characteristics of a tunnel junction between normal metal and superconducting electrodes at $T = 0$ is presented by the solid curve in Fig. 8 . When the difference in chemical potentials is much larger than the superconductor energy gap the tunneling current approaches the current of a NIN junction: $I_{ns} \simeq V/R_T$ (Eq. (12), dotted line in Fig. 8).

At finite temperatures the thermal quasiparticles can tunnel at subgap voltages (Fig. 7 right), turning the sharp gap edge of the IV characteristics into an exponential tail. This is illustrated by the dotted curve in Fig. 8. When the temperature is such that the thermal energy of excitations is much below the energy gap, the IV curve depends only on the temperature of electrons in the normal metal and the states in the superconductor electrode can still be considered fully occupied below the energy gap and completely empty above it [25]. Then the tunneling takes place from the normal metal

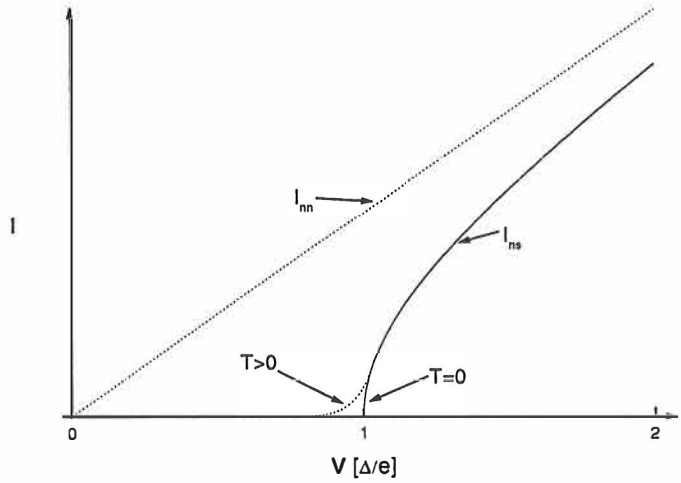


Figure 8: *At bias voltages below the energy gap the current through an NIS junction is dependent on temperature. At high voltages the current approaches that of an NIN tunnel junction.*

states above the gap edge (Fig. 7) (or to the empty normal metal states below the gap edge with an opposite bias) and the tunneling current is given by:

$$I_{ns} = \frac{1}{eR_T}\int_{\Delta}^{\infty} \frac{E}{\sqrt{E^2-\Delta^2}} \frac{1}{\exp\left(\frac{E-eV}{k_BT}\right)+1} dE. \tag{20}$$

When the voltage is such that $0 << eV < \Delta$, the current can be approximated by [26]:

$$I_{ns} \approx I_0 \exp\left(\frac{eV-\Delta}{k_BT}\right), \tag{21}$$

where $I_0 = (2eR_T)^{-1}(2\pi\Delta k_BT)^{1/2}$. If the junction is biased at a constant current the junction can be used as a thermometer with the temperature responsivity:

$$\frac{dV}{dT} \approx \frac{k_B}{e}\ln\left(\frac{I}{I_0}\right). \tag{22}$$

For typical values of bias current $dV/dT \simeq$-0.4 $\mu$V/mK [27]. Since electron and hole excitations in superconductors have equal energies the current does not depend on the direction of the bias voltage.

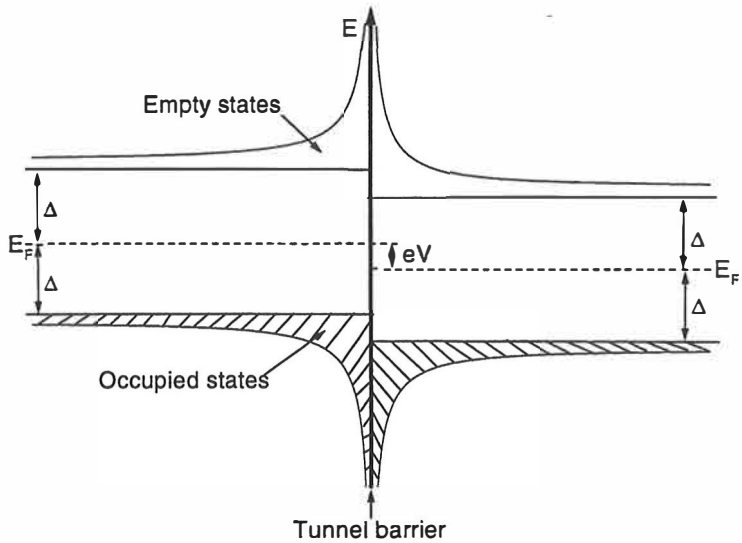


Figure 9: *An energy diagram of an SIS tunnel junction of two similar superconductors ($\Delta_1 = \Delta_2 = \Delta$) biased at a sub gap voltage at T=0.*

When both electrodes of a tunnel junction are superconductors (SIS junction, Fig. 9), both densities of states in Eq. (11) have to be replaced by superconducting densities of states of Eq (17). The quasiparticle tunneling current then becomes:

$$I_{ss} = \frac{1}{eR_T}\int_{-\infty}^{-\infty} \frac{N_s(E)}{N_1(0)}\frac{N_s(E+eV)}{N_2(0)}[f(E) - f(E+eV)]dE. \qquad (23)$$

Again at absolute zero temperature the tunneling current cannot flow unless $eV > \Delta_1 + \Delta_2$ where $\Delta_1$ and $\Delta_2$ are the superconducting energy gaps of the electrodes 1 and 2 respectively.

When the bias voltage reaches the energy gap, there is a sharp jump in the current since an infinite amount of occupied states on one side of the junction match with a similar singularity of empty states on the other side of the junction. Again, at $T > 0$ thermally excited quasiparticles can tunnel at voltages less than the sum of the energy gaps of the superconducting electrodes. This subgap current has a maximum value when $eV = |\Delta_1 - \Delta_2|$. At this voltage the thermal quasiparticles on one side of the junction level with the peaked density of empty states on the other side of the junction [22]. Measured IV characteristics in Fig. 10 for superconducting tunneling structures also show a current peak at zero voltage. This supercurrent is due

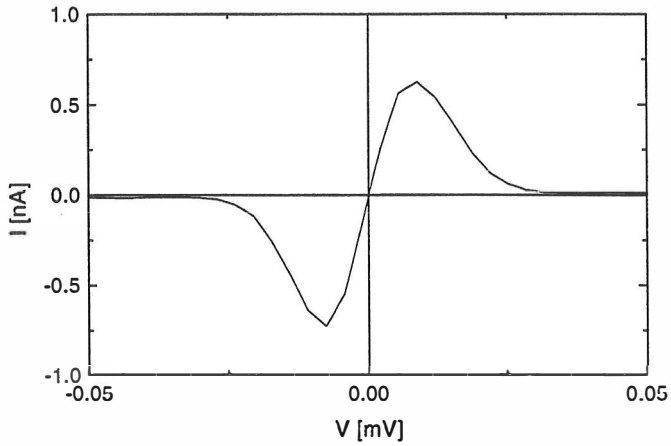


Figure 10: *An experimentally measured IV curve for supercurrent of a mesoscopic aluminium-aluminiumoxide SISIS structure. The experimental setup and the sample fabrication using an etched hole in a thin silicon nitride membrane as a mask will be described in chapters 5 and 7.*

to the tunneling of Cooper pairs (Josephson current).

# 3 Mesoscopic tunnel junctions

Classically, when there is no electrical transport through a barrier, the junction with a capacitance of $C$ may be charged with a charge $Q = CV$ by applying an external voltage $V$ over the junction. The charge $Q$ arises from a redistribution of electrons in the metallic electrodes relative to the positive background charge. The change of the charge in this kind of a classical capacitor is continuous even on an elementary charge scale.

If the tunnel resistance $R_T$ of the junction is large compared to the resistance quantum $R_K = h/e^2 \simeq 25.8$ k$\Omega$ the quantum fluctuations of charge across the junction are small. Then, in a quantum mechanical tunneling a discrete charge $e$ moves from an electrode to the other and the change in energy for this process is the charging energy $E_C \equiv e^2/2C$ [14]. For Cooper pairs the resistance quantum is $R_Q = h/4e^2$ to take into account the charge $2e$ of Cooper pairs.

The development in nanofabrication and cooling techniques has made it possible to perform experiments with tunnel junctions with such a small capacitance that the charging energy of a junction is larger than the thermal energy $k_BT$. As an example, a metallic tunnel junction with an area of 100 x 100 nm$^2$ and a typical oxide barrier thickness of 1 nm has a capacitance of the order of 1 fF. Then, the charging energy is of the order of $10^{-4}$ eV, which corresponds to a temperature of about 1 K - easily and cheaply achieved by, e.g., a $^3$He/$^4$He dilution refrigerator [28]. Ultrasmall tunnel junctions with this low capacitance are typically constrictions of a 2DEG in semiconductor heterostructures or they may be metallic junctions. Small metallic junctions may be fabricated by a lithographic method, they may exist in granular films or between small particles embedded in oxide layers, or the junction can exist between a scanning probe microscope tip and a conducting sample. One or both of the electrodes may be a superconductor or a semiconductor.

## 3.1 Coulomb blockade

Equation (12) gives a temperature independent linear current-voltage characteristic for a tunnel junction. This is Ohm's law with junction resistance $R_T$. The equation holds for a junction coupled to an ideal voltage source which recharges the capacitance of the junction instantaneously upon tunneling. In reality, however, a tunnel junction is coupled to a voltage source by wires which always have some impedance. Usually this impedance is large enough to inhibit the fast recharging of the junction after the tunneling. When this is the case, conservation of energy says that the charge can tunnel only when the electron gains energy from the voltage source across the junction at least

as much as the charging energy is:

$$eV \geq \frac{e^2}{2C}. \tag{24}$$

The suppression of tunneling current at voltages below $e/2C$ at low temperatures is called Coulomb blockade (CB). At high bias voltages the current-voltage characteristics of the tunnel junction approach Eq. (12), but with an offset voltage of $V_{OFF} = e/2C$.

If the thermal energy of the electrons $k_BT$ is higher than the charging energy of the junction, thermal fluctuations will mask the Coulomb Blockade phenomenon.

The tunneling of Cooper pairs in mesoscopic superconducting samples at very low temperatures is also affected by charging effects [29]. The supercurrent-voltage curve for mesoscopic samples at absolute zero temperature shows a peaked value of supercurrent at zero voltage when the impedance of the external circuit is small [14]. If the impedance is high the supercurrent increases with small voltages leading to a peak value at finite voltage. At non-zero temperatures the peak is broadened by thermal fluctuations.

## 3.2 Quasiparticle tunneling

In addition to the Cooper pairs, also quasiparticles can tunnel in Josephson junctions. As before this quasiparticle tunneling can be treated as tunneling in normal metal junctions remembering that the quasiparticle density of states depends strongly on energy near the gap energy of the superconductor. The quasiparticle current through a voltage biased Josephson junction can be calculated by Eq. (23).

At zero temperature the current-voltage curve for quasiparticle tunneling is shifted - in addition to the effect of the superconducting energy gap - by a voltage of $e/2C$ due to Coulomb blockade. As the resistance of the environment approaches zero, the zero temperature curve approaches the voltage biased case near the energy gap, but the linear part of the curve at high voltages is still shifted exhibiting a Coulomb gap [14, 22, 30].

At non-zero temperature the superconductor gap is smeared due to the thermal quasiparticle excitations which can tunnel at subgap energies, turning the sharp gap edge of the IV characteristics into an exponential tail, as described earlier. This subgap current increases with an increasing external resistance. This is in contrast to the behavior at high voltages and that in normal metal tunnel junctions [14, 30].

When energy gaps of the superconductors at different sides of the tunneling barrier are unequal, there will be a negative resistance region between

bias voltages of $V = (\Delta_2 - \Delta_1)/e$ and $V = (\Delta_2 + \Delta_1)/e$. This is due to the difference in the density of states of quasipartricles at the two sides of the junction [16].

## 3.3 Double junction structures and a single electron transistor

A system of two tunnel junctions connected in series differs greatly from a single junction because there is a metallic island between the two junctions. Here we consider a symmetric system of two mesoscopic tunnel junctions at low temperature, such that, $E_C >> k_B T$. The metallic island connecting the junctions has a capacitance $C_L + C_R \simeq 2C$ to the environment. The indices L and R refer to the left and the right junction respectively. One additional electron on the island changes the energy now by an amount $E_C$. At zero temperature and low bias voltages, it is not possible for an electron to tunnel into the island and there is a sharp threshold voltage for the onset of current which is completely blocked in the Coulomb gap region. In reality, however, quantum fluctuations, non-zero temperature and co-tunneling, i.e., virtually simultaneous tunneling in the two junctions, partially wash out Coulomb blockade.

If a gate voltage $V_g$ is coupled to the island with a capacitance $C_g$, a single electron transistor (SET) is found. The charging energy of the SET of $n$ electrons on the island is given by [14]

$$E_{CH}(n, Q_g) = \frac{(ne - Q_g)^2}{2(C_L + C_R + C_g)}, \tag{25}$$

where $Q_g = C_g V_g$ is is the gate charge induced on the island by the gate voltage and $n$ is the number of electrons on the island. The lowest electronic energy for having $n$ excess electrons on the island forms then a parabola as a function of $Q_g$. The parabolas for successive values of $n$ are displaced by $e$. They cross when $Q_g$ assumes half integer values of $e$. Then, the energy is the same for $n$ and $n$+1 electrons and the electrons can enter and leave the island without energy barrier. The current voltage curve of the SET is linear and there is no Coulomb blockade effect in such a case. Generally, the energy needed for a tunneling of an electron to increase the island charge from $ne$ to $(n+1)e$ is [14]

$$E_{CH}(n+1, Q_g) - E_{CH}(n, Q_g) = \left(n + \frac{1}{2} - \frac{Q_g}{e}\right) \frac{e^2}{C_L + C_R + C_g}. \tag{26}$$

Thus, changing $V_g$ controls the Coulomb gap which blocks the current at low bias voltages and at very low temperatures. This leads to periodic

current peaks separated by $e$ along the $Q_g$ axis. Under these conditions the current is very sensitive to variations of the gate voltage and changes of $Q_g$ by even fractions of an electronic charge can be resolved. Gated tunnel junction arrays can be used as an electron pump, which can be used as a current source [31] or as very sensitive electrometers down to $<10^{-4}e/\sqrt{\mathrm{Hz}}$ noise level [32].

At finite temperatures the thermal energy of electrons allows tunneling current to flow in the Coulomb gap region. When the temperature is such that $E_C >> k_BT$, the Coulomb blockade still dominates, but thermal fluctuations start to round the sharp edges of the current-voltage characteristics near the Coulomb gap edge. In the high temperature limit, $E_C << k_BT$, the full width of the conductance drop, $V_{1/2}$, divided by temperature is a universal number for all arrays of the same number $N$ of similar junctions in series [33]:

$$V_{1/2} \simeq 5.44\frac{Nk_BT}{e}. \tag{27}$$

Since the half width is directly proportional to temperature, depending only on the fundamental constants of nature and the number of junctions, it is a primary measure of temperature. For diagnostics, a measurement at a known temperature gives a way to verify the number of junctions in an array. The depth of the conductance drop normalized by the asymptotic, high voltage value $G_T \equiv 1/NR_T$, is given by [33]

$$\frac{\Delta G}{G_T} = \frac{N-1}{3N}\frac{\frac{e^2}{2C}}{k_BT}. \tag{28}$$

This gives a secondary thermometer since a calibration is needed for the capacitance $C$. On the other hand, the calibration gives the capacitance of the junctions which depends on the junction area to the barrier thickness ratio.

When the size of a metallic island between the tunnel junctions is very small the spatial confinement leads to reduced density of states similarly to what happens in semiconductor heterostructures. Further, if the size of an island is of the order of magnitude of 10 nm in diameter, discrete energy levels similar to those in semiconductor quantum dots can be resolved experimentally at low temperatures. Then, electrons start tunneling when the bias voltage is such that the Fermi level in the leads equals to one of the discrete levels allowing an electron to tunnel into or out of the island. When the bias voltage is increased, the current through the island increases in steps every time the voltage is such that the Fermi levels match a new state.

If the size of an island is smaller than both the superconducting coherence length and the magnetic field penetration depth, a ground state with Cooper

pairs is still possible as long as the spacing of discrete energy levels is smaller than the superconducting energy gap [34]. The tunneling current through discrete energy states of a superconducting sample has singular peaks instead of the step increase in current of a normal metal sample. This is due to the peaked density of quasiparticle states. The peaks are also sifted in voltage from the corresponding normal metal steps due to the superconducting energy gap $\Delta$.

## 3.4 Superconducting SET

The electrodes and the island may also be in the superconducting state. Because the island is electrically isolated from its surroundings, it has a fixed number of particles. Due to the pairing nature of superconductivity an island having an even number of electrons has different properties than an island with an odd number of electrons. The odd electron in the island has to occupy an unpaired quasiparticle state which is above the ground state by $\Delta$. This lifts energy versus $Q_g$ parabolas for an odd number of electrons. If the gap is smaller than the charging energy of the island, then at low temperatures and at low applied bias voltages the current through the island alternates between long and short cycles with a $2e$ periodic dependence on the $Q_g$. When the superconducting gap is greater or equal to the charging energy, the quasiparticle tunneling is suppressed, and the island charge can change only by $2e$ as a result of Cooper pair tunneling. If only the island is superconducting the two electron tunneling is called Andreev reflection. In that case a normal metal electron reflects in the junction as a hole and propagates as a Cooper pair in the superconductor side of the junction or vice versa.

## 3.5 Metal particles embedded in oxide layers

Charging effects may also be seen in structures made by nano oxidation. Narrow titanium or aluminium wires can be locally oxidized using ambient humidity and the electric field applied by the tip of an STM or an atomic force microscope (AFM) [35], for example. Fabricated structures are typically of the order of 10 $\mu$m long, 100 nm wide and 10 nm thick. The IV curves resemble those of one dimensional (1D) arrays of small tunnel junctions [14]. This is probably due to the formation of a metal oxide mesh during the anodisation. Tiny metallic grains, which are separated by thin oxide barrier, are acting like an array of small conductive islands.

# 4 Fabrication of small tunneling structures

## 4.1 Lift-off lithography process

The lithographic process typically consists of the definition of a desired pattern into a resist layer and transfer of this pattern into a conducting or a dielectric film. Prior to the definition of the pattern, the resist film has to be deposited on a cleaned substrate. The pattern is then formed by defining a latent image at the resist film by an exposure tool and developing this image into a three dimensional relief structure to be used for pattern transfer.

Depending on the chemical properties of the resist material or in some cases the dose, the exposed areas of the film are removed (positive resist) or left behind (negative resist) by a developing solvent. The patterns can then be transferred by depositing a layer of desired material through the windows created. Finally, the extra material is lifted off with the resist film in a solvent. Alternatively the material may have been deposited prior to the film on the substrate and extra material is selectively etched away through the windows. In this work the latter technique has been used only for chromium mask fabrication for photolithography to fabricate large scale (100 $\mu$m) structures and it will not be considered in details here. In semiconductor industry the film structures can also be used as a doping mask to create areas of different electrical properties in the substrate.

### 4.1.1 Substrate cleaning

The substrate to be used for a lithography process has to be perfectly clean. Usually this is the case when wafers from suppliers are properly handled. Then the cleaning of the substrate is an unnecessary additional processing step which can lead to more contamination in the worst case.

Sometimes a process, a human personnel or a laboratory surrounding may cause contamination of the substrate. This includes most commonly organic contamination from vacuum pumps and humans or inorganic films such as oxides and moisture. The contamination usually results in poor uniformity and adhesion of the film and in pointlike defects.

If the source of contamination cannot be eliminated, the substrates have to be cleaned prior to the resist deposition. In our case, a typical process to remove organic contamination and small particles is to flush the sample by a pressure spray of organic solvent such as acetone. For thicker contamination layers dipping into the solvent and ultrasonic or thermal agitation may preceed the flushing. A good trick is to expose the substrate to the vapour above boiling solvent. The hot fresh solvent vapour condenses on

the substrate and washes it while the contaminants accumulate in the liquid phase. Organic residues can also be removed by high temperature baking or by oxygen plasma cleaning [36].

The inorganic oxide contamination can be removed by plasma dry etching using freon and oxygen [37] or by wet etching [4] followed by rinsing in deionized water.

We realized, that the condensed moisture can be a serious problem. It may spoil the quality of the deposited resist film and it seems that in some cases the water molecules may even be transferred from substrate and resist into the final structures affecting their properties as well. The moisture can be removed by baking the sample on a hot plate or by alcohol spray flushing. It should be noticed, however, that the temperature of the substrate is one of the key parameters of resist film deposition and it should be kept constant from film to film. Evaporating alcohol also cools down the substrate leading to additional condensation of moisture in a humid surrounding.

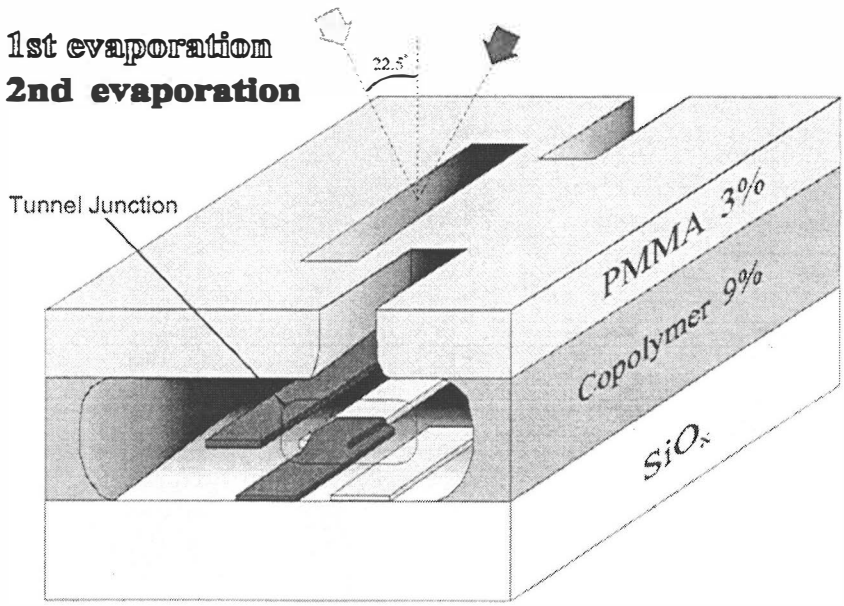


Figure 11: *A basic double layer resist on an oxidized silicon substrate demonstrating shadow angle evaporation technique. Large undercut allows fabrication of suspended bridge structures. First the bottom electrodes are evaporated in an angle and a tunnel barrier of natural oxide is grown on them. Finally, the top electrodes are evaporated in another angle to achieve a small tunneling structure at the overlap area.*

The methods given above are examples of solutions of common contami-

nation problems. These methods are commonly used in semiconductor industry and they have been adopted in nanofabrication, too. Usually the cleaning process has to be tailored according to demands of the specific process.

### 4.1.2 Resists

In conventional electron beam lithography (EBL) double layer resist films are frequently used to achieve a stronger undercut pattern which is helpful in subsequent lift-off processing. A basic double layer resist system can be seen in Fig. 11. We have been using positive polymethylmetacrylate methacrylicacid P(MMA-MAA) copolymer as a highly electron sensitive bottom resist layer, which can be exposed at a much lower dose than the top layer of polymethyl methacrylate (PMMA) [38]. This copolymer is then easily exposed by backscattered electrons over a larger area than the top layer film. This combination of resists is the most common and a simple choice.

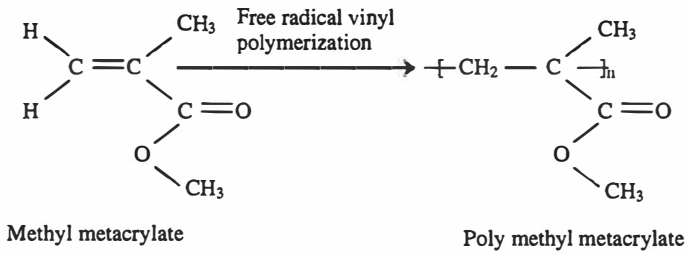


Figure 12: *Formation of a PMMA (polymethyl metacrylate) molecule by a free radical polymerization.*

An advantage of P(MMA-MAA) is its easiness in the process: it is not sensitive to visible light. Aside from normal cleaning it does not need any additional surface processing, having still an excellent adhesion to most surfaces and several solution concentrations can be deposited on a substrate, allowing a wide range of film thicknesses.

PMMA is one of the first resist materials reported for EBL [39]. It is a polymer which forms in vinyl polymerization process of the free radical. Monomer methylacrylate molecules form long chains by splitting the double carbon to carbon bonds as presented in Fig. 12. PMMA is a hard and transparent plastic which is also known as plexiglas when used as a material for bathtubs or protective windows, for example. PMMA is available for EBL in several high molecular weight forms. PMMA suits very well for nanofabrication as it is still considered as one of the highest resolution resist materials: The resolution of PMMA can be better than 10 nm, which is the size of a PMMA molecule [40].

### 4.1.3 Deposition of resist films

The next lithography step is to cover the cleaned substrate by a radiation sensitive resist film. The deposited film has to be uniform, smooth and defect free over the entire substrate. The first step is to introduce the resist material into a clean and particle free solution. This is achieved by filtering the solution through 0.2 $\mu$m PTFE (teflon) filters.

In spin casting the dissolved material is poured onto the substrate which is then rotated at constant speed of a few thousand revolutions in minute. As the solution spreads, the volatile solvent evaporates leaving a uniform thin film of resist material on the substrate. The thickness of the deposited film layer depends on the rotation speed but also on the molecular weight of the resist film material, solution concentration and viscosity. Typically, the spin cast film thickness ranges from 0.03 to 50 $\mu$m [4].

In addition to the problems with humidity, which were described earlier, there are other reasons to keep the temperature of the substrate constant. Polymer chains exist in solution as coils whose average size depends on the temperature of the solvent. As temperature drops, these coils shrink until they precipitate, starting from the largest, i.e., the highest molecular weight coils. This may lead to pinholes or larger opaque spots in the film. On the other hand, if the temperature is too high the solvent evaporates too rapidly resulting in a fast increase in viscosity and nonuniform film thickness.

For our double layer resist films (Fig. 11) we have first used a 9% solution of P(MMA-MAA) in acetic acid. When spun by 6000 RPM it forms a 280 nm thick film on a substrate. The sample is then baked on a hot plate at 170 $^{o}$C for 45 min. The top layer is 400 nm thick film of PMMA. This is fabricated by spinning a 3% solution of 940 000 u PMMA in chlorobenzene at a speed of 3000 RPM.

The film is finally baked at 170 $^{o}$C for 1 hour. The baking is to remove residual solvent from the film, but also to anneal built-in stresses due to shear

forces applied by the spinning process. The baking temperature has to be above the glass transition temperature of the material for polymer chains to become mobile to flow under the stress. In time the film will anneal to its most stable state energetically. Residual stress in the film may result in poor adhesion and nonuniformity in subsequent chemical and physical processes. The baking time has to be long enough for solvent molecules to diffuse out of the polymer structure. Thus the baking temperature is dependent on the film material and baking time is dependent on the film thickness. Prior to baking a deposited resist film is very attractive for any ambient contamination. That is why the route from the spinner to the hot plate or the oven should be made as short and as clean as possible.

### 4.1.4 Langmuir-Blodgett deposition

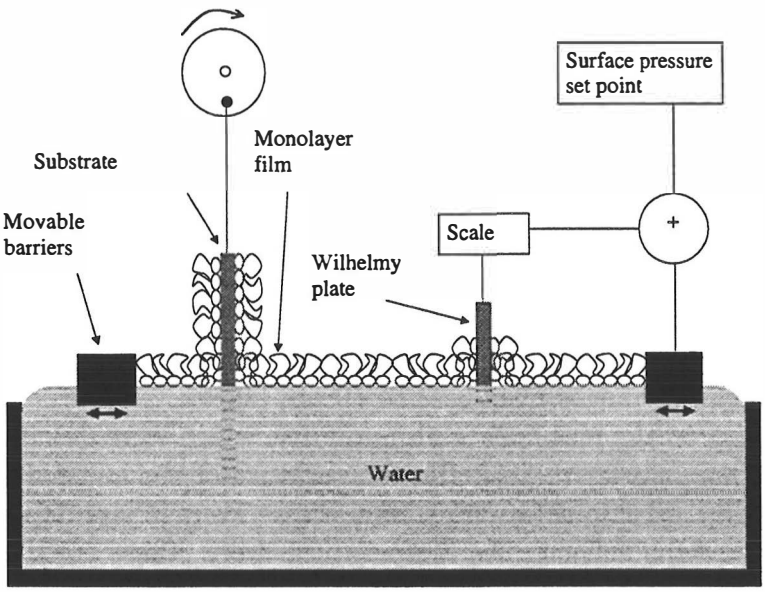


Figure 13: *A principal drawing of a Langmuir-Blodgett apparatus. A film thickness of one monolayer is sustained by a feedback loop from a Wilhelmy plate to movable barriers. The film is collected onto a substrate monolayer by monolayer by dipping it into water.*

A technique we have used to deposit extremely thin PMMA films is based on early observations of thin films of oil on water surface [41, 42]. Experimental research of floating films was continued by Irving Langmuir who developed a method to measure the surface pressure of a film detecting a deflection of a floating barrier separating a clean water surface from the area

covered by the film [43, 44]. The first attempts to transfer a floating monolayer of material onto a solid surface was reported by Katherine Blodgett in 1934-35 [45, 46]. Such built up monolayer structures are now referred to as Langmuir-Blodgett (LB) films. Since the characteristics of LB films such as the thickness and molecular arrangement may be controlled on the molecular level, they are expected to be widely applied in molecular and bioelectronics.

A schematic drawing of a typical Langmuir-Blodgett apparatus can be seen in Fig. 13. It consists of a trough equipped with movable barriers and a unit to measure surface pressure. The trough is filled with water, and a small amount of resist solution is dropped on the water surface. The water-immiscible solvent makes the solution spread rapidly to cover the whole area of the water surface between the barriers. The long PMMA molecules have hydrophilic C=O heads (see Fig. 12), which are directed to the water surface while the hydrophobic chain is lying parallel to the surface [47]. As the solvent evaporates the PMMA chain coils open and form a two dimensional monolayer film.

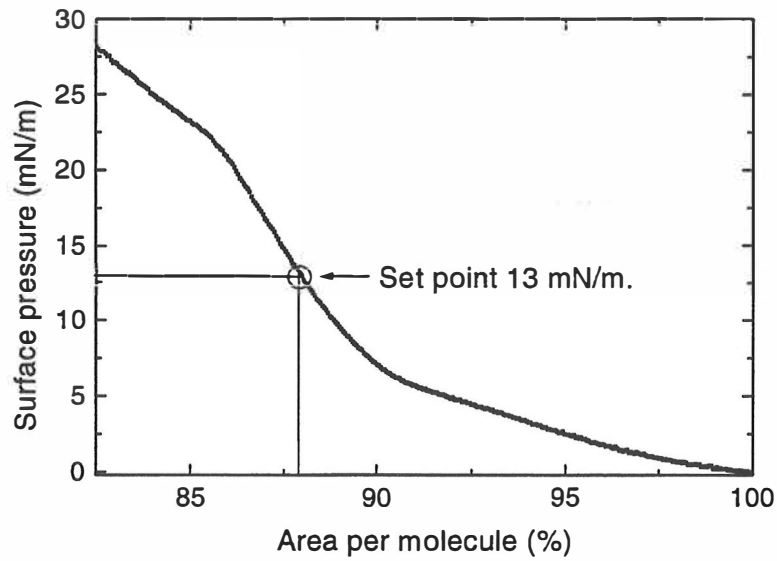


Figure 14: *Surface pressure measured as a function of the area of a PMMA film. The horizontal axis has been scaled to the value where the molecules just start to interact (100 percent). A typical film deposition took place in the middle of the range of compression of a monolayer, with a surface pressure of 13 mN/m.*

If the distance between neighboring molecules is large, the interaction between the molecules is neglible. When the area of the water surface is reduced by moving the barriers, the molecules begin to repel each other. The magnitude of this repulsion per unit length is defined as surface pressure $\Pi$. This surface pressure tends to reduce the surface tension of the pure water which is due to the excess free energy at the liquid surface [48]. For pure water at room temperature and atmospheric pressure (NTP) the surface tension is 73 mN/m. A measured surface pressure for a PMMA resist film versus the film area can be seen in Fig. 14. While reducing the film area, the surface pressure first starts to increase slowly as the hydrophobic tails of the resist molecules start to rise and the molecules form an ordered two dimensional array. When this array has been completed at a surface pressure of 6 mN/m there is an increase in the slope of the curve. When the area is further reduced, the surface pressure increases rapidly as the ordered molecules approach each other. At the surface pressure of 21 mN/m the two dimensional monolayer collapses and disordered multilayers are formed.

Our LB trough is made of PTFE as it needs to be inert against organic solvents and inorganic acids and it should not release impurities into the water. PTFE is easy to keep clean as it is a hydrophobic material. Also the movable barriers are preferably made of PTFE. The surface pressure can be measured by the Wilhelmy method [49]. In this method a so called Wilhelmy plate is hanging from a very sensitive balance and partially immersed into the water. The forces acting on the plate are gravity and surface tension of the water downward and buoyancy and surface pressure of the film upwards. The balance is set to show zero when immersed into clean water, and thus it gives directly the surface pressure as the film dropped on the water starts to push the plate upwards. The balance controls the motor moving the barriers, keeping the set surface pressure by reducing the area as the film is partially transferred onto the substrate dipped into water.

### 4.1.5 Electron exposure

A traditional way in lithography is to cover the baked resist film on a wafer by a mask which protects the areas that are not to be attacked, and then expose the mask to radiation. The radiation is typically ultraviolet light, but also x-rays are used in some applications. Because the whole wafer can be exposed in a single shot this is indeed the fast way for large scale production. A similar system has been tested also with electron beam lithography [50]. Nanoscale structures cannot be fabricated by the diffraction limited optical lithography. X-ray lithography systems using radiation of 4-20 Å wavelength have been used to produce 20 nm wide lines [51] but low brightness sources

demand very sensitive resists and high brightness sources such as synchrotron storage rings [51, 52] or laser induced plasma sources [53] are very expensive. Another problem with the x-ray lithography is the fabrication and alignment of masks.

In conventional EBL a desired pattern is exposed by a direct write of a focused electron beam. This method is much slower than the contact printing described above, but no physical mask is needed, which makes it very useful for individual samples but also for small quantity production such as mask making for photolithography. Since the wavelength of the accelerated electrons is about four orders of magnitude shorter than that of UV light, the diffraction is not limiting the resolution.

In an electron exposure, interactions of the electrons with the polymeric resist material produce changes in the chemical composition such as chain scission or cross linking polymerization [54]. In a positive polymer resist film, the electrons break the polymer backbone into fractions resulting in a reduced average molecular weight and an enhanced solubility of these short pieces of polymer chains in a developer [55]. This allows selective removal of exposed areas of the film.

A critical dose of electrons needed to expose a film is dependent on the radiation efficiency and molecular weight of the material, but also on the acceleration voltage and postexposure conditions, such as developer concentration and possible post baking, for example [56]. The sensitivity of the film needed in a lithography process depends on the pattern size and probe current used to expose it. The sensitivity should be such that the exposure takes place fast enough to keep the conditions both mechanically and electrically stable.

However, too high a sensitivity leads to reduced contrast, because of the exposure of the edges of the film by scattered electrons. When the electrons hit the film they overcome numerous small angle collisions. These forward scattering processes broaden the beam at the bottom of the resist layer leading to a slight under-cut structure which is a desirable feature in many cases. Those electrons which penetrate into the substrate may experience a large angle backscattering. The backscattered electrons cause the proximity effect which means that they additionally expose the areas nearby the electron beam. In addition to its radiation response, the performance of a resist material is characterised by its linewidth control, defect density and etch resistance.

The sensitivity of PMMA is quite poor and about 1 $\mu C/mm^2$ dose of exposure is needed at 20 kV, for example. The sensitivity of PMMA scales roughly with acceleration voltage, the critical dose at 40 kV is approximately twice that high [50].

### 4.1.6 Developing

The exposed pattern in the resist film has to be developed into a three dimensional relief structure having a proper profile for a successful subsequent pattern transfer. The development can take place in liquid solvent or in plasma. Plasma techniques will be discussed later in this thesis. In liquid development process the developer solvent is chosen so that it dissolves exposed cut chain molecules selectively over long polymer chains (positive resist) or that it dissolves these long chains selectively over exposed cross-linked molecules (negative resist).

Our basic double layer resist is developed in a mixture of methyl isobutyl ketone (MIBK) and isopropyl alcohol (IPA) (1:2 by volume) which dissolves the exposed top PMMA layer effectively. Then the sublayer of P(MMA-MAA) copolymer, which is exposed widely by scattered electrons, is developed in a mixture of ethylene glycol monomethyl ether and methanol (1:2 by volume). After this two stage developing the sample is rinsed by IPA and it is blown dry. The undercut obtained by this process is so large that one can prepare narrow PMMA bridges which can be used as masks in shadow angle evaporation technique for fabrication of small tunnel junctions [57].

### 4.1.7 Metallization

All thin film metallizations in this work were done using vacuum evaporation technique. In this process the material to be deposited is placed into a crucible, or if the material does not wet a metal surface, a separate crucible is not needed. After the chamber has been evacuated to $10^{-6}$ - $10^{-7}$ mbar or, in some cases, to "ultra high vacuum" (UHV) the crucible is heated by an electron beam gun to evaporate the material onto the substrate which is sitting face down at a distance of 20 - 60 cm from the crucible. The film thickness is measured by monitoring the change in resonant frequency of a vibrating quartz crystal as the material is deposited on it. The final thickness is determined by closing the shutter between the crucible and the substrate.

To achieve a clean film of a reactive material, aluminium for example, the pressure of the chamber should be such that the path of evaporated material from crucible to the substrate is shorter than the mean free path. The kinetic theory of gases gives the mean free path $< \lambda >$ for Maxwell-Boltzmann distribution of particles whose diameter is $\xi$ as a function of pressure $P$ and temperature $T$ [58]:

$$< \lambda >= \frac{k_B T}{\pi \sqrt{2} \xi^2 P}. \tag{29}$$

Typically, particles in the chamber have $\xi$ ranging from 2 to 5 Å and thus

the mean free path at room temperature is of the order of 100 m. However, great majority of particles have free path $\lambda$ between collisions shorter than the mean free path. The distribution of free paths can be calculated by equation:

$$\frac{dN}{d\lambda} = \frac{N_0}{<\lambda>}\exp\left(-\lambda/<\lambda>\right), \tag{30}$$

Where $N_0$ is the total number of particles. Under the conditions calculated above, using a typical crucible to substrate distance of 30 cm more than one particle per thousand collides with a residual gas molecule. To minimize the residual contamination the vacuum has to be as high as possible and the distance from crucible to substrate has to be short. To avoid contamination one can also increase the evaporation rate. The idea is that the outer shell of a dense beam of reactive material protects the molecules in the center of the beam gettering the residual gas molecules which are typically desorbed from the walls of the chamber.

### 4.1.8 Lift-off

The final process step is to strip the resist film and to lift-off the metal film outside of the patterned structures with it. The lift-off may be done by a plasma process or in a chemical solvent. The basic double layer resist was stripped by spraying the film by heated acetone. Thin LB films are extremely difficult to strip, due to a poor under-cut and that is why chlorobentzene was used. Sometimes ultrasonic agitation was used to assist in lift-off. Resists on fragile silicon nitride membranes were stripped using oxygen plasma etching. [59].

## 4.2 Electron beam lithography

### 4.2.1 Scanning electron microscope

The simplest EBL system is based on using a scanning electron microscope (SEM) which has been converted into a beam writer. Even though the throughput of SEM based instruments is not comparable with the large industrial EBL machines, their flexibility and low cost make them suitable for research applications. Changing the writing field and beam current and voltage is easy with an SEM based system. Yet another important property for research purposes is that an SEM conversion may be used also as a normal microscope whenever needed.

In an SEM the electrons for the beam are emitted either from a heated filament by thermionic emission over the work function potential barrier or

from a sharp conductive tip in a high enough potential for electrons to tunnel through the barrier by field emission (FE). The FE tip is typically made of tungsten and kept at room temperature. Due to their small size the FE sources have traditionally yielded the highest resolution in scanning electron microscopy. Their disadvantage for lithography is that the beam current is very noisy and unstable. The noise is due to the changes in the work function caused by adsorbed residual gas atoms on the tip surface. The atoms may also be ionized by the electron beam causing sputtering of the tip. A similar system operated with opposite voltage has been used to produce an electron free beam of positive argon ions for ion guide experiments [60].

Usually, the SEMs perform a real time correction in the display brightness to compensate for the changing beam current. However, the current that hits the sample can drift up to 10% in 10 minutes. Typical numbers may be 10 - 20% per hour [61] which makes an FE electron source unsuitable for lithographic applications. A thermal FE electron source has been developed to overcome the problems of drifting of cold FE sources. Thermal FE source extracts the electrons with a high voltage. Yet, the tip is heated to about 1800 K, which significantly improves the stability to better than 1% drift in 12 hours [61]. The imaging resolution of a thermal FE source is somewhat worse than that of a cold cathode source, but the stability makes them much better for lithography. The reason why a thermal FE SEM is not very common in lithography is that such systems cost 2 to 3 times more than a conventional thermal emitter based systems. A thermal electron source consists of a heated filament, an electrode called Wehnelt unit and an anode (Fig. 15). The emitted electrons are extracted from the electron cloud around the filament and accelerated by a positive potential of typically 0.5 - 50 kV of the anode. The Wehnelt unit which is biased negatively with respect to the cathode, bunches the electrons into a finely focused point. The filament is a hairpin shaped tungsten wire (W) or a lanthanum hexaboride ($LaB_6$) crystal. The main difference between the two is that W must be heated up to 2700 K while 1800 K is enough for thermal electron emission from $LaB_6$. The low operating temperature of $LaB_6$ is due to the low work function of the material. This makes $LaB_6$ 3 to 10 times brighter than W, thus giving higher signal to noise for imaging, which makes it easier to optimize the SEM for lithography. Low operating temperature means also longer life, because of reduced evaporation of the cathode material. However, a low price of W filaments often more than compensates for this difference. W filaments also drift less ( 1%/hr vs. 2 - 3%/hr for $LaB_6$) [61] due to less contamination at high operating temperature. The numbers given above are approximate ranges and will vary somewhat for different models and in some of the new W based SEMs the brightness is of the same magnitude as in $LaB_6$-emitters.

In an EBL system the beam of accelerated electrons emitted from the electron source is aligned with the optical axis of the system (z-axis) and demagnified to form a small electron probe exposing desired spots at the substrate. This is done by electrostatic and magnetic lenses and apertures [62] in an electron optical system which is called a column.

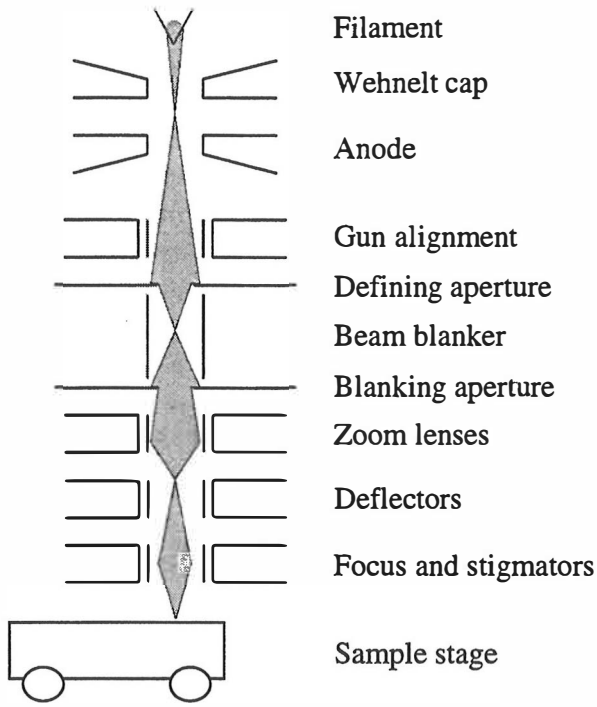


Figure 15: *A schematic drawing of an electron optical column.*

The column reduces the image of the electron source at the substrate plane (xy-plane). A cross section of a typical column structure can be seen in Fig. 15.

The size of the electron source determines the amount of demagnification needed in the column. On the other hand, a large source gives a bigger beam current than a small equally bright one, which is important especially when exposing large areas. The chromatic aberration in the lenses is dependent on the energy spread of the electrons emitted from the source. The spread is further increased by the space charge interactions between the electrons [63]. This so called Boersch effect increases when the energy of electrons is decreased. The space charging effect and the fact that the resist film has to be exposed thoroughly sets a lower limit for the acceleration voltage. An upper limit is due to the scattering of the electrons in the resist film and

from the substrate which limits the resolution roughly to the depth to which the electrons penetrate [62]. This suggests to use very low energy electrons with a very thin resist film and substrate. Another choice is to use the double layer resist. It minimizes the large angle backscattering from the substrate with a trade-off of increasing the small angle forward scattering in the bottom layer resist. Since the film layers have different developers, the top layer film can be developed with a high resolution, while scattering expands the structures in the bottom layer film. However, the suspending top layer shadows the substrate during the metallization and features of less than 100 nm can be fabricated using about 700 nm thick double layer resist (Fig. 11). To minimize both the Boersch effect and the scattering of electrons in the resist film, there exist sophisticated systems to decelerate the electrons just before the substrate. Both the spherical and the chromatic aberrations can be reduced by using weaker lenses, but this reduces also the beam current. The astigmatism is due to the residual ellipticity of apertures and imperfections in the alignment of the column [62]. Fortunately, this can be compensated by stigmator lenses added into the column. As one can see from the discussion above, the properties of the electro-optical column are compromises between the acceleration voltage, intensity and the electron probe diameter.

At the lower end of the column, deflecting coils are used to sweep the beam along the desired patterns on the substrate. Typically, a magnetic deflection is used in SEMs since the settling time is not a problem in microscopy and magnetic deflection coils introduce less aberrations than electrostatic deflection.

### 4.2.2 Beam blanker

A beam blanker prevents the exposure of the areas between the patterns and controls the dose on the areas to be exposed. In SEM it is usually an integrated part of the SEM column. A beam blanker is not absolutely necessary for lithography, but a proper exposure of high resolution patterns demands a high speed beam blanking unit. It consists of a pair of fast, usually electrostatic deflecting electrodes located at the crossover point of the beam, and an aperture. The beam is blanked by deflecting it off from the aperture hole. The response time of the beam blanker is one of the key parameters of an EBL system, because it defines the minimum step size of the beam in the exposure: the faster the beam blanker, the more dense raster of points can be used to achieve a desired dose of electrons into an area.

The beam current has to be measured by a Faraday cup and a picoammeter before the exposure. The measured beam current is then used to calculate the time to keep the beam blanker open to give a proper dose of electrons for the resist film to expose it.

### 4.2.3 Pattern generator

A pattern generator takes over the control of the scan coils and the beam blanker of SEM in order to expose a desired pattern of a resist film with a proper dose of electrons. The pattern is written as a series of point exposures. The scan coils are driven according to the pattern file by digital to analog converters (DAC). In a 1 $mm^2$ writing field two 16 bits wide DACs can point to pixels with a resolution of 1 $mm/2^{16}$=15 nm. This is close to the highest resolution of the electron beam resist materials (PMMA) as well. If the DAC is connected to an Intel microprocessor based Personal Computer (PC) through an ISA bus which has typically a speed of 100 kHz, the minimum time to point to a pixel is 10 $\mu$s. The settling time of the scan coils of the SEM to make a random displacement should be shorter than this dwell time. Then, with a typical exposure beam current of 10 pA the area dose with a continuous electron beam is 0.4 $C/cm^2$, which is roughly 2000 times the dose required for PMMA for example [50]. This means, that the beam has to be chopped by the beam blanker between the exposure points and it is on only for a period to achieve a proper dose. Another possibility to reduce the area dose is to space out the exposure points. This decreases the resolution of the lithography process and a great benefit for a pattern generator software is to allow to define a different pitch of exposure points in $x$ and $y$ directions. In some cases [64], the raster may be defined parallel to any side of the pattern allowing the critical dimensions to be exposed with the greatest number of spots. Circular shapes can be defined by polar coordinates with separate pitches for $r$ and $\Theta$.

In order to create large high resolution patterns, several small writing field exposures must be stitched together. Except the most expensive laser controlled sample stages the inaccuracy in positioning the sample stage is typically 1 $\mu$m. The positioning of the subpatterns has then to be done using predefined align marks. The alignment may be done either in the center or at the edges of the SEM writing field. The alignment is done by calculating a transformation matrix between the measured mark image and the pattern to be written. Besides stitching, the alignment feature allows multilevel patterning and processing.

### 4.2.4 Noise suppression

When choosing an adequate place for an SEM, environmental factors such as vibration, acoustic noise and elecromagnetic interference have to be taken into account. The best way to prevent floor vibration is to locate the microscope on the ground floor. If even the ground vibration level is too high, the sources have to be identified and removed. The converted SEM used in this work [65, 66] is located on a $2\times2$ $m^2$ concrete block founded directly on hard soil.

Acoustic noise can also degrade performance in producing submicron features. This is especially true with field emission sources for which the demagnification of the source, and thus demagnification of vibrations is much less than that of large $LaB_6$ and W sources. If a floor vibration isolation system is used, it may increase the sensitivity to acoustic excitation since the large mass of the instrument is no longer anchored to a large mass of the floor, but it is separated by soft springs.

To prevent electromagnetic interference, high current conductors have to be routed directly away from an SEM. Another common electromagnetic interference problem is due to ground currents. To minimize this, grounding loops of the system should be eliminated. Also digital and analog ground should be separated to prevent high frequency noise. As the magnetic field decreases with distance, the sources of stray magnetic fields, such as fluorescent lights, cathode ray tubes, ion vacuum gauges, pumps and transformers should be located as far as possible from the SEM.

In addition to the considerations above also temperature of the system should be stable, because temperature variations affect the mechanical sample stage.

## 4.3 Atomic Force Microscopy

In conventional electron beam lithography an electron sensitive resist film is exposed by a beam of electrons accelerated in an electron optical column of an SEM. Due to the high acceleration voltage the resolution of EBL is limited by the scattering of high energy (0.5 - 50 keV) electrons in the resist and the substrate. This proximity effect can be reduced by decreasing the accelerating voltage. Another possibility to expose electron sensitive polymer films is by the tunneling current in a scanning tunneling microscope (see Fig. 4). STM lithography with small accelerating voltages, down to about 10 V, has achieved lines as narrow as 20 nm [67, 68, 69]. On the other hand, since the voltages used in an STM are of the order of a few volts only, the electrons with this low energy can penetrate through only a very thin resist

film. This causes problems in deposition of a uniform film layer and in lift-off and selective etching in the subsequent pattern transfer, as will be described later in this thesis.

The exponential decay of the current as a function of the barrier thickness confines the significant electron tunneling into a very small region at the substrate. Assuming a spherical tip with a radius of curvature $R$, the radius $l$ of the spot on the substrate where tunneling probability has reduced to exp(-2)≃0.14 of that at a distance $a$ right below the tip is given by [70]:

$$l = \sqrt{\frac{2(R+a)}{\kappa} + \frac{1}{\kappa^2}} \tag{31}$$

where $\kappa$ is the decay constant given by Eq. (5). For typical values of the radius of curvature $R = 10$ nm, tip to sample distance $a = 1$ nm, and $\kappa = 20\ \mathrm{nm}^{-1}$, the spot size of the beam of electrons tunneling to the substrate is about 2 nm in diameter.

The exposure of thin resist films by low energy electrons can also be carried out by an atomic force microscope. The major advantage in using an AFM configuration rather than a tunneling based instrument is that while working with an AFM one completely separates height regulation from the exposure, a fact that greatly simplifies the operation of the instrument. This is because the surface mapping in an AFM is performed by mechanical means, and not using exposing electrons. Another benefit is that topographic viewing of the substrate area does not expose the resist as it does in EBL and STM lithography. Thus, it is possible to image the surface before, during and after the exposure.

### 4.3.1 Atomic force probe

An AFM instrument consists of a nano-Newton scale force detection and feedback system, a scanner and software, which is operating the instrument. The force probe is a sharp tip which is supported by a reflective flexible cantilever. It is usually micromechanically fabricated [71] of silicon nitride, silicon oxide or boron doped silicon which are hard materials with excellent elastic properties. The user may coat the probes by metals, such as chromium, aluminium or gold, to improve the reflectivity and conductivity.

When an AFM tip approaches a sample surface, an atomic force is acting between the lowermost atom cluster of atoms of the tip and the sample structure strictly below it [72]. The vibrational frequencies $\omega$ of atoms bound in a molecule or a crystal lattice of a solid are typically higher than $10^{13}$ Hz. Since the mass $m$ of the atoms is of the order of $10^{-25}$ kg, the spring constant between atoms is of the order of $k = m\omega^2 = 10$ N/m [72]. The spring constant

of the cantilever is typically less than that, ranging from 0.1 N/m to 10 N/m. This allows the sensor to deflect before deforming or destroying the sample surface. Also stiffer cantilevers with high resonant frequencies are used in the so-called non-contact mode, which will be described later. The deflection of the cantilever is amplified by a factor of an order of one thousand using a laser beam reflected off the back of the cantilever. The deflection of the beam is then read by a four segment photodetector and the signal is amplified and measured. The photodetector signal may also be used to generate a voltage which induces a strain into a piezoelectric crystal located below the sample (z-piezo). The strain changes the height of the sample, so that the tip to sample distance remains constant.

The sharpest tips available commercially can have a radius as small as 4 nm [73] and the area of interaction with the sample surface is only about 2 nm $\times$ 2 nm. In addition to the curvature of the radius of the end of the tip, the tip aspect ratio, in particular the angle of the side walls of a conical tip, is an important parameter. This is because the sample surface is seldom smooth but there are trenches instead. In AFM lithography the aspect ratio of the tip is even more important, due to a stronger interaction between the tip and surface. If the angle of the side walls of a tip crossing a deep and narrow trench on a sample is large, the tip cannot follow the bottom of the trench [74]. Then, the trajectory of the tip gives an impression of a very narrow and shallow groove. Even when the tip reaches the bottom of a trench with very steep walls, the AFM image shows merely the profile of the tip, not the trench. It is clear, that an AFM tip cannot reach under-cut structures of the sample.

### 4.3.2 Scanner

A modern AFM scanner design is a hollow cylinder tube electrically segmented into vertical quarters. In this work, however, a tripod scanner, similar to that of Binnig and Rohrer in their pioneering work was used. It consists of three mutually perpendicular piezo-crystal bars (x-, y- and z-piezo) glued together at one end (see Fig. 4). The sample stage is at the top of the z-piezo bar. Due to cross talk caused by nonuniform electric fields across the scanner and also due to the geometry of this design, a voltage applied to one piezo results in a slight movement of the other two dimensions, too, i.e., the three coordinates of motion are not independent. For example, when the x-bar extends or contracts, it causes rotation and extension or contraction of the y- and z-bars. This is called cross-coupling. Cross-coupling can cause SPM to generate a bowl-shaped image of a flat sample.

Another problem with a piezo scanner is that the strain of a piezoelectric

bar does not vary linearly with applied voltage. Intrinsic nonlinearity, defined as the maximum deviation from the linear strain-voltage behaviour, typically ranges from 2% to 25% in the piezoelectric materials. Piezoelectric ceramics behave also hysteretically. The difference in strain due to the hysteresis may be even 20%. To minimize errors caused by scanner hysteresis data is usually acquired only in one scan direction. Hysteresis of a z-piezo may cause erroneous step-height profiles. Further, when an abrupt change in voltage is applied, the extension or contraction of the piezoelectric material does not follow abruptly, but it occurs with two time scales: The first step takes place in less than a millisecond, the second one after a much longer time. The ratio of the second dimensional change to the first, referred to as a creep, ranges from 1% to 20%, over times ranging from 10 to 100 seconds. The creep of the z-piezo causes an SPM image to look like it has ridges on one side of a feature and shadows on the other side of a feature. When a scanner is not used for a long period of time, the deflection achieved by a given applied voltage gradually decreases, while the deflection obtained by a scanner in active use increases slowly by time. This phenomenon is called aging of a piezo crystal.

Due to these phenomena the scanner does not move linearly with an applied voltage. The measurement points are not equally spaced and an AFM image of a surface with periodic structures will show non-uniform spacings and curvature of linear structures. Usually, the nonlinear behavior of piezoelectric scanners is corrected by software, but it can never be perfect. The strategy in software correction is to compare a scanned image of a calibration grating with the known characteristics of this grating. This data gives parameters for equations to calculate the voltage to be applied to achieve a constant velocity in strain of the piezo crystals. Software correction is a simple and a cheap solution to nonlinearities of piezoelectric scanners. However, it is not good for lithography applications. The main disadvantage is that software correction compensates the scanner nonlinearities only partially. The correction is best for scans that reproduce the conditions under which the calibration was done. If the scanning area is translated, rotated, zoomed in, or the scanning speed is changed - tricks that have to be done constantly while aligning the patterns on the substrate - the correction is not accurate anymore. In practice, SPM systems that use only software corrections may deviate from true linear behavior by as much as 10%, which is far too much for reproducible patterning. Another disadvantage of software correction is that the voltages to drive the x- and y-piezos are not linear functions of position after digital to analog conversions, but rather they are complicated functions of both x and y. This complicates driving an AFM probe along a predefined path to generate lithography patterns for example.

The disadvantages mentioned above would suggest to eliminate the non-linearities by hardware instead of correcting them. This may be done by an external linear and stable sensor mounted on a piezo crystal. This kind of a sensor may be optical, capacitive or resistive. The signal from the sensor represents the true position of the scanner. It is compared to a voltage applied in order to reach the intended position. The result of this comparison is then used as feedback to adjust the position by increasing or decreasing the applied voltage.

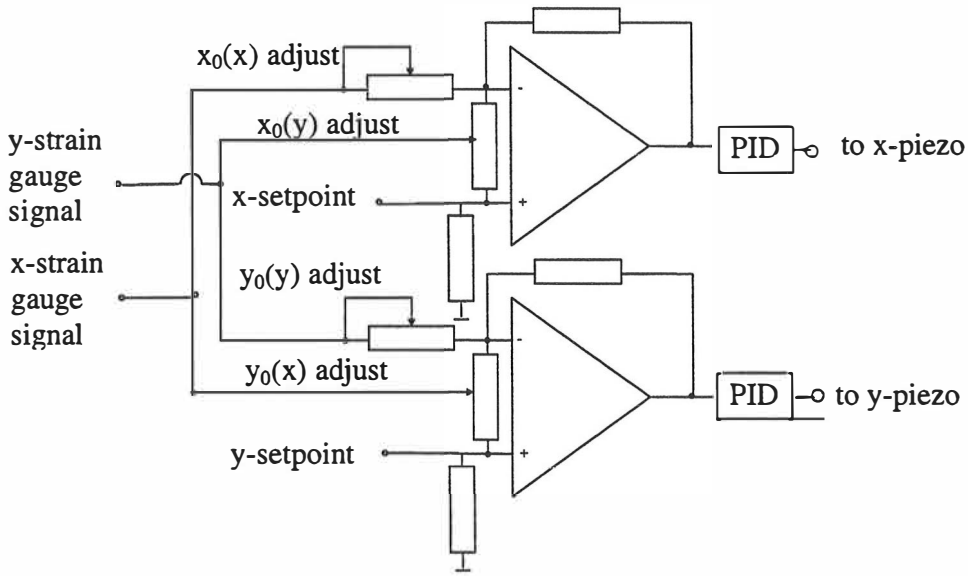


Figure 16: *Potentiometers added to the hardware for x, y and crosstalk calibration [75].*

Usually AFM systems combine both hardware and software corrections. In our original AFM instrument [76] all the piezo material artifacts had been compensated by driving the piezo voltage supplies (e.g. the high voltage amplifiers) from a feedback loop from a set of strain gauges. The strain gauges are mounted to monitor the x-, y- and z-piezo elements independently. This regulation system eliminates most nonidealities related to the piezo material, within the bandwidth limitations. The properties of the strain gauges and their installation will determine the accuracy of the scanner instead. In our instrument the strain gauges are reasonably linear but they have considerable

individual variations in gain and a remarkably large interchannel crosstalk, which needs to be calibrated and compensated. Originally this was calculated by software on the digital signal processing board (DSP) of the instrument. Then, preserving linearity in rotation and zooming in of the scanning area, each scanning angle and area needs an individual calibration file for the crosstalk and gain. We fixed this problem by including the calibration to the strain gauge hardware regulation. This was done by adding signals from each strain gauge to another, as presented in Fig. 16. These signals can be adjusted and their polarity can be changed by potentiometers $x0(y)$ and $y0(x)$ which adjust the $x$ and $y$ error signals as a function of the signals from $y$ and $x$ strain gauges, respectively. These, as well as $x$ and $y$ calibration, $x0(x)$ and $y0(y)$, can be adjusted with the help of a scan across a standard grid sample.

### 4.3.3 Vibration isolation

Due to the relatively high resonant frequency of a typical AFM probe, high frequency vibrations can disturb the instrument. If a mass is connected to a spring with resonant frequency of $\omega_0$ and damping $\gamma$, and the spring is shaken with an amplitude $A(\omega)$, the response amplitude $X(\omega)$ is given by [70]:

$$\left|\frac{X(\omega)}{A(\omega)}\right| = \sqrt{\frac{\omega_0^2 + 4\gamma\omega^2}{(\omega_0^2 - \omega^2)^2 + 4\gamma^2\omega^2}}. \tag{32}$$

When $\omega \ll \omega_0$ vibrations can pass a (rigid) spring but vibrations with $\omega \gg \omega_0$ are attenuated in a (soft) spring. Then the vibration isolation of an AFM table needs to have a low resonant frequency, $\omega_{0,table}/2\pi$, to damp effectively vibrations down to a few Hz. Lower frequencies can pass the isolation since the resonant frequency between an AFM tip and the sample, $\omega_{0,tower}$ is of the order of 10 kHz and the unwanted motion is propagating simultaneously to the tip and sample. Because AFM probes can be easily made to have a high resonant frequency, a special attention has to be paid on the stability of mechanical connection between the sample and the AFM probe. This includes glueing the tip on a plate and hanging this plate on the AFM stage.

### 4.3.4 Operating modes of an AFM

In AFM microscopy several different scanning techniques can be used [77]. Most of these operating modes have been applied for nanolithography, too.

In the contact mode the tip slides across the sample touching the surface constantly. The tip interacts with the sample by strong repulsive short range

interatomic forces, which range from 0.01 nN to 100 nN. If hard samples are scanned in contact mode, the obtained images have very high vertical resolution, since the repulsive interatomic force changes very steeply as a function of the distance between the atoms. Compression and stress as well as lateral forces such as friction and drag between the tip and a sample may lead to surface damage which limits the use of contact mode in imaging of soft samples. On the other hand, contact mode can be used in lithography to modify soft film materials mechanically. In this work, contact mode was used, while exposing very thin PMMA films by a beam of low energy electrons injected from a conductive AFM tip.

In the noncontact mode the tip is vibrated just above the surface at a constant frequency, greater than the free space resonant frequency $\omega_0 = \sqrt{k_0/m}$ (typically 100 kHz) of the cantilever, with an amplitude of 10 - 20 Å. This mechanical vibration of the tip is generated usually by a piezocrystal located below the holder of the AFM sensor. When the tip approaches the surface, weak magnetic, electrostatic and attractive van der Waals forces start to affect at a distance of 10 - 100 nm [72]. Then, the distance dependent force gradient shifts the resonant frequency of the vibrating cantilever, which can be detected as a change in amplitude. If the noncontact mode is used for lithography the film structure has to be modified by some other means than mechanically. In our case noncontact mode of AFM was used in experiments to locally oxidize thin aluminium and titanium films using anodic oxidation with an applied voltage of about 20 V between the tip and the metal.

The tapping mode can be described as noncontact mode in contact. In this mode the surface topography is recorded as in the noncontact mode, but the sensitivity is increased by lowering the tip, which is now vibrating below the resonant frequency, with a large enough amplitude to touch the sample just barely in the lower end of its swing. Vibration of the tip eliminates the shear forces which may damage soft samples and tip and this way it reduces image resolution in contact mode. The tapping tip may still be used successfully for mechanical patterning of a soft film. We have used an AFM in tapping mode to "tattoo" patterns into a non-baked PMMA film.

### 4.3.5 A pattern generator for an AFM

As a part of this thesis work a pattern generator system for lithography based on scanning force microscopes has been developed. Patterns to be transferred and miniaturized onto a chip can be scanned or drawn by any common graphical program. The pattern file is used to control a voltage at the same time as the microscope probe is scanning the surface of the substrate. The voltage can be used in numerous different ways to manipulate

the surface, depending on the lithographic method preferred. We used this system by adding a voltage to the z-piezo voltage of the scanner, in order to make the sample to jump against probe which then grooves the pattern into a film which had been spun on the sample.

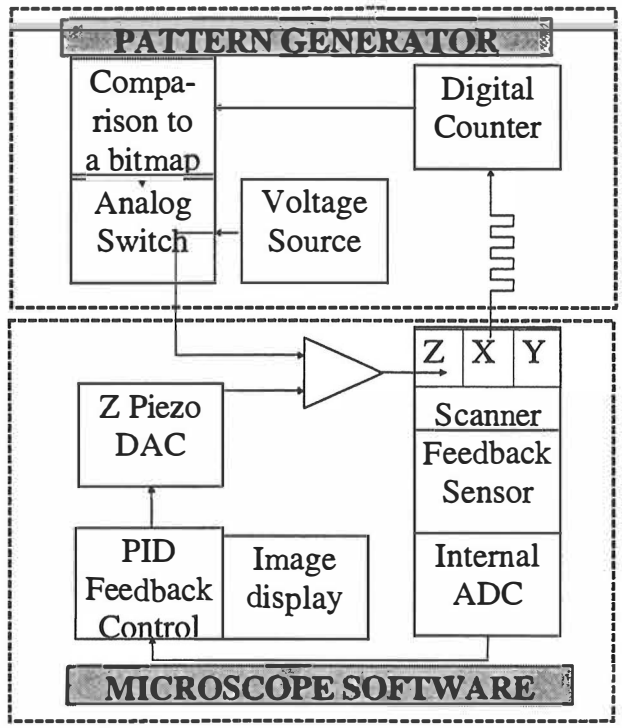


Figure 17: *A schematic presentation of the system developed in this work to control an AFM to define desired patterns on a substrate with different methods [75].*

If an AFM tip is used to manipulate a film, the shape of the tip becomes extremely important. For example, grooving a substrate by a pyramidal tip results in a quite different trace than when using a conical tip. Moreover, the resulting trace when using a pyramidal tip depends strongly on the orientation of the tip while grooving. Due to nonuniformities this may be the case with conical tips, too. That is why we wanted to preserve the orientation throughout the whole patterning. This is exactly what happens in an ordinary raster scan. In this case one does not have to drive the tip along the patterns to be grooved, but one just lets the microscope scan the sample tip in normal feedback. The pattern generator calculates the position of the probe on the substrate by trigger pulses generated after every scanned point (or pixel), using a 32-bit digital counter [78]. The position is simultaneously

compared with a corresponding point in a predrawn bitmap image of equal resolution. If the point is to be patterned the system triggers a voltage on [79]. This system is completely device independent and the voltage can be used to generate a current in electron exposure, electric field in anodization, or heat in thermal manipulation of surfaces, for example.

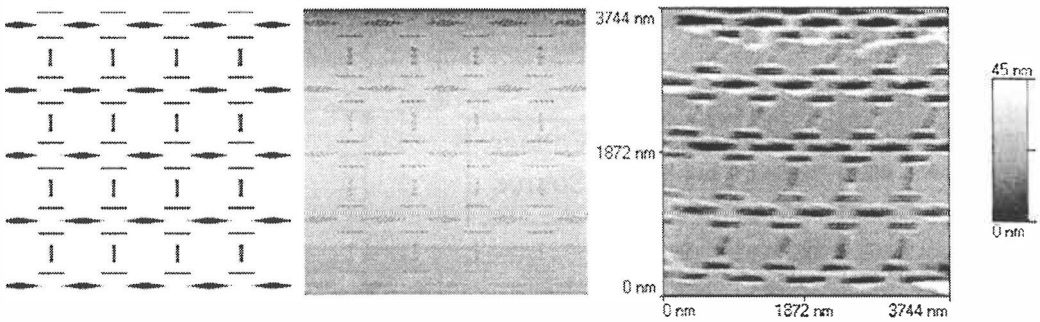


Figure 18: *A transfer of an image file into a resist film by AFM grooving. The image file to be transferred is shown on the left. The response of the AFM sensor to the voltage applied to the z-piezo to generate the pattern is shown in the middle. On the right one sees the patterned 10 nm thick PMMA film.*

This system was tested by adding the patterning voltage to the z-piezo feedback voltage. Figure 17 presents a flow chart of this set up. The instant increase in z-piezo voltage makes the sample to jump up against the sharp tip of the AFM probe, which creates the pattern into a non-baked resist film as demonstrated in [80] and [81].

Figure 18 on the left presents, as an example, a pattern that might be used to fabricate single electron tunneling arrays by shadow angle evaporation. The pattern has been drawn by Microsoft Paint program and saved as a bitmap file. The file is then used to control an additonal voltage applied to the z-piezo. The AFM software interprets this voltage as an attempt of the feedback loop to lift the sample to follow a canyon in the surface topography. That is why the pattern can be seen as black areas in the middle - this figure has been recorded during the patterning of a 10 nm thick non-baked PMMA resist film. This film was span on a 350 nm thick AZ 1350 photoresist film to protect the tip from a contact with hard silicon nitride surface of the chip. On the right one sees the result of the patterning. Figure 19 shows a vertically scanned profile of this figure. The measured linewidths of the narrowest patterns are 50 nm. The scanning area and the resolution of the AFM during the patterning should have allowed for the resolution of 30 nm.

Analyzing the profile in Fig. 19 reveals, that this is exactly the bottom width of the grooves. The measured angle of the side walls of the grooves with respect to a vertical direction is 45 $^o$. This is remarkably larger than the aspect ratio of 12 $^o$ of the tips given by the manufacturer [82]. This suggests that the edges of a groove may collapse during grooving or that the tip may be tilted a little in the transversal direction.

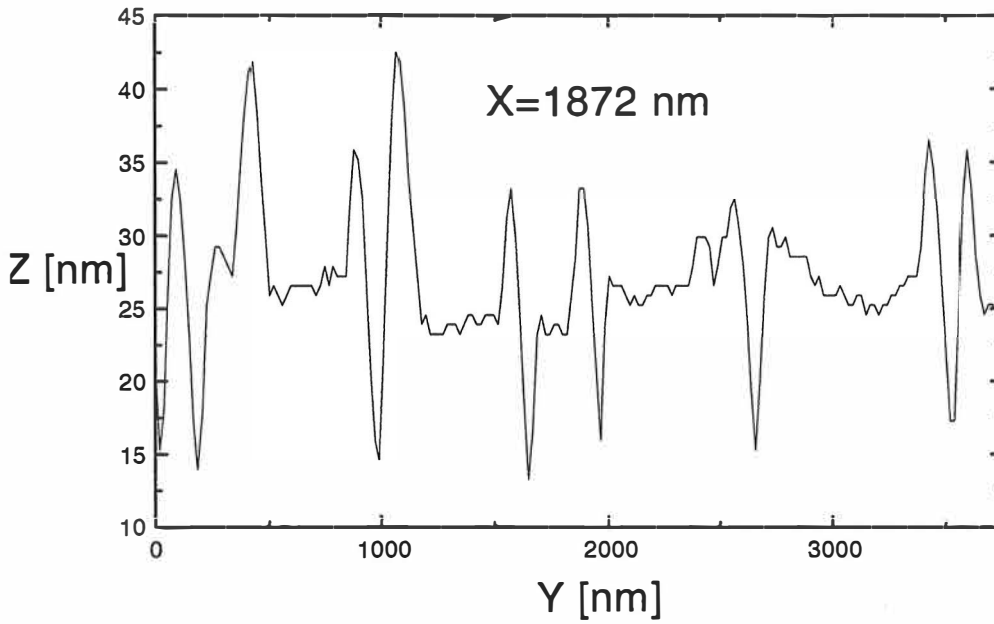


Figure 19: *A vertically scanned profile in the middle of the previous image (Fig. 18). The depth of the grooves is 10 nm. The banks around them are of resist pushed aside from the groove.*

## 4.4 Reactive ion etching

Despite of its practical easiness and almost infinite selectivity, traditional wet etching techniques are rather seldom used to transfer submicron patterns into a substrate. The main reason for that is the surface tension of the etch solution which is capable to bridge developed submicron spaces between resist films, thus preventing the etching of the underlying material. Another problem with wet etching solutions is that they may strip out the resist film and the isotropic etching profile is non-adjustable. The isotropic etching profile

depends critically on the exact etching time because overetching results in widening of lateral dimensions of the etching pattern. In addition, problems in reproducibility of the wet etching process rise with difficulties in controlling exactly the etching temperature and the etching solution concentration. From the industry point of view, the wet etching technique in semiconductor device production demands large amounts of harsh chemicals and thus it fits poorly with the other processes in line. This means increased expenses, and more sources of contamination and industrial wastes. To overcome these problems plasma enhanced dry etching processes have been adopted in submicron device fabrication. Anisotropic etching profiles, possible by dry etching [83], are of use in the fabrication of capacitors in deep trenches instead of on the wafer surface, for example. This takes an advantage of the third dimension and greatly increases the packing density [84]. However, wet etching is still the process in bulk micromachining since it has a superior selectivity combined with high etching rate.

This thesis concentrates mainly on Reactive ion etching (RIE). According to its name RIE combines reactive chemical and physical ion etching. The etching profile is greatly dependent on the ratio of these two. A purely chemical etching leads usually to an isotropic etching profile (in an isotropic substrate) while etching by physical ion bombardment progresses in an anisotropic front. Combining these two, i.e., sputtering the target by ions of a chemically reactive material, gives an etching profile in between. The shape of the profile can be adjusted by tuning the pressure or the accelerating voltage, for example. Roughly speaking high pressure and low voltage yield an isotropic etching profile, while low pressure and high voltage lead to a vertical etching profile.

### 4.4.1 Glow discharge technique

A plasma is a partially ionized gas containing electrons, ions and neutral atoms.

In DC excited plasma a constant electric field is applied between two electrodes. Some of electrons moving in this field towards the anode gain a sufficient amount of energy to be able to ionize a gas molecule at a collision. Positive ions produced are accelerated into the cathode. They also collide with gas molecules resulting in an avalanche multiplication. The cathode is sputtered by the positive ions.

In DC sputter etching the substrate has to be conductive. Otherwise it will charge up by the ions hitting it. This problem can be avoided using a radio frequency (RF) glow discharge technique. In this technique the plasma is created by a radio frequency RF electric field applied to one side of a par-

allel plate electrode system located in the etching chamber (see Fig. 20). The other electrode is grounded together with the chamber walls. A typical pressure of the chamber ranges from $10^{-4}$ mbar to 10 mbar. The discharge is initiated by electrons generated by field emission. When the electrons have gained a sufficient amount of energy from the RF field they collide inelastically with the gas molecules causing ionisation and dissociation. Ionisation leads to a cascade of reactions through the gas volume. Current flows in plasma by both electrons and ions of nearly equal concentration. Due to a higher mobility of electrons accelerated in the field, they can reach the electrodes and the walls of the plasma chamber more easily than ions. A blocking capacitor connected between the RF source and the electrode prevents any DC to flow. This builds up a negative charge on the walls and electrodes, which repels electrons and attracts positive ions. When the steady state situation is established the fluxes of electrons and positive ions striking the surfaces are equal and the glowing part of the discharge is the most positive potential in the system [85].

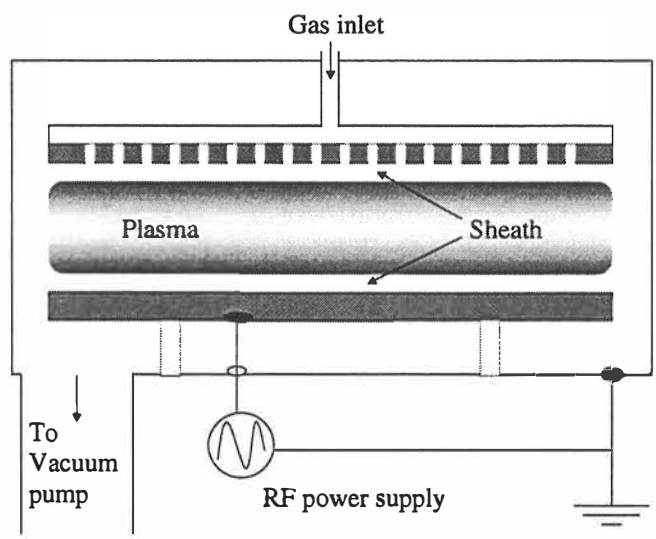


Figure 20: *The principle of a reactive ion etching apparatus used for sample fabrication.*

A depleted space called a sheath forms between the plasma and the chamber walls and electrodes. The central plasma is quite a good conductor since there are numerous charged particles and a positive potential is uniformly spaced over it. The potential drops through the sheath by a few hundred

volts over a distance of less than 1 cm. Since the grounded area is larger than the RF powered electrode the potential drop and the energy of the ions hitting the powered electrode are higher than of those hitting the grounded surfaces. If the area of the electrode connected to the RF source and the area of the grounded surface are $A_{DC}$ and $A_G$ respectively, the ratio of the voltage drops $V_{DC}$ and $V_G$ at these electrodes is given by [59]

$$\frac{V_{DC}}{V_G} = \left(\frac{A_G}{A_{RF}}\right)^n, \tag{33}$$

where the experimental value of $n$ ranges between 1 and 2. The calculated value of $n$ is 4 which is obtained by assuming the space charge limited current flow and approximating the sheath regions as capacitors. The bigger is the ratio of the electrode areas the larger is the ratio of the voltage drops at the electrodes. If the substrate is located on the grounded surface, it experiences a bombardment by low energy ions only. This is called plasma etching. If the substrate is positioned on the RF powered electrode and the pressure in the chamber drops well below 0.1 mbar the ion etching contribution becomes significant and the term RIE is justified.

A typical concentration of electrons in the plasma chamber ranges from $10^9$ cm$^{-3}$ to $10^{12}$ cm$^{-3}$ [84] being only about 0.01% of that of neutral species. The average energy of the electrons is a few electron volts which corresponds to a ten times higher temperature than the temperature of the gas, which is typically less than 1000 K.

Under these conditions the energetic electrons are striking the reaction gas molecules causing dissociation to form free radicals, ions and excitations. Free radicals are neutral atoms or a group of neutral atoms with incomplete bonding. They are not accelerated in the electric field since they are electrically neutral, but they are diffused to the target from random directions. Chemically highly reactive free radicals are normally achievable only at very high temperatures. Because the plasma temperature remains only slightly above the room temperature, the films do not have to stand high temperatures.

The motion of the ions is random in the central part of the glow, but when a positive ion reaches the sheath boundary, the electric field accelerates it towards the closest electrode. In reactive ion etching, the energetic radiation of ions is not responsible for chemical reactions but it results in surface damages which provide more sites for chemical reactions [86]. The ion bombardment also improves the desorption of the reaction products.

### 4.4.2 Etching rate and selectivity

The goal of dry etch process is usually to obtain a high etching rate over that of the masking film with a specified profile. The chemical etching rate is exponentially dependent on the ratio $E_a/k_BT$, where $E_a$ is the activation energy of the chemical process, which depends on the process gas and on the processed material. Thus, the selectivity, which is defined as a ratio of the etching rates of the masking film and the substrate, depends on the difference between their activation energies and is a highly sensitive function of temperature. In RIE, however, the etching rate and selectivity are not dependent on temperature but they are rather determined by the flux and energy of the ions. In some processes these parameters have a threshold value below which the etching rate is zero [87]. The energy and the flux of ions hitting the substrate are dependent on the power and frequency of the RF excitation, the potential of the electrodes and the chamber geometry. This makes it possible to vary or even reverse the selectivity by tuning the properties of the plasma.

### 4.4.3 The loading effect

The etching process consumes the active species created in the chamber. This results in the so called loading effect. Due to the loading effect the etching rate is affected by the area $A$ of the surface being etched. Assuming a linear reaction rate with a constant $k$, then, if the reactant species are produced by plasma with a rate $G$ per unit volume and unit time, and they recombine with a rate $\tau$, the etching rate $R$ may be written as [88]

$$R = \frac{G}{n}\left[\frac{\tau k}{1 + (\tau k A/V)}\right], \tag{34}$$

where $V$ is the volume of plasma and $n$ is the number of atoms in unit volume of the layer to be etched. The etching rate decreases when A increases. Experimental results on silicon nitride $Si_3N_4$ in a $CF_4$ plasma show reduced etching rate already when $A > 1000$ nm$^2$ [89].

The loading effect may result in a strong increase of the etching rate when $A$ rapidly falls down as the etched film clears out. This causes problems, when trying to increase a resistance of a metal film by etching it thinner. To avoid this the loading of the chamber, i.e., the area to be etched should be minimized while the plasma volume should be maximized. On the other hand, the etching rate may also decrease due to the loading effect. This is the case in isotropic etching when $A$ increases during the process. If the conditions are adjusted so that the etching rate falls down at a specified depth, the loading effect promotes the reproducibility of the process.

### 4.4.4 Etching profile

Although one of the most celebrated features of dry-etch processing is its capability to create anisotropic etching profiles, there are applications where isotropic etching is needed. For example different cleaning and passivation processes with vertical structures or under-cut structures for lift-off lithography on a substrate take advantage of isotropic etching. Another application of isotropic RIE will be introduced in chapter 7.

Isotropic etching profiles are obtained when the chemical reaction dominates and the energy of the ions hitting the substrate is as small as possible. This situation is best achieved using plasma etching and locating the substrate downstream from the plasma zone generating the reactive species. However, RIE with a relatively high pressure moderates the energy of ions and isotropic etching profiles can be obtained.

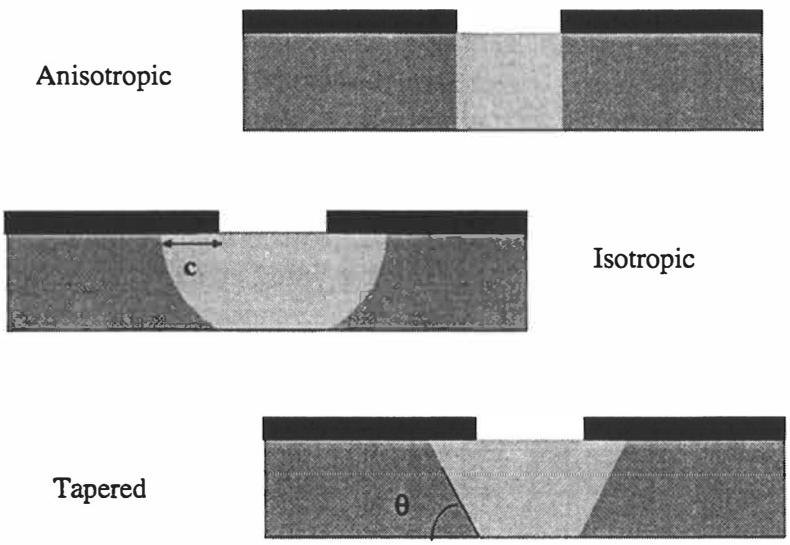


Figure 21: *Isotropic, anisotropic and tapered etching profiles. The amount of under-cut, c, and taper angle, $\theta$, are also indicated.*

When the pressure of RIE is decreased and the energy of the accelerated ions is increased, a more anisotropic etching profile is obtained. The accelerated ions hitting the substrate break the bonds at the surface making it chemically more reactive and also stimulate desorption of reaction products exposing a fresh surface for reactive species. This results in an enhanced etching rate in the direction of the accelerating field and hence, to an anisotropic profile. When pressure increases collisions in the sheath randomize ion ve-

locities. Also temperature spreads out the angular distribution of ions [87]. Tuning plasma parameters and the composition of the process gas, different profiles can be achieved.

### 4.4.5 Etching silicon nitride

Fluorocarbons are often used as etchant gases for silicon and silicate glasses [59]. In this work all etching of silicon nitride was done using Tetrafluoromethane ($CF_4$) etching gas.

Energetic electrons in plasma break bonds in $CF_4$ forming trifluoromethane ($CF_3$) and fluorine:

$$e^- + CF_4 \rightleftharpoons CF_3 + F + e^-. \tag{35}$$

The free radicals are much more numerous in a glow discharge since they are produced at a lower threshold energy (< 8 eV) and they have longer lifetimes than ions. The relative fluxes of free radicals and ions are, however, about equal since the ions move much faster than radicals due to the energy gained from the sheath electric field.

The fluorine free radicals react with silicon nitride, $Si_3N_4$ as:

$$12F + Si_3N_4 \rightarrow 3SiF_4 + 2N_2. \tag{36}$$

The reaction product, $SiF_4$, (tetrafluorosilane) has high vapor pressure and thus, it is well desorbing and it can be easily pumped out of the chamber. Trifluoromethane does not actively etch the nitride, but it may increase selectivity over silicon participating in the polymer film deposition which passivates the silicon surface [90]. The amount of fluorine atoms in the plasma can be dramatically increased by adding oxygen into the etching chamber. This is due to oxygen reactions with $CF_X$ radicals forming CO, $CO_2$, $COF_2$ and F [37]. Moreover, the consumption of $CF_X$ leads to the suppression of $C_XF_{2X}$ polymer formation on surfaces. This polymerization may even stop etching. If too much oxygen is added (>15%), etching rate starts to decrease due to the dilution of the etching gas.

RIE etching rate for silicon nitride is of the order of 100 nm/min being about the same as that for silicon oxide (60 - 100 nm/min) [91] and slightly lower than that for silicon 300 nm/min [92]. The rate does not show noticeable dependence on temperature [91] but it is sensitive to the electrode potential [93]. These things together with the small loading effect [94] emphasize the importance of ion bombardment in the process.

Organic resist masks used for pattern transfer must withstand the reactive species, ion bombardment and photon radiation produced in the plasma. The selectivity of RIE is relatively low: a typical value for silicon nitride

over AZ 1350 photoresist in the $CF_4$(96%):$O_2$(4%) plasma is 3 [95]. The etching of the masking polymer films is dominated by reaction with oxygen, but the process is enhanced by fluorine atoms, which remove hydrogen from the polymer making it more reactive with oxygen [96, 97]. Pure oxygen plasmas can be used to selectively strip the resist films from substrates or even to transfer patterns into a mask [36]. In mask fabrication the properties of plasma can be tuned to stress the chemical reactions (isotropic) or ion bombardment (anisotropic) in order to achieve desired mask profiles. These include under-cut for lift-off lithography, for example. If the plasma does not contain oxygen, it may even stabilize the polymer film [98]. Ultraviolet radiation in the plasma enhances the chemical activity and thus reduces the selectivity of an organic resist film. This is due to the scission of polymer chains similar to what happens to long PMMA chains in EBL as described earlier.

### 4.4.6 The reactive ion etcher

All reactive ion etching experiments described in this thesis were carried out in Axic Benchmark [99] RIE machine (see Fig. 20). This system has two water cooled parallel stainless steel electrodes 18 cm in diameter. The distance between the electrodes is adjustable up to a few centimeters. The process gases are fed into the etching chamber through the upper electrode with a shower head shape. This electrode is grounded together with the chamber walls. The lower electrode is connected to the RF power source operating at the standard industrial frequency of 13.56 MHz via an inductive-capacitive matching network operated to achieve the best power transfer to the plasma. The etching chamber is pumped down by a molecular drag pump. After maintaining a desired flow of process gases by automatic mass flow controllers, the chamber pressure is manually set by throttling the pumping line. The pressure is measured by a capacitive pressure gauge, which does not need a calibration for different process gases used. Also the gas flow rate, etching time, forwarded and reflected power and the voltage difference between the electrodes (DC bias) can be monitored during the process.

The chamber walls and electrodes were always cleaned prior to etching by rubbing the surfaces with a tissue paper using acetone as a cleaning agent. The cleaning was completed using a pure oxygen (occasionally argon) plasma for 5 min to remove any residual contamination.

This is because the process gases, such as $CF_4$, form byproducts, which coat the interior of the etching chamber. If these materials are not removed frequently from the chamber, they will redeposit onto the substrate. This will, of course, reduce the etching rate or, in the worst case, extinguish

the etching completely. The contamination will reduce the value of the RF induced DC bias, which is thus a good indicator of the cleanliness of the chamber. Another indicator for chamber contamination is the minimum achievable pressure. If the chamber pressure does not reach its typical value of less than $1.3 \cdot 10^{-3}$ mbar (1 mtorr) in a reasonable time, and there is no leak in the vacuum system, the residual pressure may be due to contamination. This can be tested by cleaning the chamber and observing the pressure while pumping down again.

# 5 Experimental setup for testing fabricated structures

An initial test for fabricated structures was to measure their resistance at room temperature. A "good" sample with tunnel junctions should have a resistance of a few kilo-ohms for each junction. If the resistance is higher than that, the tunnel barrier is too thick, while too low a resistance indicates a shorted junction. Moreover, the resistance of nanoscale devices may not be very stable immediately after metal deposition, but it tends to increase due to annealing and relaxing of the deposited material. Usually, this drift slows down in a few days and if the devices are still usable they remain relatively stable.

Low temperature measurements were carried out at liquid helium temperature using a dip stick or at lower temperatures using a dilution refrigerator [100], which is able to cool samples down to about 50 mK at its best. Temperature was measured by a carbon resistor calibrated against a primary Coulomb blockade thermometer (CBT) [11]. Temperature was regulated by throttling the $^3$He circulation.

Current-voltage curves were measured applying a DC voltage from a home made sweep and using room temperature current and voltage preamplifiers [101] and a digital voltmeter [102] to read the signals. Dynamic conductance curves were measured by detecting the response of the sample to a small AC excitation current added to the bias. This was accomplished using standard lock-in techniques [103, 104]. Also heat capacity measurements for titanium disks on a thermally isolated silicon nitride membrane were carried out using a lock-in amplifier [103, 104].

To minimize external interference the whole setup including the electronics and the refrigerating system was placed into an electrically shielded room [105]. The measured data were brought out from the room using a general purpose interface bus (GPIB) with an optical isolation [106] and read by a personal computer.

Due to the small size of the nanoscale devices, they are extremely sensitive for any static charge and voltages. A tiny voltage spike may break thin metallic lines in these devices. Most often junctions are shorted due to damage in the tunnel barrier. For this reason, everything that will be in touch with nanodevices has to be well grounded. In addition one has to take care of noisy switches, pick-up voltages in moving cables etc.

# 6 Fabrication by atomic force microscopy

Although the line width of the conventional electron beam lithography (EBL) can be, in some cases, squeezed to below 10 nm [107], a number of alternative methods are under investigation. One possibility is to transfer single particles on a substrate using an AFM or a scanning tunneling microscope tip [108, 109]. The particles can then be positioned to form desired patterns.

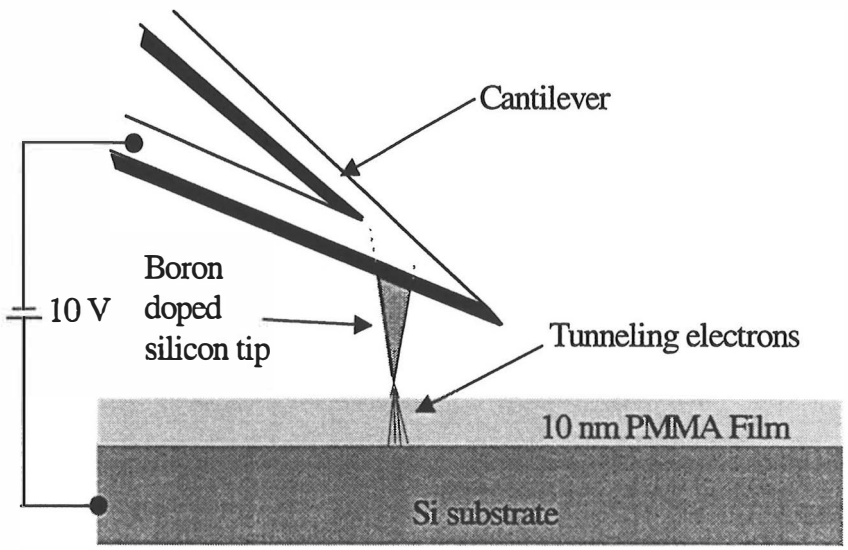


Figure 22: *A principle of exposing a thin PMMA film by electrons injected from an AFM tip.*

Another possibility is to oxidize patterns on the hydrogen passivated surface of the substrate by applying an electric field between the substrate and the STM [110, 111] or the AFM [112] tip. Further, the field can also be used for a very local anodic oxidation to manipulate electrical properties of a thin metal film deposited on a substrate. This anodization may take place in an electrolyte [113] or in humid ambient air [114].

The microscope tips can also be used to draw patterns on a resist film on the substrate. Different resist materials can be exposed by heat [115, 116], by mechanical scratching [81, 80] or by electron beam generated by a tip [117], in analogy to conventional EBL. Our experiments in electron exposure using an AFM will be described below.

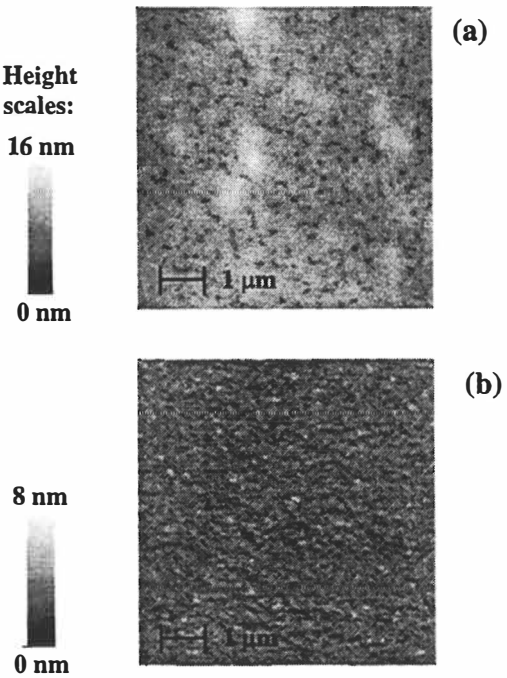


Figure 23: *A spin-cast film (a) and an LB-film (b) of the same thickness of 10 nm in both cases. The spin-coated resist film is less uniform and it contains numerous point defects on its surface.*

## 6.1 Electron exposure using an AFM

We used a conducting AFM tip to expose very thin PMMA films. An exposing current of low energy electrons was induced from the tip to the substrate by applying a small bias voltage between them. The principle is presented schematically in Fig. 22. This technique using traditional polymer resists, e.g., PMMA and SAL601, has been used in Refs. [118] and [119], respectively.

Extremely thin films are needed, to allow tunneling of the low-energy electrons produced by the AFM. Such a thin film, spin-coated at a high speed using very dilute solutions, is not uniform and shows a high density of point defects as can be seen in Fig. 23(a). Therefore, we have adopted the Langmuir-Blodgett technique for polymer deposition as described in [47]. A uniform 10 nm PMMA resist film, fabricated using this method can be seen in Fig. 23(b).

To be able to apply a bias voltage between an AFM tip and substrate, they both have to be made of conducting material. This requirement rules

out glass as a substrate material, and also excludes the use of oxidized and nitridized silicon wafers. This is why we ended up using standard (525±25) $\mu$m thick boron doped silicon wafers whose resistivity was 5 - 10 $\Omega$cm [120].

For electrical measurement of the fabricated structures, larger scale bonding pads were introduced on the substrate by conventional EBL prior to AFM lithography. Further, to stitch the fine structures with these bonding pads, a special alignment pattern was introduced in the same EBL process. This "navigation" structure consists of an array of squares. Each square is identified by a small dot whose location inside the square reflects the position of the square in the array, i.e., the dots are positioned with a slightly smaller pitch than the squares. Each square of the pattern reveals the direction and distance to the central area, which is wired to contact pads.

The alignment structure was metallized by vacuum evaporation. First a 15 nm thick chromium layer was evaporated to improve the adherence to the silicon surface. This layer was followed by a 20 nm thick gold layer to provide a clean and non-oxidizing surface. The gold layer was evaporated at a continuously varying angle in order to make the edges smooth. In practise this was done by tilting the sample table 10 degrees with respect to the line sight from the source and rotating the sample table about its normal.

We used RIE to remove organic residues and roughen the surface of the substrate prior to the subsequent LB film deposition. This was essential in order to obtain a uniform and well covering film. The process took place in 0.040 mbar (30 mtorr ) argon plasma at the power density of 2.5 W/cm$^2$. The optimum etching time for these parameters is 5 min. With longer etching times the alignment structures were damaged and the surface roughness of the subsequent LB film increased also.

A thin resist film was then LB deposited on the substrates and metallic alignment structures. For the film deposition we used a commercial KSV "Minitrough" Langmuir-Blodgett facility [121], operated in a laminar flow clean air environment. We spread 940 000 u (molecular weight) PMMA as a 500 ppm solution in chlorobenzene onto a pure water sub-phase. A constant surface pressure of 13 mN/m - well below the first collapse point of the film layer - was set and maintained throughout the process. Thus, the thickness of the film on the water is, in principle, the thickness of one "monolayer" of the material. The deposition was started with an up-stroke from the water sub-phase followed by eight dipping cycles, giving a total of 17 monolayers.

After the deposition the films were baked at 160 °C. Already 5 minutes gave satisfactory results, with such a small film thickness. Higher baking temperatures caused extra difficulties in the lift-off process, while lower temperatures left the film too soft thereby reducing the selectivity of the subsequent development.

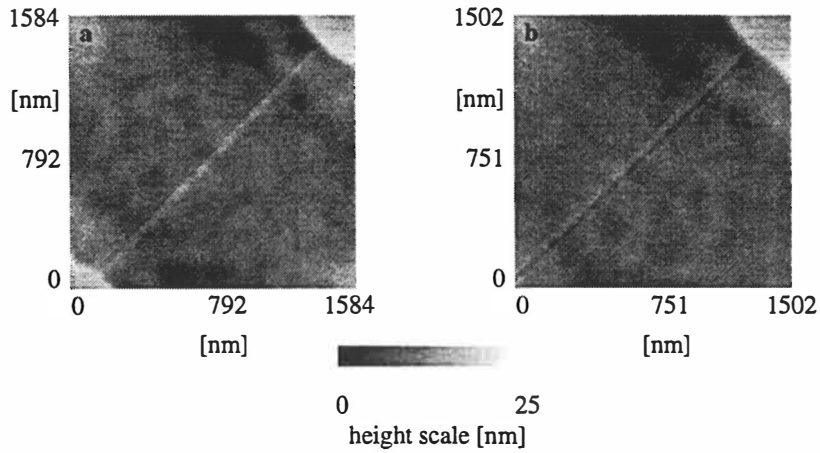


Figure 24: *Exposure of an 11 nm thick PMMA LB-film immeadiately after the exposure and after development in pure isopropanol for 10 s. In (a) a slight increase in thickness of the exposed film indicates a change in film structure. In (b) the developer has dissolved the exposed material, over a 20 nm wide open line [122].*

An unexpected problem was a partial tearing-off of the first layer during the first down stroke until we realized that a baked (160 °C, 1 min) first layer could withstand the subsequent dippings. After the first cycle, there were no problems with the following layers. Sometimes the contact and alignment relief on the substrate caused a slight waviness on the resist surface, but fortunately, without any practical influence on the lithography.

The lines defined by AFM lithography were drawn to connect a 3 $\mu$m wide gap in the center of the alignment structure. As an electron injector, we prefer doped silicon tips [82] to traditional silicon nitride AFM probes. This is because doped silicon is conducting enough to facilitate lithography without metal covering. Metal deposition bends the cantilevers which gives rise to difficulties in aligning the laser based force readout system. Also electrical properties of a deposited thin metal film on such a sharp tip are very unstable. Using metal coated standard tips the voltage required to expose a film on a substrate varied considerably from tip to tip, probably since deposition, aging and erosion of the coating results in different tip radii. The doped silicon tips provided less variation. Voltages used typically ranged from 18 to 20 V.

In our experiments we operated the AFM in the ordinary contact frame scan mode, and simple line patterns were generated by switching the exposure voltage on and off. We could repeatedly establish the fact that there exists a range in the exposure voltage, in which the resist is not mechanically affected by the exposure, but it can be developed into the desired pattern using a weak solvent. Figure 24 presents a 20 nm wide line after the exposure (a) and after the development (b) of the film in pure isopropanol for 10 s. A slight increase in the thickness of the exposed film indicates a change in film structure. If the line was patterned by a mechanical contact between the tip and the film, the thickness of the film would rather decrease than increase. Further, the development in isopropanol dissolves only the line area of the film, a fact that clearly suggests changes in film structure due to tunneling electrons.

Unfortunately, we did not succeed in pattern transfer with the narrowest lines. A fairly thin (60 - 70 Å ) metal film was evaporated on samples with different line widths. The lift-off was performed using acetone and occasionally chlorobenzene. Aluminium gave the best results of tested metals with minimum widths of around 50 nm of conducting lines. Evidently forward scattering of electrons in the resist creates a slightly under-cut structure, making thereby the lift-off process possible.

In addition to the problems in lift-off it is extremely difficult to fabricate tunnel junctions while using very thin resist films. The traditional method to form a tunnel barrier between two electrodes using a shadow angle evaporation is useless; for this a thick double layer resist is needed. Another possibility is to form an oxide barrier directly on the pre-defined bottom electrodes by thermal oxidation either in air or in pure oxygen. However, metals that can be oxidized, develop too thick an oxide layer as a result of the repeated dipping into water during the LB deposition. We regarded pure chromium as the most promising candidate due to its slow oxidation in air, but still with the possibility to grow a good oxide barrier. This has been demonstrated in experiments on Cr based EBL fabricated junctions [123]. Evidently, even the chromium develops too thick an oxide in water, because despite of many attempts, we never saw any conduction between two chromium bottom electrodes connected with a top electrode introduced after a LB deposition. It may also happen that chromium gets covered by contamination forming this way a thick barrier.

Next we tried to create artificial $Al_2O_3$ barriers onto supposedly non-oxidizing gold bottom electrodes. After the development of a line exposed by AFM, a thin layer of aluminium was evaporated on the substrate and the film was oxidized completely through. The actual top aluminium electrode was evaporated on that layer. The thickness of the first layer is extremely crucial. Too thin a layer contains numerous pinholes, while too thick a layer

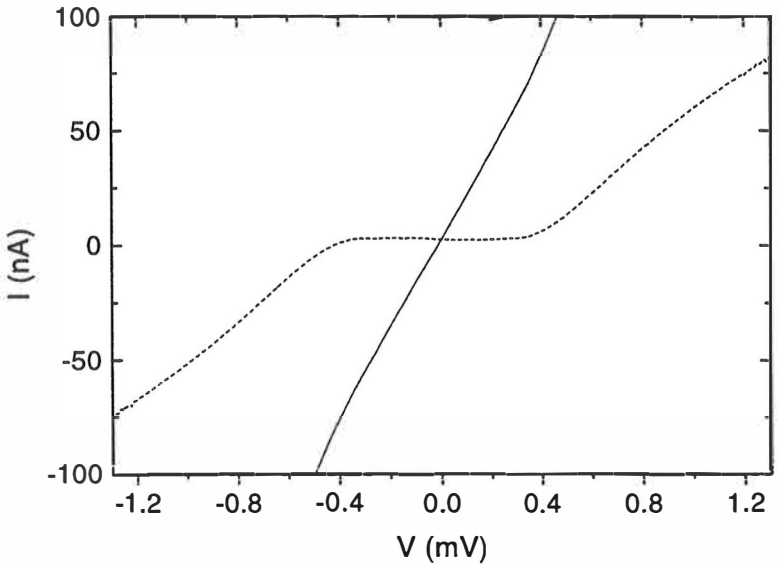


Figure 25: *Electrical measurements at 100 mK of a sample with two series connected junctions with artificial $Al_2O_3$ barrier between gold and aluminium electrodes. The measured solid IV curve shows a significant shunting, the linear slope of which has been subtracted in the dashed curve.*

is impossible to oxidize through. In both cases the tunnel junctions will be shunted. The experiments resulted in a few successful junctions. Their room temperature resistance ranged from 1 to 100 k$\Omega$. The samples were cooled down and their IV and differential conductance versus voltage curves were measured at different temperatures down to below 100 mK. The solid IV curve in Fig. 25 has been measured of a fabricated sample at 100 mK. The structure shows a clear superconducting gap due to tunneling through two NIS junctions. However, the sub-gap conductance is relatively high indicating a considerable shunting either through point defects or a conducting first aluminium layer. The assumedly linear contribution of this shunting of 5.2 k$\Omega$ has been subtracted in the dashed curve.

## 6.2 Anodic oxidation using an AFM

We constructed a system to locally oxidize metallic surfaces using an atomic force microscope (AFM) [113, 114, 124]. This process is similar to electrochemical anodization, but now a conductive AFM tip works as a cathode

and an electrolyte is replaced by the ambient humidity of air.

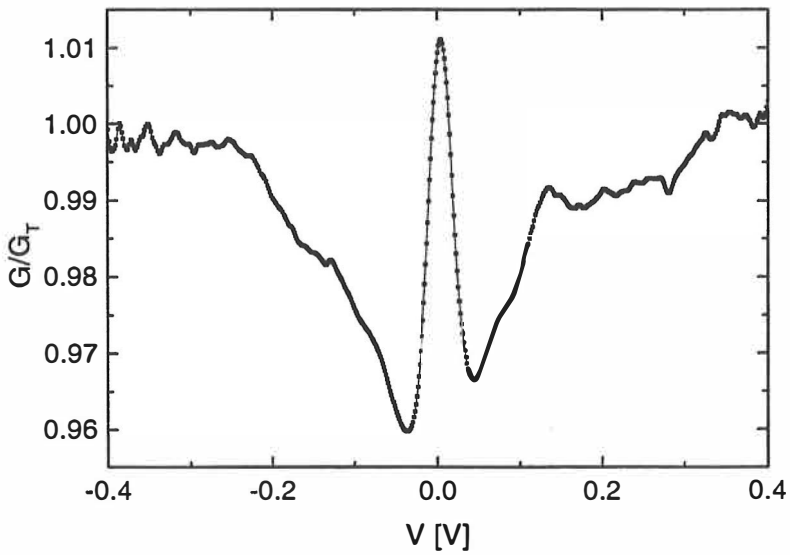


Figure 26: *A strongly non-linear behavior of an oxidized aluminium strip measured at liquid helium temperature. A conductance drop normalized by the corresponding asymptotic, high voltage value at small bias voltages resembles that of an array of tunnel junctions. However, there is a sharp peak with enhanced conductance at bias voltages close to zero.*

In this setup a negative bias voltage is applied to a metal strip to be oxidized, with the conducting AFM tip grounded. When the metal film is then scanned in contact mode in ambient humidity of air, a strictly local surface anodic oxidation occurs. The resistance through the sample can be monitored and used as a feedback to control the anodization voltage. When a predefined resistance value is achieved the voltage can be set to zero. The voltage can also be selectively switched on and off during a scan to produce electrical structures - point contacts, quantum wires or tunnel junctions for example.

The system has been tested by oxidizing 0.5 $\mu$m wide and 10 nm thick aluminium strips with a continuous voltage of roughly 10 V. These aluminium strips were connected to larger scale contact pads fabricated simultaneously with the strips by EBL. A threshold electric field for anodization is roughly $10^9$ V/m [59] and thus the voltage used is enough to oxidize the metal just through the thickness of the film.

The resistance of the strips doubled from its original value in about 20 minutes. The sample resistance is very unstable during and right after the anodization. Apparently, when the anodization voltage has been turned off, further oxidation occurs and an additional time is needed for sample to stabilize. After stabilization strongly non-linear current-voltage characteristics were measured for these samples at 4.2 K (see Fig. 26).

# 7 Fabrication of vertical tunnel junctions through a thin silicon nitride membrane

A method to use thin silicon nitride membranes for nanolithography to fabricate very small vertical tunnel junctions [125] was further investigated in this work. The technique is closely related to that used in fabrication of point contacts in Refs. [126] and [127]. A tiny etched aperture in a membrane forms a mask for metal deposition. Because the thickness of the evaporated metal film can be controlled very accurately, the method allows fabrication of chains of junctions with extremely small and thin isolated aluminium islands in between. The single junctions showed low environmental impedance. For the double junction structures we measured similar suppressed energy gap threshold voltages as earlier [125], which might indicate that the islands are not superconducting. However, supercurrent through the samples suggests that the island is in the superconducting state as well.

The substrate material for the membranes was double polished (100) oriented silicon wafer having about 300 nm thick silicon nitride on its both sides. Also this LPCVD silicon nitride layer was grown at the University of California.

The silicon nitride membranes were fabricated by anisotropic wet etching of silicon in potassium hydroxide (KOH). Silicon nitride on one side (which will be referred to from now on as the back side) is used to define a mask window for the etching of the intermediate silicon to expose a square silicon nitride membrane on the opposite side (the front side) of the chip. The mask window was defined using photolithography and it was opened by reactive ion etching.

Due to a great selectivity of {100} and {110} over {111} planes in wet etching of silicon, four {111} sidewall planes are gradually formed as the <100> front progresses anisotropically downward with time until only the silicon nitride and {111} planes are remaining. The sidewalls intersect the surface at $54.74^{o} = \arctan(\sqrt{2})$ angle, and thus the etched cavity will always have a bigger opening on the top than on the bottom, and if the side of a square masking window is smaller than $\sqrt{2}$ times the thickness of the (100) silicon, the etching will result in a pyramidal cavity unless extremely long etching times are used.

Under these conditions, the size of the etching mask window has to be scaled up by $\sqrt{2}$ times the thickness of the (100) silicon wafer. In addition, the sides of the mask have to be carefully aligned with <110> direction of the wafer. Misaligned window will result in too large membranes, since {111} planes will encompass the window. Our photoresist mask was designed to

have a 3 × 3 matrix of 800× 800 $\mu m^2$ squares with 1.5 mm pitch. A chromium mask was fabricated using EBL and wet etching. The mask was aligned [128] in the center of a 1 $cm^2$ square chip cleaved along the <110> direction. A photoresist layer was deposited on both sides of the chip. The back side film was made to protect the membrane layer during the following processing steps.

This photolithography pattern was transferred into the silicon nitride by reactive ion etching in 0.013 mbar (10 mtorr ) $CF_4$:$O_2$ (3:1 by volume) plasma using RF power of 1.5 W/$cm^2$. A typical dry etching time for a 300 nm thick silicon nitride layer was 1 minute.

The subsequent wet etching took place in a KOH:$H_2O$ (1:4 by weight) solution at 98 $^oC$. The etching time for 500 $\mu m$ silicon layer was 3.5 hours. To stop the etching completely by removing any possible KOH residues from the membranes, the chips were boiled in de-ionized water immediately after etching. The result was nine equally spaced 100 × 100 $\mu m^2$ square membranes.

The idea was to use the fabricated insulating membranes as a mechanical mask for sandwiched vertical tunnel junctions. The junction was formed through an isotropically etched bowl shaped hole. The etching was timed so that the hole just breaks through the membrane, thus having an ultra small opening in the lower edge of the membrane.

The hole was fabricated combining electron beam lithography and reactive ion etching. Since PMMA is such a poor mask material for dry etching, a relatively thick layer was used. We span 6% PMMA with a speed of 2000 RPM to achieve about 500 nm thick film on the front side of the wafer. After baking the film for 1 hour at 170 $^oC$, a small spot was exposed on each membrane by simply centering the scanning area of the SEM in the middle of the membrane using a small probe current of 6 pA and accelerating voltage of 40 kV and then switching off the scanner. The dose for the different membranes on a single chip was varied by changing the time the scanner was off. This was done to achieve a range of hole diameters to insure at least one working mask on a chip despite of some variations in the subsequent processing steps. The doses used ranged from 5 pC to 50 pC. The exposed holes were developed in MIBK:$H_20$ solution (1:3 by volume) for 100 s. With this procedure we were able to define holes of about 100 nm in diameter through the thick PMMA resist film.

The transfer of the pattern into the silicon nitride membrane was done using RIE. To achieve an isotropic etching profile a relatively low RF power of 0.7 W/$cm^2$ and high pressure of 0.040 mbar (30 mtorr ) of $CF_4$:$0_2$ (5:2 by volume) was used. The etching rate for these parameters was measured to be 255±10 nm/min. This was done by etching two samples with different

thicknesses of silicon nitride in short periods and determining the thickness of the remaining film by its color [9]. The results can be seen in Fig. 27. Isotropic etching of the tiny aperture with a bowl shaped profile is the very crucial step in the fabrication and many compromises had to be done. First, the PMMA layer on the membrane should be as thin as possible to minimize scattering of electrons during the exposure of the masking hole for RIE. PMMA is, however, a very poor masking material for reactive ion etching, especially oxygen removes it very rapidly. That is why the amount of oxygen molecules in plasma has to be limited. Still, oxygen in the plasma is needed to remove residual polymers from the chamber walls and from the substrate to avoid a sudden slow-down of the etching rate. Our solution was to use as little oxygen as possible, to remove the sample from the etching chamber and to run an oxygen clean up process for the chamber.

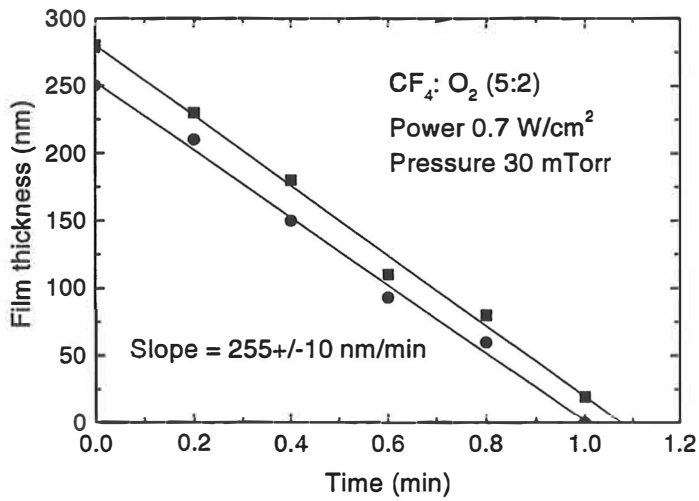


Figure 27: *Determination of reactive ion etching rate for silicon nitride films. The original LPCVD grown film thicknesses were 250 nm (circles) and 280 nm (squares).*

We processed the hole in five steps. First we cleaned the chamber by acetone and run an oxygen plasma at 0.027 mbar (20 mtorr ) with an RF power of 2.3 W/cm$^2$. This was done to remove possible contamination left in the chamber by a previous user of the instrument. After burning the plasma for 4 minutes the DC bias had increased to its empty clean chamber value (-650 V for our setup with these parameters) and the clean up process was

finished. Next the chip was inserted into the chamber and the etching process was run for 50 s until the DC bias started to decrease. Then the chamber was cleaned again running oxygen plasma for 4 minutes. The second and final etching step was similar to the first step but it lasted only for 35 seconds. Finally, the residual PMMA film was peeled off and the chamber was cleaned for the next user by running oxygen plasma cleaning process keeping the chip inside the chamber. A final etched hole can be seen in Fig. 28.

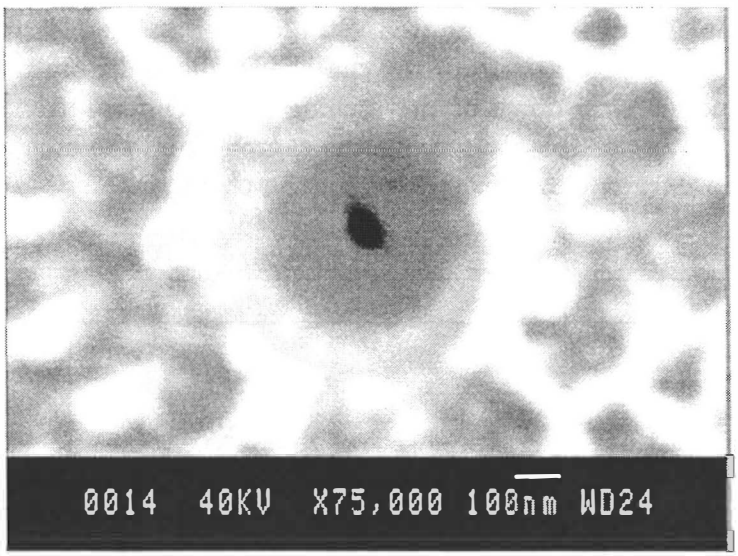


Figure 28: *Scanning electron micrograph of an etched aperture through a 300 nm thick silicon nitride membrane. The area of the final aperture is about ten times smaller than that of the masking aperture in the resist film [125].*

Also the sample position inside the chamber is very crucial. This is probably due to turbulent flow of etching gases inside the chamber. That is why we always centered the chip accurately on the plate electrode. Despite of that we realized that the diameter of the bottom orifice of our etched structure did not correlate with the electron dose used in exposure.

The metallization process is presented in Fig. 29. It was started by evaporating 200 nm of aluminium on front side of the membrane to achieve a uniform and well covering front electrode for the samples and simultaneously to grow the metal on the edges of the bowl shaped holes. A mechanical mask was used to keep the nine different samples electrically disconnected from each other. Since the bottom orifices of the holes were not to be blocked, this first evaporation was done in a large angle of $55^o$ from the normal of the membrane. After the evaporation the fresh metal surface was oxidized

at 1 mbar of pure oxygen for 1 minute to form a tunnel barrier. After the oxidation the chip was flipped over and the following evaporations took place perpendicular to the back side of the membrane. If multi junction arrays were fabricated, 10 nm thick island layers were evaporated and their surfaces were oxidized in a row, until a specified number of junctions were obtained. In the single junction case 200 nm thick aluminium layer of the second electrode was deposited directly on the first oxide. The metallizations took place in vacuum $\sim 10^{-6}$ mbar and the evaporation rate was roughly 30 Å/s for the electrodes and 10 Å/s for the islands.

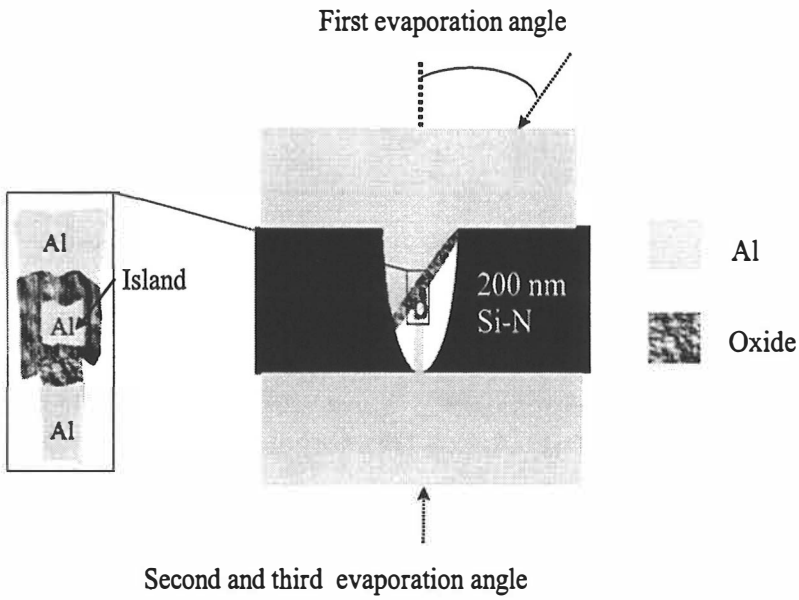


Figure 29: *Metallization of a double junction sample [125].*

The current voltage characteristics were measured for single junction devices using a DC voltage bias. At liquid helium temperature the IV curves were linear, indicating the absence of Coulomb effects. In a resistive environment - as the junctions fabricated by a conventional planar lithography and shadow angle evaporation - a sample with a capacitance of approximately $C \approx 1$ fF should show a voltage offset of $E_C/e \approx 100$ $\mu$V.

The linear IV curve might suggest that the tunneling barrier of the junction was damaged and that the junction is shorted. However, below the superconducting transition temperature of about 1.3 K the devices showed IV curves typical for aluminium SIS junctions, with superconducting energy gap of approximately $\Delta \approx 180$ $\mu$eV, typical for aluminium films. Figure 32 presents one of these curves measured at 200 mK. In addition the measured

resistances ($\sim$ 10 k$\Omega$) of the samples were typical for a tunnel junction samples and they behaved well: decreasing temperature increased the resistance since thermal exitations were suppressed [129, 130].

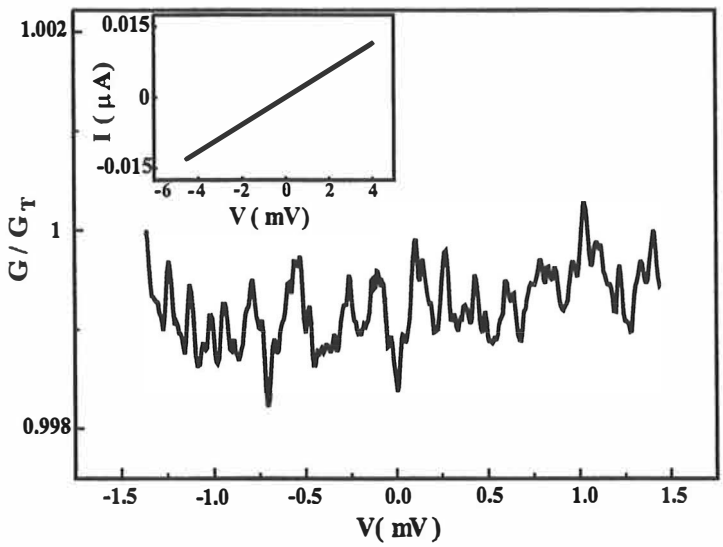


Figure 30: *A measured flat normal state differential conductance at $T$ = 300 mK and a linear IV curve at 4.2 K (inset) are indicating the absence of Coulomb blockade in single $Al/AlO_x/Al$ junction samples. This is a sign of low environmental impedance [125].*

To measure the charging effects in the junction more accurately, thermal effects were suppressed by cooling the sample down to 300 mK and superconductivity was suppressed by a magnetic field. Signal to noise ratio was improved using lock-in techniques with AC excitation at about 10 Hz frequency. As shown in Fig. 30 the measured dynamic conductance $G$ normalized to its asymptotic high voltage value $G_T$ is still flat within the noise level of about 0.1%, while lateral junctions show typically a conductance drop of 3% at 4.2 K [131] and as high as 6% at 1.3 K [132]. Using the orthodox theory, numerically calculated depth of our conductance dip of less than 0.1% at 0.3 K suggests an environmental resistive impedance less than 10 $\Omega$. The width of the conductance minimum peak corresponding to the thermal excitations at 0.3 K would be of the order of 0.1 mV (see Eq. (27)).

The low environmental impedance of these vertical junctions originates from their geometry. As illustrated in Fig. 31 the evaporated aluminium, attached to the junction on both sides of the silicon nitride membrane, shunts the junction capacitively. The current in the external circuit charges

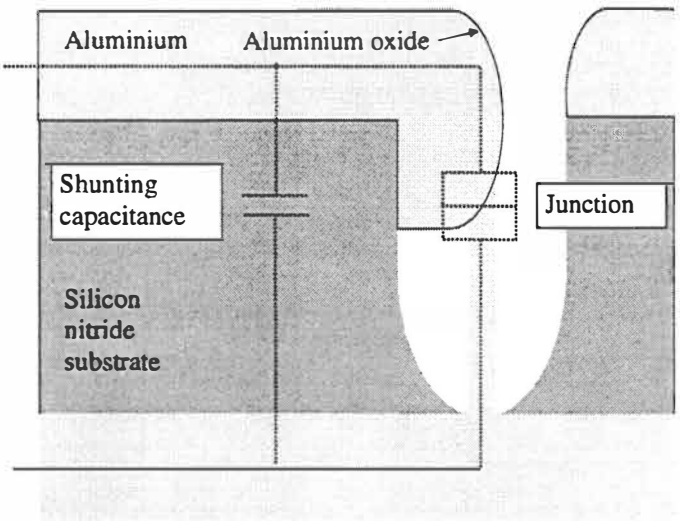


Figure 31: *The electrodes of a vertically fabricated tunnel junction form a large shunting capacitance, by which the junction gets purely voltage biased.*

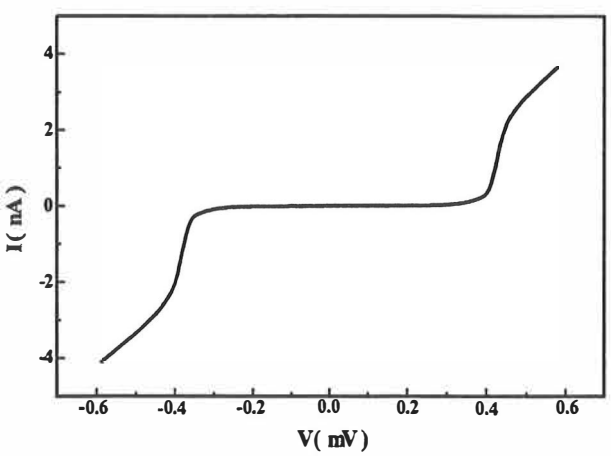


Figure 32: *Current-voltage curve of a single SIS junction through a silicon nitride membrane, measured at $T$ = 200 mK. The gap range $\pm 0.4$ mV is consistent with having just one Al-Al$O_x$-Al junction ($2\Delta \simeq 0.4$ mV).*

this shunting capacitance which is much larger than the capacitance of the junction, and thus acts as an ideal voltage source. The low environmental impedance may have applications in Coulomb blockade thermometry, for example. So far the problem of environmental impedance in lateral structures has been circumvented by using long arrays of junctions.

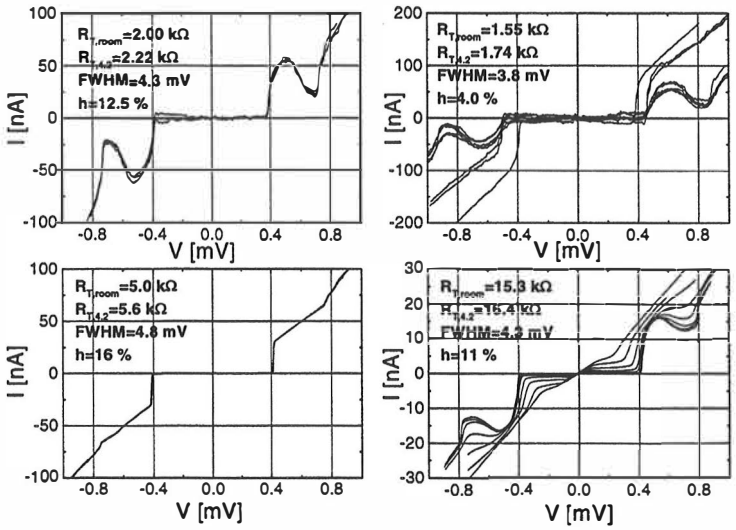


Figure 33: *Measured IV curves of four different aluminium double junction samples fabricated through a thin silicon nitride membrane. The measurements were performed at different temperatures in the superconducting state. Measured room temperature tunnel resistances together with tunnel resistance and width and height of conductance dip measured at 4.2 K are also shown.*

We have obtained quite peculiar superconducting state current-voltage characteristics for samples with two junctions separated by a metallic island. We do not understand the results as yet. When these samples were measured at liquid helium temperature clear Coulomb blockade effects can be seen in differential conductance versus voltage curves. The width of the Coulomb peak in Fig. 34 corresponds well to what can be calculated as the thermal width (Eq. (27)) for a double junction (4.0 mV at 4.2 K). The depth of the measured conductance dips ($h = \Delta G/G_T$) for different samples ranged from a few % to as high as 50% at liquid helium temperature. Assuming symmetric junctions, this corresponds to junction capacitances from a few fF to about 50 aF respectively. Further, assuming a typical thickness of the

tunnel barrier of 1 nm one obtains the junction sizes ranging from 1 $\mu m^2$ to 0.01 $\mu m^2$. In our case a small deviation in the thickness of the silicon nitride membranes combined with lateral nonuniformities in isotropic etching rate by RIE are the most probable reasons for the large variation in junction sizes.

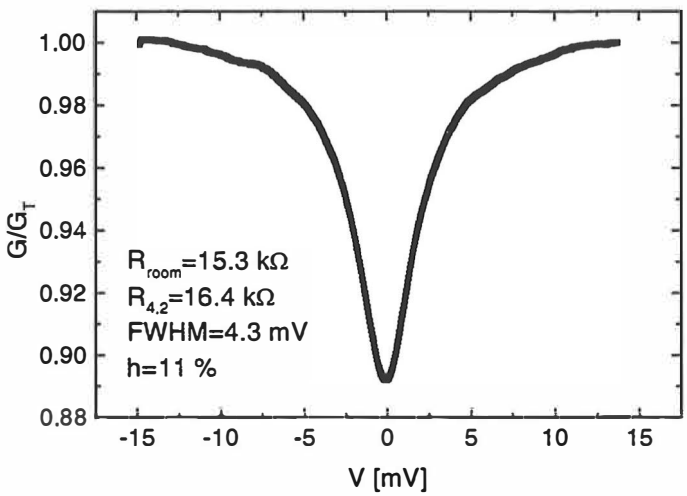


Figure 34: *Conductance curve of a double junction through a silicon nitride membrane measured at liquid helium temperature (4.2 K).*

When cooled down to below the superconducting transition temperature, IV curves of double junction samples showed a reduced superconducting energy gap structure. The gap for some samples was approximately equal to $4\Delta$ similar to that in single SIS junctions or SINIS structures. However, the existence of two junctions was verified by measuring the width of the Coulomb blockade peak at fixed temperatures in the fully normal state. In addition, the measured IV curves showed clear supercurrent peaks at zero voltage, which counts out the possibility of the island being in its normal state. Some of the samples showed an expected energy gap of $8\Delta$, but with extra bumps in the subgap area, similar to the reduced energy gap of heavily doped semiconductors or a Josephson-quasiparticle peak in SISIS stuctures [133]. Some of these measured IV curves are presented in Fig. 33. None of the fabricated samples showed a clear fully developed energy gap of $8\Delta$ typical for SISIS structure.

# 8 Micro-calorimeter

The existence and the nature of the superconducting state of small samples is dependent on the sample dimensions and geometry. The knowledge of limitations in geometry of superconducting mesoscopic features will be important in scaling down the size of superconducting devices. The effect of confinement of sample dimensions has been investigated by resistance measurements [134] suppressing the superconductivity at low temperatures by an applied magnetic field [135, 136, 137]. However, properties of small samples in the superconducting, zero-resistance state are also a subject of an increasing interest [138, 139] and they cannot be probed by a simple transport measurement. Our goal is to be able to measure the heat capacity of superconducting mesoscopic samples under various conditions.

The final part of this thesis presents a successful design for these experiments [140]. The device has been used to measure a jump in the heat capacity at the critical temperature, $T_c$ of a set of small titanium disks. According to the BCS-theory, the energy gap of the superconductor vanishes at the critical temperature, and there is a jump in the specific heat [24]. The theory gives the size of this jump as

$$\left[\frac{c_{es} - c_{en}}{c_{en}}\right]_{T=T_c} = 1.43, \tag{37}$$

where $c_{en}$ and $c_{es}$ are the electronic specific heat in the normal state and in the superconducting state, respectively. In the normal state $c_{en}$ is proportional to temperature [141]

$$c_{en} = \frac{\pi^2}{2} n_e k_B \frac{T}{T_F} = \gamma T, \tag{38}$$

where $n_e$ is the density of conduction electrons and $T_F$ is the Fermi temperature. The material dependent factor $\gamma$ is referred to as the Sommerfeld constant [141]. The specific heat in the superconducting state is exponentially dependent on temperature

$$c_{es} \propto \exp(-bT_c/T). \tag{39}$$

In addition, we have to take into account the specific heat of the lattice which, unlike the electronic specific heat does not change abruptly in the transition. However, it is dependent on the temperature following the Debye $T^3$ law [141]

$$c_{ph} = \frac{12\pi^4}{5} n_i k_B \left(\frac{T}{\theta_D}\right)^3, \tag{40}$$

where $n_i$ is the density of ions in the lattice and $\theta_D$ is the Debye temperature of the material, below which phonons start to "freeze" out.

Our method to study small superconducting structures - extensively used also in many related experiments in our laboratory - is to measure the thermal time constant $\tau = R_{th}C$ as a function of temperature of disks deposited on a thermally isolated thin silicon nitride membrane. The thermal resistance $R_{th}$ and the heat capacity $C$ can be related to the thermal conductivity $\kappa$ and the specific heat $c$, respectively, with help of the sample geometry. The thermal response of the system is very sensitive to changes of $C$ when heated using alternating power at a frequency near the thermal cut-off frequency $f_c=(2\pi\tau)^{-1}$. The heat capacity of the membrane itself is so small that the abrupt change in the heat capacity of the disks at $T_c$ can be seen as a change in the amplitude of the temperature oscillations.

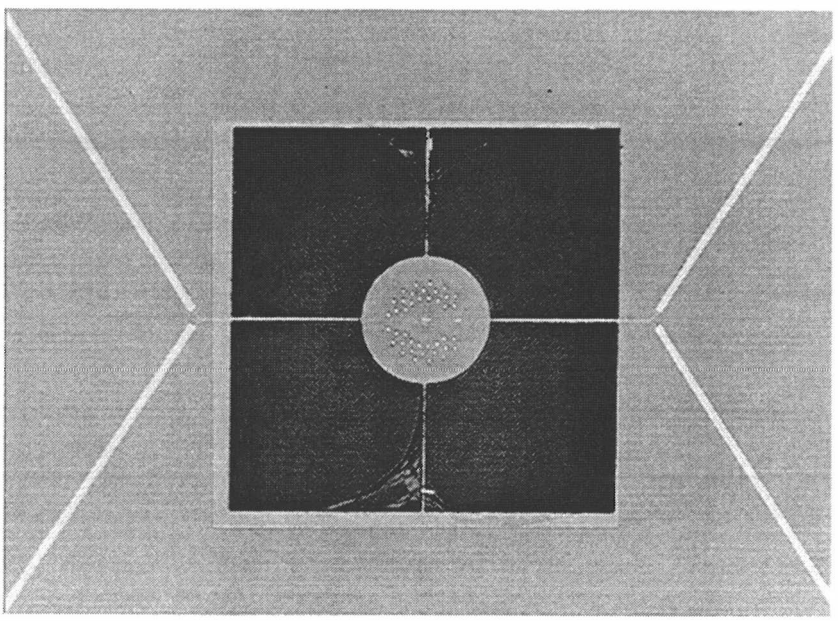

Figure 35: *A micrograph of a fabricated calorimeter. A thin silicon nitride membrane is thermally isolated by supporting it by four 200 μm long and 5 μm wide bridges.*

The sample geometry can be seen in Figs. 35 and 36. Normal metal-insulator-superconductor (NIS) tunnel junction pairs have been used both as a heater of the membrane and as a thermometer. The SINIS structure used as a heater is located in the middle of the membrane and the SINIS for thermometer uniradially with 40 titanium disks around the heater. The

radius of the disks is 7 $\mu$m and they are 400 nm thick.

An alternating current at a frequency $f = \omega/2\pi$ is applied to the heater. The heating power $P(t)$ is then proportional to $I^2 cos^2 \omega t = I^2(1 + cos 2\omega t)/2$. For this sample geometry we can assume a uniform membrane temperature so that temperature difference occurs across the four bridges of length $L$ and cross-sectional area of $S$. Then, we can approximate the heating power as $P(t) = CdT_m/dt - \kappa S \nabla T$, where $T_m$ is the temperature of the membrane and $\nabla T$ is the temperature gradient along the bridges. The thermal resistance of the bridges is $R_{th} = L/4\kappa S$. If temperature variations are small and $\kappa$ is constant, the amplitude of temperature oscillations on the membrane follows

$$\delta T \propto \left[1 + \left(\frac{f}{f_c}\right)^2\right]^{-1/2} . \tag{41}$$

This amplitude can be measured by lock-in techniques with heater current as a reference signal. The thermometer SINIS is biased at a constant current so that the voltage across the structure is slightly below $2\Delta$. Then this voltage is strongly dependent on the electronic temperature in the normal metal electrode as thermal excitations smooth out the IV curves at higher temperatures (see Figs. 7 and 8). If an accurate amplitude is needed in units of K, the voltage must be calibrated against temperature using zero heating power. For the present, however, we have not been interested in the absolute value of the amplitude, and thus the calibration is not needed. The heater can be considered as a point heater, since there is no resistance in its superconducting leads, and so stray heating of the membrane due to the Joule effect in wiring is neglible as long as one does not exceed the critical current. In addition, the superconducting leads do not shunt the thermal isolation of the membrane.

The Sommerfeld constant $\gamma$ for titanium is 3.3 mJ/molK [142]. This value gives an electronic heat capacity of $C$=2.4·10$^{-13}$ J/K for our set of disks at 1 K. At that temperature the specific heat of dielectric materials is typically less than 10$^{-3}$ J/kgK [143]. This leads to an order of magnitude smaller heat capacity of the silicon nitride membrane than that of the disks already at 1 K temperature. Since most of our measurements were carried out below that temperature, and since the heat capacity of the membrane depends on temperature more strongly than that of the electronic system, the contribution of the membrane to the heat capacity of the calorimeter is minor. Also the heat capacity of the titanium lattice is negligible at low temperatures: The Debye temperature of titanium, 415 K [142], gives about two orders of magnitude smaller heat capacity for the lattice than that of the electrons at 1 K.

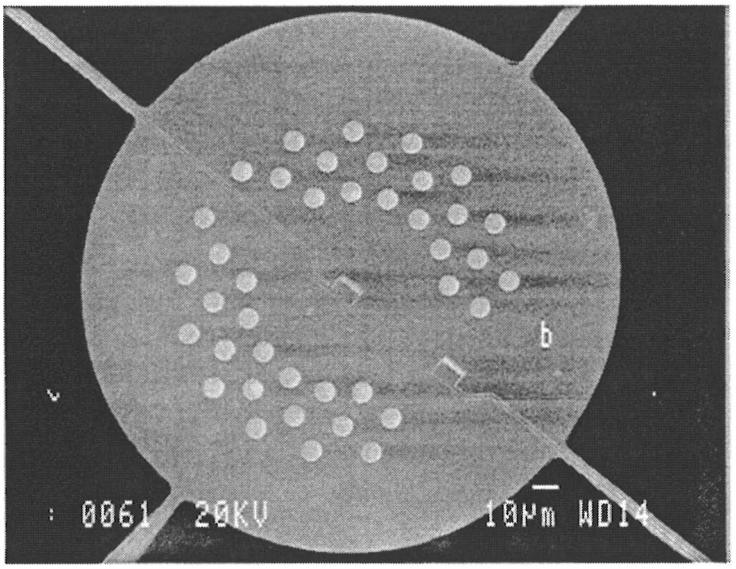


Figure 36: *Scanning electron micrograph showing the details of a fabricated microcalorimeter. The toothbrush-shaped structures are SINIS structures used both as a heater and as a thermometer. Titanium disks are located almost uniradially around the heater.*

The silicon nitride membranes used as calorimeters were fabricated similarly as membranes for vertical tunnel junctions except that now the membranes were designed to a considerably larger size, being typically 600 × 600 $\mu m^2$.

The titanium disks were patterned by electron beam lithography and vacuum deposition. Titanium was chosen as a material of the disks since its bulk critical temperature of 400 mK [142] is much below that of aluminium (1.2 K) used as a superconducting element in the NIS junctions. This is important in order to be able to measure the heat capacity of the disks at magnetic fields appropriate to observe changes in the properties of the disks, but at the same time not affecting the characteristics of the SINIS structures. In addition, titanium is considered as an easy and stable material for fabrication. The tunnel junction structures used as a heater and as a thermometer were fabricated in another EBL process using shadow angle evaporation. The superconducting electrodes were made of 15 nm thick aluminium layer. The surface of this layer was oxidized at 2 mbar of pure oxygen for 3 minutes to form an insulating tunnel barrier. The normal metal islands were deposited on that oxide. They are 55 nm thick and made of copper. The deposition took place in a large angle to eliminate the copper shadows on the membrane

Finally, this system was thermally isolated from its surroundings by supporting the membrane by just four 200 $\mu$m long and 5 $\mu$m wide bridges. These bridges were aligned by photolithography to support the aluminium wires to the heater and the thermometer. The cutting of the membrane was done by reactive ion etching similar to the cutting of the window for wet etching but with a much lower RF power of 0.7 W/cm$^2$.

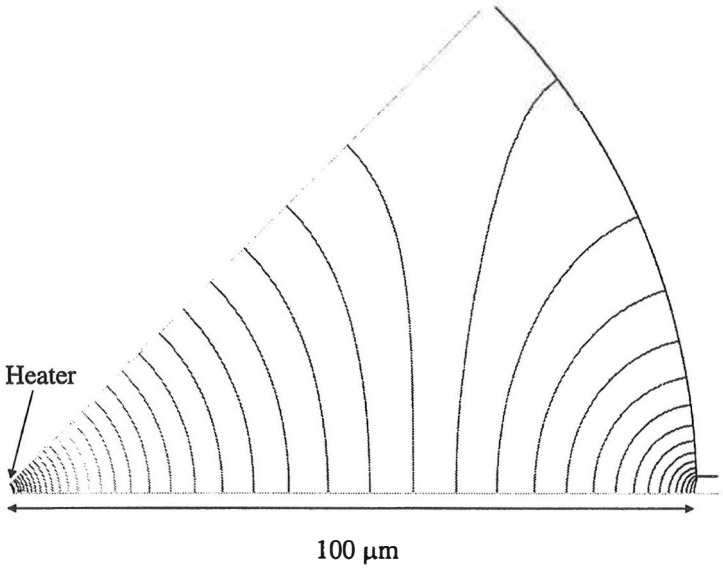


Figure 37: *Simulated equitemperature lines of an octant of a two dimensional membrane. The membrane is supported by four 200 $\mu$m long and 5 $\mu$m wide bridges. The thermal conductivity of the bridges is approximated to be ten times smaller than that of the membrane [145]. According to this simulation objects located uniradially at a distance less than half of the disk radius from the center are approximately at the same temperature.*

The geometry of the calorimeter was decided after simulations of the temperature distribution on the membrane [144]. These simulations were made to find out, how the disks should be located around the heater to keep them all at about the same temperature. In the simulations it was assumed that the AC power applied to the point heater in the middle of the membrane is so small that it heats the mambrane differentially and thus, the thermal conductivity remains constant along the membrane, and also along the bridges. The thermal conductivity through the bridges was set an order of magnitude smaller than that of the membrane based on the measurements of Ref. [145]. The energy generated by the heater was assumed to flow

from the membrane only along the four silicon nitride bridges. The heat capacity of the membrane and the fabricated structures was neglected in these simulations. The simulation for final geometry can be seen in Fig. 37.

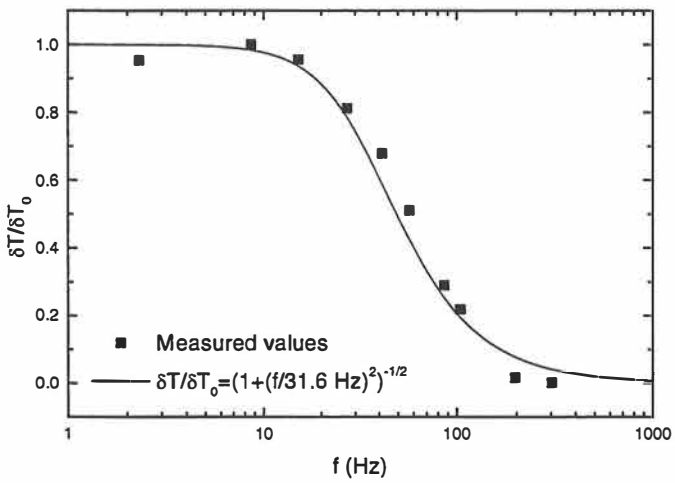


Figure 38: *Thermal response of a set of titanium disks on a calorimeter at $T$ =1 K.*

We measured the thermal cut-off frequency of temperature variations for the fabricated devices at different temperatures. This was done by altering the frequency of an applied AC heating power and measuring the thermal attenuation of the system by the thermometer on the membrane. The measured amplitude of temperature oscillations $\delta T$ was normalized by its value $\delta T_0$ at low frequencies. A measured response at 1 K is presented in Fig. 38. The thermal cut-off frequency extracted from the fit with Eq. (41) is 31.6 Hz at this temperature. The thermal conductivity of $\kappa = 1.58T^{1.54}$, has been measured for a similar silicon nitride structure with 25 $\mu$m wide and 200 nm thick bridges in Ref. [145]. Applying this formula and the measured cut-off frequency at 1 K, we obtain a heat capacity of $C = (2.44\pm0.2)\cdot10^{-13}$ J/K for our sample.

In Fig. 39 we have plotted the cut-off frequencies extracted from the measurements at different temperatures. Using $\kappa = 1.58T^{1.54}$ [145], a fit with the data points above the critical temperature leads to a $T^{-0.1}$ dependence of the heat capacity, instead of the theoretical linear dependence of electronic specific heat. On the other hand, using the calculated heat capacity for

titanium disks with the linear temperature dependence, the fit leads to a thermal conductivity of $\kappa = 1.54T^{2.68}$ for our bridge structure. The same dependence within 10% error limits was obtained also for a sample with 10 $\mu$m wide bridges.

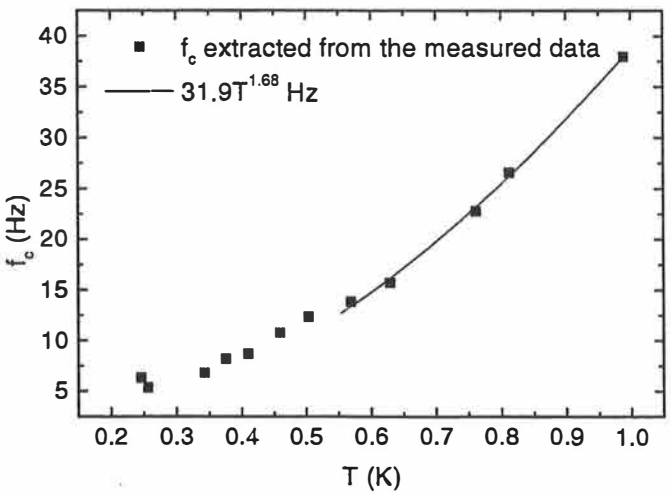


Figure 39: *Thermal cut-off frequencies as a function of temperature. The transition between the normal and the superconducting state takes place at $T \simeq 450$ mK. The fit is done with the data points measured in the normal state.*

Figure 40 presents measured thermal conductances as a function of temperature for four different silicon nitride membrane geometries. The earlier results for 200 nm thick membranes show that the exponent of the temperature dependence of $\kappa$ increases if the width of the bridges increases. In our case the exponent is close to that of bulk dielectric material and also close to that measured for 1 $\mu$m thick membranes, but the overall magnitude of $\kappa$ is close to that measured in [145] for 25 $\mu$m wide bridge geometry and 200 nm thick membrane.

An excitation at a frequency close to the cut-off frequency near the transition temperature of titanium was applied to the heater to achieve a maximum sensitivity for measurements of the jump in the heat capacity. Measured steps at three different excitation levels are presented in Fig. 41. The shape of the curves around the step is mainly determined by the sensitivity of the device. It decreases rapidly as the thermal cut-off frequency changes. The

superconducting phase boundary on the magnetic field ($H$) and temperature ($T$) -plane may be measured from the temperature shift of the step in the heat capacity for different applied magnetic fields. We measured a few points at the phase boundary, which can be seen in Fig. 42. Also the deviations due to the geometry of mesoscopic samples should be measurable using such microcalorimeters. Measurements of magnetization at this transition have been described in Refs. [147, 148].

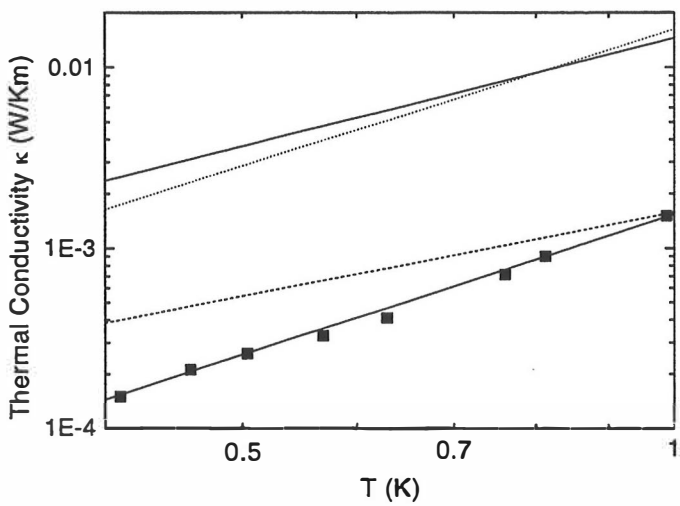


Figure 40: *Thermal conductivity as a function of T, extracted from different sources. W. Holmes [146] measured a temperature dependence of* $\kappa = 16.2T^{2.5}$ *(dotted line) for a full membrane whose thickness was 1* $\mu m$ *. The earlier results measured at our laboratory [145] were* $\kappa = 14.5T^{1.98}$ *(the uppermost solid line) for a full and* $\kappa = 1.58T^{1.54}$ *(dashed line) for a cut 200 nm thick membrane with four 25* $\mu m$ *wide bridges. Present measurements for the cut structure with four 5* $\mu m$ *wide bridges suggest a dependence of* $\kappa = 1.54T^{2.68}$.

Silicon nitride micro-calorimeters can thus be used for sensitive measurements of heat capacity at low temperatures. It is also clear that the sensitivity of the device can still be improved by optimizing the geometry. In Ref. [140] we have calculated that the heat capacity of the $L$=0 and 1 angular momentum states are qualitatively different from each other. In case of the $L$=0 state the heat capacity always decreases with increasing applied magnetic field, while the $L$=1 state can show an enhancement of heat capacity with

small magnetic field. We hope to be able to observe these phenomena with this experimental setup. We also believe that these measurements may lead to an unambiguous observation of the paramagnetic Meissner effect [139].

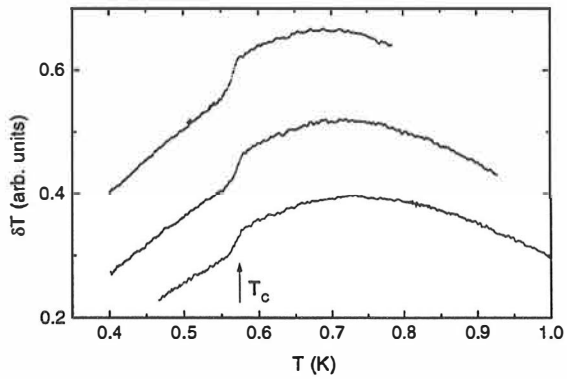


Figure 41: *The amplitude of the temperature variation of the micro-calorimeter vs. temperature of three AC excitation levels of 210 mV, 230 mV and 250 mV at a frequency of 17.4 Hz.*

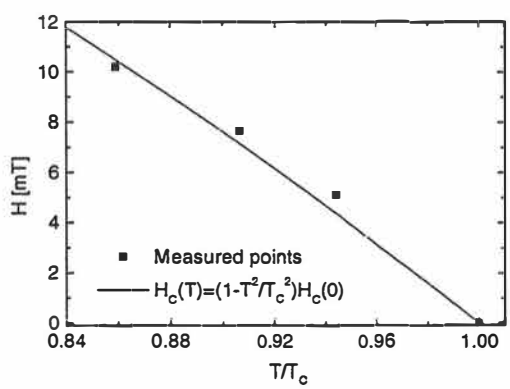


Figure 42: *Measured values of the critical magnetic field of small titanium disks as a function of temperature.*

# 9 Summary and discussion

In this thesis fabrication of small electronic devices using different combinations of atomic force microscopy, electron beam lithography and reactive ion etching processes has been investigated. Besides X-ray lithography and focused ion beam techniques, these are the most promising top-to-bottom methods in processing nano-scale devices and that is why they are under an extensive examination in many research groups all over the world.

A combination of atomic force microscopy and electron beam lithography was used to produce 20 nm wide lines a 10 nm thick PMMA resist film deposited by Langmuir-Blodgett technique on a silicon substrate. The lines were exposed by low energy electrons injected from an AFM tip applying a bias voltage of about 20 V between the sample and the tip. Lift-off of such a thin resist film was found to be extremely difficult, but pattern transfer into metallic films was still successful down to 50 nm wide lines. In the case of thin resist films one is not able to take an advantage of the celebrated shadow angle evaporation technique to fabricate a tunnel junction. We circumvented this by fabricating artificial aluminium oxide barriers. They, however, resulted in considerable shunting. Due to the problems in lift-off and barrier formation, several multi layer resist combinations were tested. Since these multi layers are always relatively thick, an exposure by tunneling electrons was out of question. Therefore an AFM tip was used to groove the soft non-baked topmost film layer. The pattern was then transferred into sub-layers by reactive ion etching and wet etching. Use of a multi layer resist and plasma processing seems to be the most promising lift-off process to fabricate small tunnel junctions with native oxide barriers, although resist reflow into the patterned grooves poses a problem.

Strongly non-linear IV curves were measured for locally anodised thin aluminium lines. A system to measure the sample resistance and control the voltage between the sample and AFM tip by an external computer was constructed. A disadvantage of this method is the great instability of the samples and their vulnerability to stray voltages. In the future, different geometries and materials will be tested.

Reactive ion etching was combined with electron beam lithography to produce circular openings of less than 100 nm in diameter to silicon nitride membranes. These holes were then used as an evaporation mask for fabrication of rows of vertical tunnel junctions with very small islands in between them. The most important observation was the very low environmental impedance. This is because the thin wires of a lateral junction have been replaced by large electrodes on both sides of a thin silicon nitride membrane. These together form a capacitor which shunts the tunnel junctions

and acts as an ideal voltage source. Peculiar IV curves were measured for double junctions below the superconducting transition temperature. Differences in the IV curves from sample to sample mirror non-uniformities in the junctions and in the islands. We found out that the quality of the silicon nitride is crucial - for one batch of wafers the etched holes were circular, while for the next batch the shape of similarly fabricated openings was quite arbitrary. Vertical junctions may have applications in metrological Coulomb blockade thermometry and in research of tunnel junctions connected by extremely small islands. For the latter purpose, designing a gate electrode to the sample will be a challenge.

Micromachined silicon nitride membranes were used as microcalorimeters. They were thermally isolated using reactive ion etching. The SINIS structures used both as a heater and as a thermometer were fabricated on these membranes by electron beam lithography. The microcalorimeters were used successfully to measure the jump in heat capacity at the superconductor -normal metal transition for a set of small titanium disks deposited on the membrane. This was done by measuring the thermal attenuation against frequency at different temperatures. After promising preliminary results, poor yield has become a trouble lately with missing or shorted tunnel junctions. After the fabrication process has been stabilized, microcalorimeters will be used for research of small superconducting samples of different geometries. The geometry of the calorimeter can be tailored for each type of a sample to reach the maximum signal to noise ratio.

# References


[1] S. M. Sze, *VLSI Technology*, Second edition (McGraw-Hill, UK, 1988).

[2] R. Turton, *The Quantum Dot: A Journey Into the Future of Microelectronics* (Oxford University Press, UK, 1995).

[3] X. Lu, S. S. K. Iyer, C. Hu, N. W. Cheung, J. Min, Z. Fan, P. K. Chu, Appl. Phys. Lett. **71**, 2767 (1997).

[4] S. M. Sze, *Semiconductor Sensors* (Wiley, New York, 1994).

[5] M. C. Peckerar, F. K. Perkins, E. A. Dobisz and O. J. Glembocki, "Issues in Nanolithography for Quantum Effect Device Manufacture" in *Handbook of Microlithography, Micromachining and Microfabrication*, Vol. 1, editor P. Rai-Choudhury (Spie Optical Engineering Press, USA, 1997).

[6] S. Datta, *Electronic Transport in Mesoscopic Systems*, Cambridge Studies in Semiconductor Physics and Microelectronic Engineering: 3, First paperback edition, eds. H. Ahmed, M. Pepper and A. Broers, (Cambridge University Press, Cambridge, 1997).

[7] K. Yoh, A. Nishida and M. Inoue, Solid State Electron. **37**, 555 (1994).

[8] A. Lindell, M. Pessa, A. Salokatve, F. Bernardini, R. M. Nieminen and M. Paalanen, J. Appl. Phys. **82**, 3374 (1997).

[9] S. M. Sze, *Physics of Semiconductor Devices*, Second Edition (Wiley, Singapore, 1981).

[10] Y. Arakawa, Solid State Electron. **37**, 523 (1994).

[11] J. P. Pekola, K. P. Hirvi, J. P. Kauppinen and M. A. Paalanen, Phys. Rev. Lett. **73**, 2903 (1994). J. P. Kauppinen and J. P. Pekola, Microelectronic Engineering **41/42**, 503 (1998).

[12] R. Fazio and G. Schön, "Mesoscopic Effects in Superconductivity" in *Mesoscopic Electron Transport*, NATO ASI Series, Vol. 345, eds. L.L. Sohn, L.P. Kouwenhoven and G. Schön, (Kluwer Academic Publishers, Dordrecht, 1997).

[13] F. Mandl, *Quantum Mechanics* (Wiley, Chichester, 1992).

[14] G-L Ingold and Yu. V. Nazarov, "Charge Tunneling Rates in Ultrasmall Junctions" in *Single Charge Tunneling*, NATO ASI Series, Vol B 294, eds. H. Grabert and M. H. Devoret, (Plenum Press, New York, 1992).

[15] M. Alonso and E. J. Finn, *Fundamental university physics*, Vol. 3 (Addison Wesley, USA, 1968).

[16] I. Giaever and K. Megerle, Phys. Rev. **122**, 1101 (1961).

[17] J. S. Moodera, R. Meservey and P. M. Tedrow, Appl. Phys. Lett. **41**, 488 (1982).

[18] J. Talvacchio, J. R. Gavaler, A. I. Braginski and M. A. Janocko, J. Appl. Phys. **58**, 4638 (1985).

[19] G. Binnig, H. Rohrer, Ch. Gerber and E. Weibel, Appl. Phys. Lett. **40**, 178 (1982).

[20] G. Binnig, H. Rohrer, Ch. Gerber and E. Weibel, Phys. Rev. Lett. **49**, 57 (1982).

[21] C. J. Chen, *Introduction to scanning tunneling microscopy* (Oxford University Press, New York, 1993).

[22] M. Tinkham, *Introduction to Superconductivity*, Second edition (McGraw-Hill, Inc., USA, 1996).

[23] L. N. Cooper, Phys. Rev. **104**, 1189 (1956).

[24] J. Bardeen, L. N. Cooper and J. R. Schrieffer, Phys. Rev. **106**, 1175 (1957).

[25] L. Solymar, *Superconductive tunneling and Applications* (Chapman and Hall Ltd., London, 1972).

[26] M. Nahum and J. M. Martinis, Appl. Phys. Lett. **63**, 3075 (1993).

[27] M. Nahum, T. M. Eiles and J. M. Martinis, Appl. Phys. Lett. **65**, 3123 (1994).

[28] O. V. Lounasmaa, *Experimental Principles and Methods Below 1 K* (Academic Press Ltd., London, 1974).

[29] A. A. Odintsov, R. Fazio and F. W. J. Hekking, "Josephson current of interacting electrons" in *Mesoscopic Superconductivity.* Proceedings of the NATO ARW, eds. F. W. J. Hekking, G. Schön and D. Averin, Physica B **203**, 361 (1994).

[30] G. Falci, V. Bubanja and G. Schön, Z. Phys. B **85**, 451 (1991).

[31] L. J. Geerligs, V. F. Anderegg, P. A. M. Holweg, J. E. Mooij, H. Pothier, D. Esteve, C Urbina and M. H. Devoret, Phys. Rev. Lett. **64**, 2691 (1990).

[32] H. Pothier, P. Lafarge, P. F. Orfila, C. Urbina, D. Esteve and M. H. Devoret, Physica B **169**, 573 (1991).

[33] J. P. Pekola, K. P. Hirvi, J. P. Kauppinen and M. A. Paalanen, Phys. Rev. Lett. **73**, 2903 (1994).

[34] D. C. Ralph, C. T. Black, J. M. Hergenrother, J. G. Lu and M. Tinkham "Ultrasmall superconductors" in *Mesoscopic Electron Transport*, NATO ASI Series, Vol. 345, eds. L.L. Sohn, L.P. Kouwenhoven and G. Schön, (Kluwer Academic Publishers, Dordrecht, 1997).

[35] G. Binnig, C. F. Quate and C. Gerber, Phys. Rev. Lett. **56**, 930 (1986).

[36] M. A. Hartney, D. W. Hess and D. S. Soane, J. Vac. Sci. Technol. B **7**, 1 (1989).

[37] C. J. Mogab, A. C. Adams and D. L. Flamm, J. Appl. Phys. **49**, 3796 (1978).

[38] Electron sensitive polymers, such as PMMA or P(MMA-MAA) can be bought, for example, from OCG Microelectronic materials Inc., 5 Garret Mountain Plaza, West Paterson, NJ 07424, USA.

[39] M. Hatzakis, J. Electrochem. Soc. **116**, 1033 (1969).

[40] B. P. Van der Gaag and A. Sherer, Appl. Phys. Lett. **56**, 481 (1990).

[41] Lord Rayleigh, Proc. R. Soc. London **47**, 364 (1890).

[42] B. Franklin, Philos. Trans. R. Soc. London **64**, 445 (1774).

[43] I. Langmuir, J. Am. Chem. Soc. **39**, 1848 (1917).

[44] I. Langmuir, Trans. Faraday Soc. **15**, 62 (1920).

[45] K. B. Blodgett, J. Am. Chem. Soc. **56**, 495 (1934).

[46] K. B. Blodgett, J. Am. Chem. Soc. **57**, 1007 (1935).

[47] S. W. J. Kuan, C. W. Frank, Y. H. YenLee, T. Eimori, D. R. Allee, R. F. W. Pease and R. Browning, J. Vac. Sci. Technol. B **7**, 1745 (1989).

[48] G. L. Gaines Jr., *Insoluble Monolayers at Liquid-Gas Interfaces* (Wiley-Interscience, 1966).

[49] L. Wilhelmy, Ann. Phys. Chem. **119**, 177 (1863).

[50] M. A. McCord and M. J. Rooks, "Electron Beam Lithography" in *Handbook of Microlithography, Micromachining and Microfabrication.* Vol. 1, editor P. Rai-Choudhury (Spie Optical Engineering Press, USA, 1997).

[51] G. Simon, A. M. Haghiri-Gosnet, J. Bournex, D. Decanini, Y. Chen, F. Rousseaux, H. Launois and B. Vidal, J. Vac. Sci. Technol. B **15**, 2489 (1997).

[52] C. N. Archie, J. I. Granlund, R. W. Hill, K. W. Kukkonen, J. A. Leavey, L. G. Lesoine, M. Q. Barton, J. P. Silverman, J. M. Warlaumont, A. D. Wilson, R. J. Anderson, N. C. Crosland, A. R. Jorden, V. C. Kempson, J. Schouten, A. I. C. Smith, M. C. Townsend, J. Uythoven, M. C. Wilson, M. N. Wilson, D. E. Andrews, R. Palmer, R. Webber and A. J. Weger, J. Vac. Sci. Technol. B**10**, 3224 (1992).

[53] M. Chaker, B. la Fontaine, C. Y. Cote, C. Kieffer, H. Pepin, M. H. Talon, G. D. Enright and D. M. Villeneuve, J. Vac. Sci. Technol. B **10**, 3239 (1992).

[54] M.J. Bowden, "A Perspective on Resist Materials for Fine Lithography" in *Materials for Microlithography, Radiation-Sensitive Polymers*, eds. L.F. Thompson, C.G. Willson and J.M.J. Frechet, American Chemical Society Symposium Series 266 (American Chemical Society, USA, 1984).

[55] E. Reichmanis and A. E. Novembre, Ann. Rev. Mater. Sci. **23**, 11 (1993).

[56] L.F. Thompson, "Resist Processing", in *Introduction to Microlithography*, Second Edition eds. L.F. Thompson, C.G. Willson and M.J. Bowden (American Chemical Society, USA, 1994).

[57] G. J. Dolan, Appl. Phys. Lett. **31**, 337 (1977).

[58] K. Valli, "Tyhjiötekniikan fysikaalisia perusteita" in *Tyhjiötekniikka.* (Suomen tyhjiöseura ry, Finland, 1986), published in Finnish.

[59] S. K. Ghandhi, *VLSI fabrication principles: silicon and gallium arsenide*, Second edition, (Wiley, New York, 1994).

[60] A. Lindell, R. Saintola and K. Valli, Nucl. Instr. and Meth. A **378**, 258 (1996).

[61] Joe Nabity, private communication.

[62] P. Grivet, *Electron Optics* (Pergamon Press, Oxford, 1965).

[63] H. Boersch, Z. Phys. **139**, 115 (1954).

[64] Raith GmbH, Hauert 18, D-44227 Dortmund, Germany, phone: +49 231 975 0000, fax: +49 231 9750005, email: Raith@raith.de, web site: www.raith.de.

[65] JSM 840A SEM conversion, JEOL Skandinaviska AB, Vegagatan 19, S-17234 Sundbyberg, Sweden, phone: +46 8 282800 fax: +46 8 291647, email: sales@jeol.se, web site: www.jeol.se.

[66] Nabity pattern generator, JC Nabity lithography systems, P. O. Box 5354, Bozeman, MT 59717 USA, phone: +1 406 5870848, fax:+1 406 5869514 email: Jcnabity@aol.com, web site: www.Jcnabity.com.

[67] C. R. K. Marrian, E. A. Dobisz and J. A. Dagata, J. Vac Sci. Technol. B **10**, 2877 (1992).

[68] C. R. K. Marrian, F. K. Perkins, S. L. Brandow, T. S. Koloski, E. A. Dobisz and J. M. Calvert, Appl. Phys. Lett. **64**, 390 (1994).

[69] L. Stockman, G. Neuttiens, C. van Haesendonck and Y. Bruynseraede, Appl. Phys. Lett. **62**, 2935 (1993).

[70] L. L. Sohn, C. T. Black, M. Eriksson, M. Crommie and H. Hess, "Scanning probe microscopes and their applications" in *Mesoscopic Electron Transport*, NATO ASI Series, Vol. 345, eds. L.L. Sohn, L.P. Kouwenhoven and G. Schön (Kluwer Academic Publishers, Dordrecht, 1997).

[71] T. R. Albrecht and C. F. Quate, J. Vac. Sci. Technol. A **6**, 271 (1988).

[72] D. Rugar, P. Hansma, Physics Today, **October**, 23 (1990).

[73] IBM Super Cone Probes, Digital Instruments, 520 East Montecito Street, Santa Barbara, CA 93103 USA.

[74] D. Nyyssonen, L. Landstein and E. Coombs, J. Vac. Sci. Technol. B **9**, 3612 (1991).

[75] A. Lindell, P. Davidsson and J. Pekola, Microelectronic Engineering **45**, 363 (1999).

[76] TMX 2010 Discoverer SPM, Topometrix, 5403 Betsy Ross Drive, Santa Clara, CA 95054-1162, USA. web site: www.thermomicro.com.

[77] F. C. Quate, Surface Science **299/300**, 980 (1994).

[78] LabPC+ board, National Instruments, 11500 N Mopac Expwy, Austin, TX 78759-3504, USA.

[79] ADG419 Analog switch, Analog devices, P.O. Box 9106, Norwood, MA 02062-9106, USA.

[80] V. Bouchiat and D. Esteve, Appl. Phys. Lett. **69**, 3098 (1996).

[81] L. L. Sohn and R. L. Willett, Appl. Phys. Lett. **67**, 1552 (1995).

[82] Ultralevers, Park Scientific Instruments, 1171 Borregas Ave., Sunnyvale, OA 94089 USA. web site: www.thermomicro.com.

[83] H. W. Lehmann and R. Widmer, J. Vac. Sci. Technol. **15**, 319 (1978).

[84] M. de Boer and Han Gardeniers, "Reactive ion etching" in *Etching technology* eds. M. Elwenspoek, M. de Boer and J. G. E. Gardeniers (Swiss foundation for research in microtechnology 1996).

[85] J. L. Vossen, J. Electrochem. Soc. **126**, 319 (1979).

[86] J. W. Coburn and H. F. Winters, J. Vac. Sci. Technol. **15**, 327 (1978).

[87] W. M. Holber and J. Forster. J. Vac. Sci. Technol. A **8**, 3720 (1990).

[88] C. J. Mogab, J. Electrochem. Soc. **124**, 1262 (1977).

[89] T. Enomoto, Solid State Technol., **April**, 117 (1980).

[90] D. L. Flamm, P. L. Cowen and J. A. Golovchenko, J. Vac. Sci. Technol. **17**, 1341 (1980).

[91] S. Matsuo, J. Vac. Sci. Tecnol. **17**, 587 (1980).

[92] M. J. Vasile and F. A. Stevie, J. Appl. Phys. **53**, 3799 (1982).

[93] H. Toyoda, H. Komiya and H. Itakura, J. Electron. Mater. **9**, 569 (1980).

[94] T. M. Mayer, J. Electron. Mater. **9**, 513 (1980).

[95] R. J. Poulsen, J. Vac. Sci. Technol. **14**, 266 (1977).

[96] J. M. Cook and B. W. Benson, J. Electrochem. Soc. **130**, 2459 (1983).

[97] J. J. Hannon and J. M. Cook, J. Electrochem. Soc. **131**, 1164 (1984).

[98] J. A. Mucha, D. W. Hess and E. S. Aydil, "Plasma Etching", in *Introduction to Microlithography*, Second Edition, eds. L. F. Thompson, C. G. Willson and M. J. Bowden, (American Chemical Society, USA, 1994).

[99] Axic Benchmark 600 with PC 5100 plasma controller, Axic, 493 Gianni street, Santa Clara, California 95054-2414, USA, phone: +1 4089800240, Fax: +1 4089800524.

[100] PDR50 Dilution refrigerator, Nanoway Co., Ylistönmäentie 26, 40500 Jyväskylä, Finland. phone: +358 14 4451500, fax: +358 14 4451504, email: cool@nanoway.fi, web site: www.nanoway.fi.

[101] 1211 Current preamlifier and 1201 Low noise preamlifier, Ithaco Inc., 735 W. Clinton street, P. O. Box 6437, Ithaca, NY, USA, phone +1 607 2727640.

[102] HP 3457A Multimeter, HP company, 3000 Hannover street, Palo Alto, California 94304, USA.

[103] SR810 DSP Lock-In amplifier, Stanford research systems, Inc. 1290-D Reamwood avenue, Sunnyvale, California 94089, USA.

[104] RV-Elektroniikka Oy PICOWATT, Veromiehentie 14, FIN-01510 VANTAA, Finland, phone: +358 9 822087, fax: +358 9 822184, email: reijo.voutilainen@picowatt.fi web site: www.picowatt.fi.

[105] Euroshield Oy, FIN-27510 Eura, Finland, phone: +358 2 8383300, fax: +358 2 8651233, email: shielding@euroshield.com, web site: www.euroshield.com.

[106] 37 204 HB-IB Extender, HP company, 3000 Hannover street, Palo Alto, California 94304, USA.

[107] W. Chen and H. Ahmed, Appl. Phys. Lett. **62**, 1499 (1993).

[108] F. Thibaudau, J. R. Roche and F. Salvan, Appl. Phys. Lett. **64**, 523 (1994).

[109] P. H. Beton, A. W. Dunn and P. Moriarty, Appl. Phys. Lett. **67**, 1075 (1995).

[110] J. W. Lyding, T. C. Shen, J. S. Hubacek, J. R. Tucker and G. C. Abeln, Appl. Phys. Lett. **65**, 2010 (1994).

[111] K. Matsumoto, M. Ishii, K. Segawa, Y. Oka, B. J. Vartanian and J. S. Harris, Appl. Phys. Lett. **68**, 34 (1996).

[112] S. C. Minne, H. T. Soh, P. Flueckiger and C. F. Quate, Appl. Phys. Lett. **66**, 703 (1995).

[113] Y. Nakamura, D. L. Klein and J. S. Tsai, Appl. Phys. Lett. **68**, 275 (1996).

[114] E. S. Snow and P. M. Campbell, Science **270**, 1639 (1995).

[115] H. J. Mamin and D. Rugar, Appl. Phys. Lett. **61**, 1003 (1993).

[116] H. J. Mamin, Appl. Phys. Lett. **69**, 433 (1996).

[117] K. Kragler, E. Gunter, R. Leuschner, G Falk, A. Hammerschmidt, H. von Seggern and G. Saemann-Ischenko, Appl. Phys. Lett. **67**, 1163 (1995).

[118] A. Majumdar, P. I. Oden, J. P. Carrejo, L. A. Nagahara, J. J. Graham and J. Alexander, Appl. Phys. Lett. **61**, 2293 (1992).

[119] K. Wilder, C. F. Quate, D. Adderton, R. Bernstein and V. Elings, Appl. Phys. Lett. **73**, 2527 (1998).

[120] Okmetic Ltd., P. O. Box 44, FIN-01310 Vantaa, Finland, phone: +358 9 502800 fax: + 358 9 50280500, email sales@okmetic.com, web site: www.okmetic.com.

[121] KSV Minitrough, KSV Instruments, P. O. Box 128, FIN-00381 Helsinki, Finland, phone: +358-9-5497 3300, fax: +358-9-5497 3333, email: info@ksvltd.fi, web site: www.ksvltd.fi.

[122] P. Davidsson, A. Lindell, T. Mäkelä, M. Paalanen and J. Pekola, Microelectronic Engineering **45**, 1 (1999).

[123] Yu. Pashkin, J. P. Pekola and L. S. Kuzmin, J. Vac. Sci. Technol. B **17**, 1413 (1999).

[124] E. S. Snow, D. Park and P. M. Campbell, Appl. Phys. Lett. **69**, 269 (1996).

[125] A. Aassime, A. J. Manninen and J. Pekola, Appl. Phys. Lett. **73**, 2369 (1998).

[126] K. S. Ralls, R. A. Buhrman and R. C. Tiberio, Appl. Phys. Lett. **55**, 2459 (1989).

[127] D. C. Ralph, C. T. Black and M. Tinkham, Phys. Rev. Lett. **74**, 3241 (1995).

[128] Karl Suss MA45 Mask aligner, Karl Suss KG GmbH and Co, Schleissheimer Str. 90, D-85748 Garching, Munich, Germany, phone: +49 89 320070, Fax: +49 89 32007162 email: info@suss.de web site: www.suss.com.

[129] J. G. Simmons, J. Appl. Phys. **35**, 2655 (1964).

[130] K. Gloos, R. S. Poikolainen and J. P. Pekola, submitted to Appl. Phys. Lett. (2000).

[131] J. P. Kauppinen and J. P. Pekola, Phys. Rev. Lett. **77**, 3889 (1996).

[132] P. Delsing, K. K. Likharev, L. S. Kuzmin and T. Claeson, Phys. Rev. Lett. **63**, 1180 (1989).

[133] Y. Nakamura, C. D. Chen and J. S. Tsai, Phys. Rev. Lett. **79**, 2328 (1997).

[134] A. Bezryadin, C. N. Lau and M. Tinkham, Nature **404**, 971 (2000).

[135] W. A. Little and R. D. Parks, Phys. Rev. Lett. **9**, 9 (1962).

[136] O. Buisson, P. Gandit, R. Rammal, Y. Y. Wang and B. Pannetier, Phys. Lett. A **150**, 36 (1990).

[137] V. V. Moshchalkov, L Gielen, C. Strunk, R. Jonckheere, X. Qiu, C. van Haesendonck and Y. Bruynseraede, Nature **373**, 319 (1995).

[138] P. S. Deo, V. A. Schweigert, F. M. Peeters and A. K. Geim, Phys. Rev. Lett. **79**, 4653 (1997).

[139] P. S. Deo, J.P. Pekola and M. Manninen, Europhys. Lett. **50**, 649 (2000).

[140] A. Lindell, J. Mattila, P. S. Deo, M. Manninen and J. Pekola, Physica B **284-288**, 1884 (2000).

[141] N. W. Ashcroft, N. D. Mermin, *Solid State Physics* (Saunders College, Philadelphia, 1976).

[142] B. W. Roberts, *Properties of Selected Superconductive Materials*, NBS Technical Note 983 (U. S. Government Printing Office, Washington D. C., 1978).

[143] F. Pobell, *Matter and Methods at Low Temperatures*, Second edition (Springer, Berlin, 1996).

[144] The simulations were done using Fluent 5.0 program by Ari Jasberg, email: ari.jasberg@phys.jyu.fi.

[145] M. M. Leivo and J. P. Pekola, Appl. Phys. Lett. **72**, 1305 (1998).

[146] W. Holmes, unpublished.

[147] A. K. Geim, S. V. Dubonos, J. G. S. Lok, I. V. Grigorieva, J. C. Maan, L. T. Hansen and P. E. Lindelof, Appl. Phys. Lett. **71**, 2379 (1997).

[148] A. K. Geim, I. V. Grigorieva, S. V. Dubonos, J. G. S. Lok, J. C. Maan, A. E. Filippov and F. M. Peeters, Nature **390**, 259 (1997).